TUDelft

Delft University of Technology

Nano-scale failure in steel

Interace decohesion at iron/precipitate interfaces

Elzas, Astrid

DOI

10.4233/uuid:f72f61f4-4508-4552-85b8-d89abbbee90e

Publication date
2019

Document Version
Final published version

Citation (APA)
Elzas, A. (2019). *Nano-scale failure in steel: Interace decohesion at iron/precipitate interfaces*. [Dissertation (TU Delft), Delft University of Technology]. https://doi.org/10.4233/uuid:f72f61f4-4508-4552-85b8-d89abbbee90e

Important note
To cite this publication, please use the final published version (if applicable).
Please check the document version above.

NANO-SCALE FAILURE IN STEEL

INTERFACE DECOHESION AT IRON/PRECIPITATE INTERFACES

Nano-scale failure in steel

Interface decohesion at iron/precipitate interfaces

Proefschrift

ter verkrijging van de graad van doctor
aan de Technische Universiteit Delft,
op gezag van de Rector Magnificus prof. dr. ir. T.H.J.J. van der Hagen,
voorzitter van het College voor Promoties,
in het openbaar te verdedigen op donderdag 10 januari 2019 om 12:30 uur

door

Astrid Elzas

Werktuigbouwkundig Ingenieur,
Technische Universiteit Delft, Nederland,
geboren te Den Haag, Nederland.

Dit proefschrift is goedgekeurd door de

promotor: prof. dr. B.J. Thijsse

Samenstelling promotiecommissie:

Rector Magnificus,	voorzitter
Prof. dr. B.J. Thijsse,	Technische Universiteit Delft, promotor

Onafhankelijke leden:

Prof. dr. ir. J. Sietsma,	Technische Universiteit Delft
Prof. dr. ir. T.J.H. Vlugt,	Technische Universiteit Delft
Prof. dr. ir. E. van der Giessen,	Rijksuniversiteit Groningen
Prof. dr. ir. A.S.J. Suiker,	Technische Universiteit Eindhoven
Prof. dr. E. Neyts	Universiteit Antwerpen, België
Dr. ir. C. Bos,	Tata Steel Europe

An electronic version of this dissertation is available at
http://repository.tudelft.nl/.

CONTENTS

SUMMARY

Multiphase alloys such as advanced high strength steels show limited ductility due to interface decohesion at internal boundaries. This interface decohesion is caused by dislocations that pile-up at interfaces in the material, where they cause a stress concentration. This stress concentration in turn can lead to interface decohesion, resulting in the formation of voids, which, when they coalesce, can form a macroscopic crack. In order to understand the process of interface decohesion and the factors facilitating this, in this thesis interface decohesion at interfaces between the soft iron matrix of steel and hard precipitates is studied at the nano-scale with molecular dynamics simulations. From the nano-scale simulations cohesive laws are derived that relate the tractions at the interface to the separations at the interface. These cohesive laws can be used to describe interface decohesion in material models at the next larger length scale (micro-scale), such as discrete dislocation plasticity.

In Chapter 2 the interaction of dislocations with an interface between iron and a precipitate under *shear* loading is studied. The properties of the precipitate material are varied, as well as the interaction strength between iron and the precipitate, to study their influence on the dislocation-interface interaction. By changing the lattice constant and/or the stiffness of the precipitate and the interaction strength between iron and the precipitate, the interface structure changes. In this chapter the iron grain and the precipitate have the same orientation. When the precipitate material has the same lattice constant as iron a coherent interface results, while for a different lattice constant a semi-coherent interface forms. It is found that not only the atomic interactions across the interface, but also the interface structure determines the adhesion across the interface. The interface structure is the key factor determining the dislocation accommodation capability of the interface: only very strong semi-coherent interfaces and very weak coherent interfaces are capable of accommodating dislocations. Strong precipitates prevent slip transfer into the precipitate, independent of the interface structure.

In Chapter 3 the interaction of dislocations with iron/precipitate interfaces is studied under *tensile* loading. Simulations are performed for different orientations of the iron and the precipitate grain, resulting in 11 different interfaces, and for up to three dislocations impinging on the interface. Based on a universal description of the adhesive energy, a *cohesive law* is derived that relates the normal tractions to the normal separations at the interface. This cohesive law can be used in larger scale simulations to describe crack growth at the interface. Only one parameter, the adhesive energy of the interface, is found to be necessary to distinguish between the different interfaces.

Chapter 4 describes the development of a cohesive law relating the tangential tractions to the tangential separations for the same 11 interfaces as in Chapter 3, but here under *shear* loading. It is found that not only the interface orientation but also the shear direction determines the interface behaviour under a shear load. The presence of a dislocation at the interface changes for some interfaces the interface structure and with that

the interface behaviour is also changed. The cohesive law derived in this chapter takes this structure change into account.

The combination of shear and tensile loading, *mixed* loading, is studied in Chapter 5. The interface behaviour is studied for both subsequently and simultaneously applied shear and tensile loading. The interface structure and the change in this structure due to the applied load and due to the interaction with a dislocation play a key role in the interface behaviour. In this chapter the cohesive laws derived for pure tensile (Chapter 3) and pure shear (Chapter 4) loading are modified to take into account the influence of the other loading direction on the behaviour during mixed loading. It is found, however, that not for every interface a generic relation between the tractions and the separations at the interface exists, but that the relation is loading-history dependent. In these cases the cohesive laws give no exact prediction of the response, but rather a range of possible values.

The in this thesis derived cohesive laws describe crack *growth* at the iron/precipitate interfaces. In Chapter 6 the crack *nucleation* process is studied. It is found that in the absence of dislocations under pure normal loading crack *nucleation* occurs according to the same traction-separation relation as crack *growth*. Impinging dislocations at the interface, however, locally modify the structure of the interface, leading to a different crack nucleation behaviour. A different loading mode can also change the interface structure and with that the crack nucleation behaviour. The cohesive laws derived in this thesis, however, do not need to be updated to correctly describe the crack nucleation behaviour. Either the crack nucleation process occurs so locally that the resolution of the larger scale method in which the cohesive laws will be applied is too coarse to take the nucleation into account. Or, when the structure changes less locally due to the dislocation and/or the loading and therefore the different behaviour also occurs less local, this different behaviour is already taken into account in the in this work derived cohesive laws.

SAMENVATTING

Meerfasige legeringen zoals geavanceerde hogesterkte stalen hebben een beperkte vervormbaarheid door loslating van interne grensvlakken. Deze zogenaamde interface-decohesie wordt veroorzaakt door dislocaties die ophopen aan grensvlakken in het materiaal, waar ze een spanningsconcentratie veroorzaken. Deze spanningsconcentratie kan vervolgens leiden tot interface-decohesie, resulterend in de vorming van holtes, die, als ze samengroeien, een macroscopische scheur kunnen vormen. Om het proces van interface-decohesie en de factoren die dit mogelijk maken te doorgronden, wordt in dit proefschrift met moleculaire dynamica simulaties interface-decohesie bestudeerd op nano-schaal aan grensvlakken tussen de zachte ijzermatrix van staal en harde precipitaten. Uit deze nano-schaal simulaties worden cohesieve relaties afgeleid die de tracties aan het interface relateren aan de separaties aan het interface. Deze cohesieve relaties kunnen gebruikt worden om interface-decohesie te beschrijven in materiaalmodellen in de naasthogere lengteschaal (microschaal), zoals discrete dislocatie plasticiteitsmodellen.

In Hoofdstuk 2 wordt de interactie tussen dislocaties en een interface tussen ijzer en een precipitaat onder *schuifbelasting* bestudeerd. De eigenschappen van het precipitaat-materiaal en ook de interactiesterkte tussen ijzer en het precipitaat worden gevarieerd om hun invloed op de interactie tussen de dislocatie en het interface te bestuderen. Door de roosterconstante en/of de stijfheid van het precipitaat en de interactiesterkte tussen ijzer en het precipitaat te veranderen, verandert de structuur van het interface. In dit hoofdstuk hebben de ijzerkorrel en het precipitaat dezelfde oriëntatie. Als het precipitaat-materiaal dezelfde roosterconstante heeft als ijzer ontstaat een coherent interface, terwijl voor een andere roosterconstante zich een semi-coherent interface vormt. Het blijkt dat niet alleen de atomaire interacties over het interface, maar ook de interface-structuur de adhesie over het interface bepaalt. De interface-structuur speelt de belangrijkste rol voor de capaciteit van het interface om dislocaties op te nemen: alleen een heel sterk semi-coherent interface en een heel zwak coherent interface kunnen dislocaties opnemen. Precipitaten met een hoge sterkte voorkomen het doorlopen van slip in het precipitaat, onafhankelijk van de structuur van het interface.

In Hoofdstuk 3 wordt de interactie van dislocaties met ijzer/precipitaat-interfaces bestudeerd onder *trekbelasting*. Simulaties worden uitgevoerd voor verschillende oriëntaties van de ijzer- en de precipitaatkorrel, resulterend in 11 verschillende interfaces, en voor 0 – 3 dislocaties die invallen op het interface. Gebaseerd op een universele beschrijving van de adhesie-energie wordt een *cohesieve relatie* afgeleid die de normale tracties aan de normale separaties aan de interface relateert. Deze cohesieve relatie kan gebruikt worden in simulaties op grotere lengteschaal om scheurgroei aan het interface te beschrijven. Slechts één parameter, de adhesie-energie van het interface, blijkt nodig te zijn om onderscheid te maken tussen de verschillende interfaces.

Hoofdstuk 4 beschrijft de afleiding van een cohesieve relatie tussen de tangentiële

tracties en de tangentiële separaties voor dezelfde 11 interfaces als in Hoofdstuk 3, maar hier voor *schuifbelasting*. Het blijkt dat niet alleen de oriëntatie van het interface maar ook de schuifrichting het gedrag van het interface bepaalt onder een schuifbelasting. De aanwezigheid van een dislocatie aan het interface verandert voor sommige interfaces de structuur van het interface en daarmee ook het gedrag van het interface. De cohesieve relatie afgeleid in dit hoofdstuk houdt rekening met deze structuurverandering.

De combinatie van een schuif- en een trekbelasting, *gemengde* belasting, wordt bestudeerd in Hoofdstuk 5. Het gedrag van het interface wordt bestudeerd voor zowel gelijktijdig als opeenvolgend aangebrachte schuif- en trekbelasting. De structuur van het interface en de verandering van deze structuur dankzij de belasting en dankzij de interactie met een dislocatie spelen een sleutelrol in het gedrag van het interface. In dit hoofdstuk worden de cohesieve relaties die afgeleid waren voor pure trekbelasting (Hoofdstuk 3) en pure schuifbelasting (Hoofdstuk 4) aangepast om de invloed van de andere belastingsrichting op het gedrag gedurende gemengde belasting in rekening te brengen. Het blijkt echter dat niet voor elke interface een generieke relatie tussen de tracties en de separaties aan het interface bestaat, maar dat deze relatie belastingsgeschiedenis afhankelijk is. In deze gevallen geven de cohesieve relaties geen exacte voorspelling van het gedrag, maar wel een bandbreedte van de mogelijke gedragingen.

De in dit proefschrift afgeleide cohesieve relaties beschrijven scheur*groei* aan de ijzer/precipitaat-interfaces. In Hoofdstuk 6 wordt scheur*nucleatie* bestudeerd. Het blijkt dat in de afwezigheid van dislocaties onder pure trekbelasting scheur*nucleatie* dezelfde tractie-separatie relatie volgt als scheur*groei*. Invallende dislocaties op het interface veranderen echter lokaal de structuur van het interface, wat leidt tot een ander scheurnucleatie-gedrag. De cohesieve relaties die in dit proefschrift afgeleid zijn hoeven echter niet aangepast te worden om scheurnucleatie-gedrag correct te beschrijven. Ofwel treedt scheurnucleatie zo lokaal op dat de resolutie van de naasthogere schaal methode waarin de cohesieve relatie toegepast zal worden te grof is om nucleatie in rekening te brengen. Ofwel, als de structuurverandering minder lokaal optreedt dankzij de dislocatie of de belasting en daarom het veranderde gedrag ook minder lokaal optreedt, is het veranderde gedrag al in rekening gebracht in de in dit werk afgeleide cohesieve relaties.

1

INTRODUCTION

The rapidly increasing global energy consumption together with the concerns for a changing climate urges for changes in human behaviour, new technologies, and, among many other things, new improved materials. The use of stronger and lighter materials will help to reduce the energy consumption.

Steel is one of the most widely used materials in industry. The global steel consumption in 2017 equalled 214.5 kg/capita. In the development of steel traditionally a trade-off had to be made between strength and ductility. Improving the strength of a material by decreasing plasticity through limiting the dislocation motion results in a decrease of the ductility. Changing the microstructure towards a heterogeneous structure, such as in dual-phase steels and other heterogeneous metals, potentially could reduce the necessity of a trade-off between strength and ductility. Because of their heterogeneous structure these materials, in theory, can be strong and show a high ductility at the same time [1]. However, these materials can show failure, caused by decohesion at internal boundaries in the materials, as is illustrated in Figure 1.1. In this thesis this failure mode is studied to understand the process of interface decohesion and the circumstances leading to this, in order to improve existing material models so that the material behaviour can be more accurately predicted.
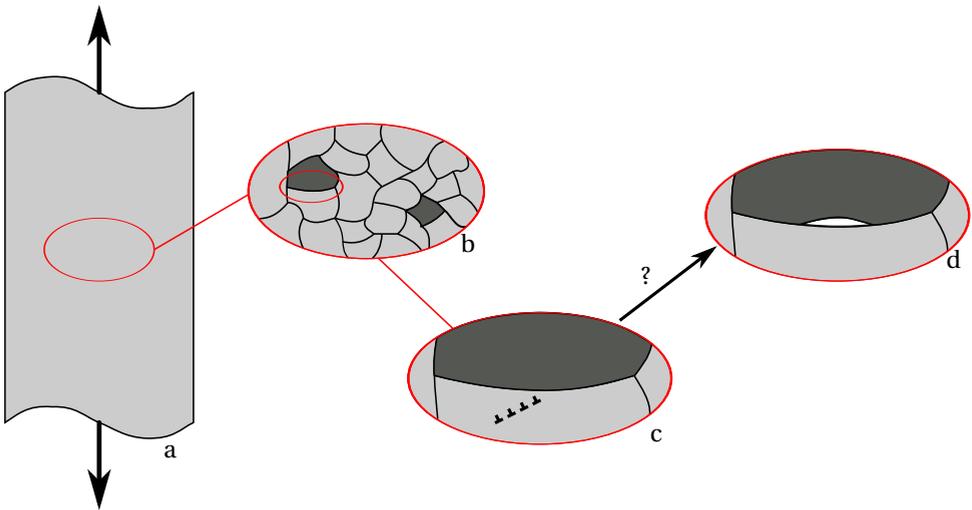
Figure 1.1: Schematic illustration of the problem of interface decohesion studied in this thesis. Under an applied load (a) dislocations start moving in the microstructure (b) of a metallic material (c). When they encounter a hard precipitate, they will be stopped at the interface between the soft metal matrix (light grey) and the hard precipitate (dark grey). New arriving dislocations will then form a pile-up which causes a stress concentration at the interface. This stress concentration might lead to decohesion of the interface (d). In this thesis this failure mode is studied to understand the process of interface decohesion and the circumstances leading to this, in order to improve existing material models so that the material behaviour can be more accurately predicted.

1.1. DUAL-PHASE STEELS

Dual-phase steels and other heterogeneous materials consist of different domains in the material which have a different strength due to a difference in composition, crystal structure, or microstructure. When these materials are deformed they show a three stage deformation. In stage 1 the soft and hard domains deform elastically. In stage 2 there is dislocation slip (movement) in the soft domains, while the hard domains continue to deform elastically. Since this leads to a mechanical incompatibility between the domains, a strain gradient results, which makes the softer phase stronger. In stage 3 both the soft and the hard domains deform plastically. Since more strain occurs in the soft than in the hard domains, this results in strain partitioning and the occurrence of strain gradients in the material. This in turn leads to work hardening due to the back-stress, which prevents necking of the material and with that it improves the ductility.

When the different domains deform plastically, this occurs by the motion of dislocations. The interfaces within the domains, the grain boundaries, and between the domains, the phase boundaries, form an obstacle for dislocation motion. At these boundaries a dislocation can be stopped, reflected, transmitted, broken up, dissolve or spawn new dislocations. The Burgers vectors and (dis-)continuity of the slip planes on both sides of the interface, the strength of the interface, and the structure of the interface all determine which of these events will occur. Furthermore, the local stress and strain in the material, for instance caused by the presence of other dislocations, will affect the interaction between dislocations and interfaces. If a dislocation is stopped at an interface and more dislocations arrive at this interface on the same slip plane, a pile-up of dislocations forms, as illustrated in Figure 1.1c. The more dislocations are present in the pile-up, the larger the stress from the pile-up on the interface. This increased stress can be a driving force for the first dislocation in the pile-up to cross the interface. However, this stress can also lead to decohesion of the interface (see Figure 1.1d). This, in turn, can result in the formation of microscopic voids, which, when they coalesce, form a macroscopic crack. If this occurs, the ductility, which was increased by the heterogeneity of the material, is again reduced.

1.2. THIS THESIS: INTERFACE DECOHESION

To prevent failure in operating conditions, material models are needed that accurately predict the performance of multi-phase steels. Since interface decohesion at the nano-scale can eventually result in macroscopic failure of the material, it is crucial that this process is well understood. What role plays the interface structure in interface decohesion, how do dislocations influence interface decohesion, what is the influence of the local stress-state on interface decohesion? These processes are studied in this thesis using computational methods. To translate this nano-scale interface decohesion to macro-scale material behaviour, the material can be modelled with a so-called bottom-up approach. In this case the material is modelled at different length scales, where crucial information from one length scale is carried on to the next, larger, length scale. This multiscale approach is illustrated in the next section.

1

1.3. COMPUTATIONAL MATERIAL MODELS

By taking the electron density of atoms into account in density functional theory, modelling the material at a length scale of several Ångstroms, one can determine certain material properties, such as the cohesive energy and the lattice constant. These properties can then be used to develop a model that describes the interaction between the atoms in molecular dynamics simulations (MD), where atoms are represented as point masses and the atomic interaction is represented as relatively simple force fields so that systems up to a length scale of several nanometers can be studied over time scales of nanoseconds. With MD simulations the mobility of single dislocations can be determined, which in turn can be the input for discrete dislocation plasticity models (DDP). These describe the plasticity of crystalline materials at an even greater length scale (microns). In these simulations plasticity is simulated by the collective motion of discrete dislocations in an elastic continuum at a length scale of several micrometers. The results from these simulations about the behaviour of grains with certain orientations and slip systems can subsequently be used as input for crystal plasticity simulations where discrete grains and slip systems are modelled so that the anisotropy of the single crystal properties and the crystallographic texture is taken into account and the material can be studied at a length scale of several millimeters. Finally, the material behaviour at a length scale of meters can be modelled with continuum plasticity, where the material is described as a homogeneous continuum. Here the discrete nature of materials is no longer taken into account. In summary, if all information from the smaller length scales is properly included in the material properties at this final meter length scale, through the bottom-up approach just described, the material behaviour can be accurately predicted.

1.4. TRANSLATING THE NANO-SCALE TO THE MICRO-SCALE

In this thesis the crucial information on interface decohesion is extracted at the nano-scale, to be carried on to the micro-scale. At the nano-scale the material is studied with molecular dynamics simulations. The interface structure, local stress state, dislocation behaviour, and interface decohesion are all natural outcomes of the simulations. Information from this nano-scale can then be translated to the micro-scale, as input for discrete dislocation plasticity simulations. As already hinted at in the previous section in DDP simulations the orientation of a grain is represented by the orientation of the slip planes. There can be different grains of material present in a simulation, modelled by differently oriented slip planes in the grains and/or by different material parameters. The interfaces between the grains are described as line contacts, for which a cohesive law relates the tractions at the contacts to the separations [2, 3]. Various shapes for such cohesive laws have been proposed, e.g. [4–8]. The parameters for a cohesive law can be obtained either from experiments or from MD simulations. When the parameters for the cohesive law are obtained from experiments, they typically are obtained from polycrystalline samples and then they describe the average behaviour of many interfaces. With MD simulations it is possible to study the behaviour of individual interfaces. The orientation of the grains making up the interface, the interface structure, dislocations impinging at the interface, and the local stress state all can be taken into account, to obtain an accurate description of interfacial debonding at the nano-scale. In this thesis

1

cohesive laws are derived from the nano-scale MD simulations to describe the interface behaviour at the micro-scale in DDP simulations.

1.5. OUTLINE OF THE THESIS

In this thesis interfaces between the softer iron matrix of steel and hard precipitates are computationally studied under different loading modes and upon interaction with different numbers of edge dislocations. The outline of this thesis is as follows:

In Chapter 2 the interaction of single dislocations and dislocation pile-ups with iron-precipitate interfaces is studied under shear loading. The properties of the precipitate material are varied, as well as the interface strength, to determine the influence of these properties on the dislocation-interface interaction.

In Chapter 3 a cohesive law is derived that relates the normal tractions to the normal separations at the iron-precipitate interfaces for crack growth at the interface under pure normal loading. This cohesive law can be implemented in a DDP framework to describe crack growth at a larger scale. This cohesive law is applicable to different interfaces, resulting from differently oriented grains, while only one parameter, the cohesive energy of the interface, is needed to distinguish between the different interfaces.

The relation between the tangential tractions and the tangential separations at the interfaces under pure shear loading is described with the cohesive law derived in Chapter 4. The relation between tangential traction and separation is heavily dependent on the interface structure. Impinging dislocations can change this structure and with that change the interface behaviour. Therefore, the influence of structure change by impinging dislocations is included in the cohesive law.

In Chapter 5 a cohesive law is derived for mixed loading conditions. Subsequent or simultaneous normal and tangential loading can lead to different interface behaviour, since the interface structure can change differently under the different loading modes. Impinging dislocations at the interface can influence the structure change of the interface under shear or mixed loading. This is included in the here derived cohesive laws.

All the cohesive laws derived in this thesis are applicable to describe crack *growth*. Crack *nucleation* under pure tensile loading in the absence of dislocation occurs according to the same traction-separation relations as crack *growth*, as is described in Chapter 6. The presence of dislocations and different loading modes, however, change the crack nucleation behaviour, making it different than the crack growth behaviour. The crack nucleation behaviour and how this should be included in the cohesive laws is also described in Chapter 6.

Finally, results and conclusions are summarised in Chapter 7.

REFERENCES

[1] X. Wu and Y. Zhu, *Heterogeneous materials: a new class of materials with unprecedented mechanical properties,* Materials Research Letters **5**, 527 (2017).

[2] G. I. Barenblatt, *The Mathematical Theory of Equilibrium Cracks in Brittle Fracture,* Advances in Applied Mechanics **7**, 55 (1962).

1

[3] D. Dugdale, *Yielding of steel sheets containing slits,* Journal of the Mechanics and Physics of Solids **8,** 100 (1960), arXiv:0021-8928(59)90157-1 [10.1016] .

[4] X. P. Xu and A. Needleman, *Void nucleation by inclusion debonding in a crystal matrix,* Modelling and Simulation in Materials Science and Engineering **1,** 111 (1993).

[5] M. J. van den Bosch, P. J. G. Schreurs, and M. G. D. Geers, *An improved description of the exponential Xu and Needleman cohesive zone law for mixed-mode decohesion,* Engineering Fracture Mechanics **73,** 1220 (2006).

[6] K. Park, G. H. Paulino, and J. R. Roesler, *A unified potential-based cohesive model of mixed-mode fracture,* Journal of the Mechanics and Physics of Solids **57,** 891 (2009).

[7] J. P. McGarry, É. Ó. Máirtín, G. Parry, and G. E. Beltz, *Potential-based and non-potential-based cohesive zone formulations under mixed-mode separation and over-closure. Part I: Theoretical analysis,* Journal of the Mechanics and Physics of Solids **63,** 336 (2014).

[8] R. Dimitri, M. Trullo, L. De Lorenzis, and G. Zavarise, *Coupled cohesive zone models for mixed-mode fracture: A comparative study,* Engineering Fracture Mechanics **148,** 145 (2015).

2

DISLOCATION IMPACTS ON IRON/PRECIPITATE INTERFACES UNDER SHEAR LOADING

Molecular dynamics simulations are performed to obtain a better understanding of the interactions of single dislocations and dislocation pile-ups with interfaces between iron and a precipitate. The material properties of the precipitate material and the iron-precipitate interaction are varied to understand the influence of interface structure, interface strength and precipitate stiffness on these interactions under shear loading. Our main findings are: (1) the interface adhesion is determined by a combination of the atomic interactions across the interface and the interface structure, (2) the interface structure is the key factor determining the dislocation accommodation capability of the interface: very strong semi-coherent interfaces do accommodate dislocations, while only very weak coherent interfaces are capable of doing this, and (3) a strong precipitate prevents slip transfer into the precipitate. Results of this study combined with those of a forthcoming study under tensile loading can be used to improve the description of interface decohesion in existing larger-scale models, such as Discrete Dislocation Plasticity.

2

2.1. INTRODUCTION

Plasticity in iron and other metals is governed by the motion of dislocations. Grain or phase boundaries can act as a barrier for dislocation motion, since crystallographic mismatch across an interface as well as atomic disorder within an interface lead to a discontinuity of slip planes, which impedes dislocation motion. At an interface, a dislocation can be stopped, transmitted, reflected, broken up and dissolve, or even spawn new dislocations. As a general rule, therefore, reducing the grain size of a material leads to a stronger material, because dislocations are faced with an increasing number of obstructing interfaces. This is expressed by the Hall-Petch relation, which states that the yield stress of a polycrystalline material is proportional to $d^{-1/2}$, where d is the mean grain size [2]. Interface effects may also have a negative influence on mechanical properties. Since dislocation motion is hindered at an interface, dislocations can pile-up in its vicinity, leading to increased stress concentrations. At high enough stresses this may lead to decohesion at the interface, resulting in void formation and eventually in the formation of a macroscopic crack. Multiphase alloys such as advanced high strength steels show limited ductility due to such decohesion at internal boundaries.

The aim of the present work is to better understand the interaction of single dislocations and dislocation pile-ups with interfaces. Different precipitate materials are encountered in steel, which have in common that they are stiffer than the matrix and, due to their different lattice constant and/or crystal structure, form semi- or non-coherent interfaces with the matrix. In our study we make use of the possibilities that simulations give us by independently changing the material properties to study the separate effect of interface strength, structure and precipitate stiffness. In this work interactions under shear loading are considered, in forthcoming work under tensile loading. By starting with a precipitate equal to iron and gradually changing to a material that is indeed stiffer and has a different lattice constant we come closer to a 'real' precipitate material. Our goal is not to describe the interactions for one specific precipitate material, but to obtain a better understanding of the mechanisms involved in dislocation-interface interactions. In addition, in order to improve existing larger-scale models such as Discrete Dislocation Plasticity, an understanding of the influence of the interface and precipitate properties on the occurrence of interface decohesion is needed. The principal phenomena studied here are slip transfer, dislocation absorption at the interface, and interface gliding. By varying independently the properties of the precipitate material and the interaction between iron and precipitate atoms (i.e. bonding strength across the interface), a comprehensive picture of the effects of strength, stiffness, lattice mismatch and interface coherency on dislocation/interface interactions is obtained. Although the simulations produce precise quantitative results, the main emphasis of the work is less focused on exact numbers. The main questions are: what happens under which conditions and what are the relative importances of the material properties of the system.

Whereas the current paper considers bcc crystals, existing work in the literature mainly deals with fcc materials. For Cu, Pan and Rupert studied crack nucleation due to multiple dislocation adsorption at a non-coherent grain boundary [3]. From their study they conclude that the capability to adsorb free volume at the grain boundary, influenced by the strain rate, reduces the crack nucleation susceptibility of that grain boundary. Shimokawa *et al.* [4] studied the influence of the interface strength on slip transfer for

a ductile and a brittle model material. These authors conclude that a higher interface strength promotes dislocation transmission and with that improves the ductility of the material.

In nano-layered materials, where the Hall-Petch relation loses its validity and there is no possibility of pile-up of dislocations because of the limited layer thickness, the degree of coherency of the interface as well as the structures of the individual grains determine the possibility for slip transfer. The strength model by Hoagland *et al.* [5] states that for a dislocation to traverse a coherent interface, a stress must be applied that cancels at least the coherency stress in one of the two grains. For a semi-coherent interface between two iso-structural grains, the coherency stress must be overcome for a glide dislocation to traverse a coherent part of the interface. In addition, the misfit dislocations at the interface must be cut for dislocation transmission at the interface to be possible. In the case of a semi-coherent interface between two non-iso-structural grains, Wang *et al.* [6, 7] propose the following mechanism for dislocation trapping or transmission at an interface: If the shear strength of the interface is lower than for the slip planes in the perfect crystal, the stress field of an approaching dislocation locally shears the interface, while creating interface dislocations bounding the sheared regions. The glide dislocation is attracted to the sheared interface and the core of the dislocation spreads in the interface. In order to have slip transmission, a stress must be applied that is large enough to compact the spread core again. A lower interface shear strength allows more spreading of the dislocation core and with that makes the interface a more effective barrier for slip transfer.

For Al, Wang [8] studied the interactions between a dislocation pile-up and a grain boundary. Depending on the available slip systems across the grain boundary and the atomic structure of the grain boundary several kinetic processes were found: grain boundary migration, grain boundary sliding, slip transmission, dislocation reflection and reconstruction of the grain boundary.

This paper is organised as follows. In Section 2.2 the simulation set-up and the specifications of the precipitate materials are explained. For the three different precipitate materials, the results are described in Sections 2.3.1, 2.3.2 and 2.3.3. In Section 2.4 the results are discussed and compared with existing literature on the subject. In Section 2.5 conclusions are presented.

2.2. Method

2.2.1. Material description

The interatomic potential for iron should accurately describe both edge dislocations in iron and the highly non-equilibrium structures resulting from dislocation pile-up/interface interactions. To describe a single edge dislocation in iron, the potential developed by Malerba *et al.* [9], optimised to describe interstitials and vacancy defects, would be a reliable choice. However, for the present study the pile-ups make this potential less appropriate [10]. Studies of crack tips [10, 11] have shown that both potential 2 developed by Mendelev *et al.* [12] and the potential developed by Ackland *et al.* [13] are good potentials for this type of study. Although they were derived from nearly the same input data and predict nearly the same material properties, they turn out to predict qualitatively

different descriptions of material behaviour at a crack tip [11]. In the current study the EAM-potential by Ackland *et al.* [13] is used.

In the EAM-format the potential energy of atom i is given by

$$U_i = F(\rho_i) + 1/2 \sum_j \phi_{ij}(r), \tag{2.1}$$

where F is the embedding energy as a function of the local electron density ρ_i, and ϕ_{ij} is the pair interaction between atom i and the surrounding atoms j as a function of their distance r. The local electron density ρ_i is made up from the contributions ψ_j to the electron density by the atoms j surrounding atom i at distances r,

$$\rho_i = \sum_j \psi_j(r). \tag{2.2}$$

F, ϕ and ψ are relatively simple functions, parametrised for Fe. They can be found in the original paper [13].

The potential that we use for the precipitate material, which we call material X, is based on this iron potential. The EAM-potential was written in effective pair format [14]. For different versions of material X the potentials were obtained by modifying the lattice constant and/or the pair interaction of the iron potential. Three different varieties of material X were constructed in this way, in order to have significant property ranges over which the influences of interface coherency, interface strength and precipitate stiffness could be studied:

- $X^{(1)}$: $\phi_X = \phi_{Fe}$, $a_X = a_{Fe}$,

- $X^{(2)}$: $\phi_X = 2\phi_{Fe}$, $a_X = a_{Fe}$,

- $X^{(3)}$: $\phi_X = 2\phi_{Fe}$, $a_X = 1.1 a_{Fe}$.

For all three X-materials the embedding term $F(\rho_i)$ was chosen to be equal to that for iron. To create $X^{(3)}$, a material with a lattice constant $a = s a_{Fe}$, where in this case $s = 1.1$, the iron EAM-potential is modified according to

$$\begin{aligned} \phi(r) &\to \phi(r/s), \\ \psi(r) &\to \psi(r/s). \end{aligned} \tag{2.3}$$

Properties of the materials Fe, $X^{(1)}$, $X^{(2)}$ and $X^{(3)}$ are shown in Table 2.1, together with the experimental values for Fe.

The pair interaction between Fe and X is constructed as a linear combination of the individual pair interactions in Fe and X and is defined by

$$\phi_{Fe-X} = q(\phi_{Fe} + \phi_X), \tag{2.4}$$

where the factor q is varied between 1/6 and 3/2 to obtain different pair interaction strengths. Note that the value of q not only reflects the atomic bonding strength across the Fe/X interface but also expresses the tendency of an FeX crystal to phase separate ($q < 1/2$) or form a compound ($q > 1/2$). For Fe/$X^{(1)}$ and Fe/$X^{(2)}$ pair interactions and

Table 2.1: Material properties at $T = 0$ K for Fe and for precipitate materials $X^{(1)}$, $X^{(2)}$ and $X^{(3)}$ created by modifying the iron-potential. Precipitate values are given relative to those of iron.

	Fe experimental	Fe	$X^{(1)}$ $a_X = a_{Fe}$ $\phi_X = \phi_{Fe}$ $F_X = F_{Fe}$	$X^{(2)}$ $a_X = a_{Fe}$ $\phi_X = 2\phi_{Fe}$ $F_X = F_{Fe}$	$X^{(3)}$ $a_X = 1.1a_{Fe}$ $\phi_X = 2\phi_{Fe}$ $F_X = F_{Fe}$
a_0 (bcc) (Å)	2.860[a]	2.855	1.00	1.00	1.10
E_{coh} (bcc) (eV/atom)	4.28[b]	4.013	1.00	1.45	1.45
C_{11} (GPa)	226[c]	243.4	1.00	1.88	1.41
C_{12} (GPa)	140[c]	145.1	1.00	1.80	1.35
C_{44} (GPa)	116[c]	116.2	1.00	2.00	1.50
B (GPa)	169[d]	177.9	1.00	1.84	1.38
E (GPa)	119	134.9	1.00	1.99	1.49
a_0 (fcc) (Å)	3.562[e]	3.658	1.00	1.01	1.11
E_{coh} (fcc) (eV/atom)		3.892	1.00	1.43	1.43

[a] Ref. [15]
[b] Ref. [16]
[c] Ref. [17], value at room temperature.
[d] Ref. [15], value at room temperature.
[e] Ref. [18]

$q = 1/2$ this equals the alloy model by Johnson *et al.* [19] which gives an alloy model which is invariant to transformations in the monatomic models from which it is derived. However, there is no physical requirement for this invariance. In order to study the influence of interface strength when no other parameters are changed, we therefore chose to describe the pair interaction by Equation 2.4, to create a continuous scale over which the interface strength can be varied. For different choices of q the interface energies are given in Table 2.2, where the energy is the difference in energy with respect to the energy of the same number of Fe and X atoms in a bulk crystal. For all the systems in Table 2.2 the summed surface energies of the two crystals are higher than the interface energy. This means that all interfaces are stable.

2.2.2. Setup

For the molecular dynamics simulations Fe/X bi-crystal systems were created as shown in Figure 2.1. Both crystals are oriented along x: $[01\bar{1}]$, y: $[011]$, z: $[100]$. To accommodate the large strain fields of dislocations in iron, the system size was chosen as $155 \times 1.2 \times 110$ nm for Fe–$X^{(1)}$ and Fe–$X^{(2)}$, while for Fe–$X^{(3)}$ the thickness (y-direction) was increased from 1.2 to 4.4 nm to accommodate the interface structure resulting from the misfit in lattice constant. In the iron grain one or multiple $\{112\}\langle 111\rangle$ edge dislocations are inserted on the same $(2\bar{1}1)$ slip plane. In the shearing simulations, atoms in the lower 10 Å are kept fixed, region F, and on the atoms in the upper 10 Å, region D, a shear displacement is imposed with a constant strain rate $\dot{\gamma}$ of 10^8 s^{-1}. For the mobile atoms,

Table 2.2: Interface energies for Fe–X interfaces with different varieties of the precipitate material X and different choices of q, as defined in Equation 2.4. Both grains are oriented according to x: $[01\bar{1}]$, y: $[011]$, z: $[100]$.

2

$X = X^{(1)}, \phi_X = \phi_{Fe}, a_X = a_{Fe}$

ϕ_{Fe-X}	$1/2\phi_{Fe}$	ϕ_{Fe}	$3/2\phi_{Fe}$	$2\phi_{Fe}$	$3\phi_{Fe}$
E_{int} (mJ/m^2)	1566	0	-1594	-3213	-6517
q	1/4	1/2	3/4	1	3/2

$X = X^{(2)}, \phi_X = 2\phi_{Fe}, a_X = a_{Fe}$

ϕ_{Fe-X}	$1/2\phi_{Fe}$	ϕ_{Fe}	$3/2\phi_{Fe}$	$2\phi_{Fe}$	$3\phi_{Fe}$
E_{int} (mJ/m^2)	3120	1566	-10	-1605	-4848
q	1/6	1/3	1/2	2/3	1

$X = X^{(3)}, \phi_X = 2\phi_{Fe}, a_X = 1.1a_{Fe}$

	$1/2\phi_{Fe}$	ϕ_{Fe}	$3/2\phi_{Fe}$	$2\phi_{Fe}$	$3\phi_{Fe}$
E_{int} (mJ/m^2)	3386	2287	1041	-273	-3040
q	1/6	1/3	1/2	2/3	1

region M, time integration is performed at 1 K with a Nosé-Hoover thermostat, using a time step of 5 fs. Prior to loading, the system is equilibrated at 1 K for 100 ps. The stress τ that results from the applied strain is calculated by summing the resulting forces on the atoms in region D and dividing this by the area of the system in the x, y-plane.

Figure 2.1: Setup for the study of dislocation/interface interactions. Atoms in region F are kept fixed, atoms in region M are the mobile atoms, whose positions are updated by time integration of the force field. The atoms in region D are moved in the x-direction with a constant strain rate of $\dot{\gamma} = 10^8$ s^{-1}. In the Fe grain zero, one or multiple $\{112\}\langle 111\rangle$ edge dislocations are inserted on the same slip plane before starting the simulation. Both crystals have $\langle 110\rangle$ directions along x and y and $\langle 100\rangle$ along z.
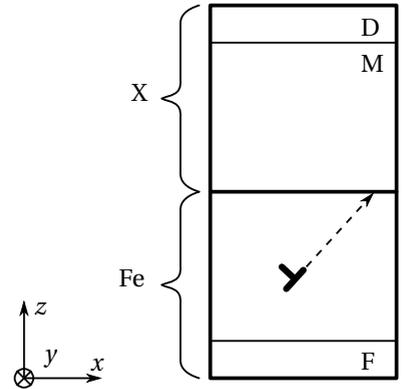
The typical cleavage plane in α-iron is the (100) plane, with the crack front direction either in the [001] or the [011] direction. When interface decohesion occurs, the interface will be the crack plane. In this study therefore, the orientation of the grains was chosen such that the interface is an (100) plane. The interaction of dislocations with interfaces is studied in a system which is periodic in the interface plane. The dislocation line direction has to be in a periodic direction to study an infinitely long dislocation and is therefore chosen to be equal to the crack front direction. In iron the $\{110\}\langle 111\rangle$,

{112}⟨111⟩ and {123}⟨111⟩ slip systems can be active. For the {112}⟨111⟩ slip system the dislocation line lies in the [011] direction and therefore this slip system and the grain orientation as described above are chosen in this study.

In this study all simulations are performed at 1 K. By performing the simulations at this low temperature the dislocation-interface interactions can be studied in detail without the interactions being hidden by the thermal vibrations present at a much larger scale at higher temperature.

The interface structure for Fe–X[3] was created using the method described by Tschopp and McDowell [20]. Of all the structures created, the structure of which the interface energy has the highest number of occurrences was chosen. The MD simulations are performed with LAMMPS [21], the structures are visualised with OVITO [22], additional analysis is done with Matlab.

2.3. RESULTS

2.3.1. FE–X[1], ONLY INFLUENCE OF INTERFACE STRENGTH

The specific role of the interface strength on dislocation/interface interactions is studied for the simplest case, the interface between Fe and X[1], which are materials with identical properties. Both grains have the same lattice constant and are equally oriented, leading to a fully coherent interface. Only the pair interaction between Fe and X[1] (i.e., across the interface) is varied, leading to different interface strengths.

A strong interface, $q \geq 3/4$, is expected to block dislocation movement. Our simulations for a single dislocation indeed show that for these interfaces the dislocation is stopped (blue, red and black curves in Figure 2.2a), at least up to a certain applied strain which depends on q. The reason is straightforward. The stronger bonding between atoms across the interface than in the bulk makes that a higher critical resolved shear stress has to be overcome for the dislocation to cross the interface than for dislocation motion in the bulk crystal. If the interface is not too strong, $q = 3/4$, the resolved shear stress on the dislocation eventually becomes high enough for the dislocation to cross the interface, at an applied strain $\gamma = 0.046$ (blue curve in Figure 2.2a). For higher interface strengths (red and black curves), the material fails elsewhere before a high enough shear stress on the dislocation is reached. Close inspection shows that the dislocation initially stops not in the interface itself but several ångströms underneath the interface (Figure 2.2b). We show below that already for two dislocations such halting effects occur with far more complexity.

A medium-strength interface, $q = 1/2$, has a special role in the cases studied here, where it is purely the interface strength that affects the motion of the dislocation in and through the interface. For $q = 1/2$ there is not even an interface effect at all. The bonding across the interface is exactly equal to that in the bulk of both crystals and the slip plane in the iron grain perfectly continues into the precipitate. Therefore, the dislocation can move unhindered into the precipitate, as can be seen from the green curves in Figure 2.2.

For a weak interface, $q = 1/4$, the dislocation enters the interface and, as one might expect, is accommodated inside the interface without being transferred into the precipitate (Figures 2.2a and 2.2b). The bonds between the atoms across the interface are weaker than those in the bulk, making it energetically favourable for the dislocation to

2

(a)

(b)

(c)

(d)
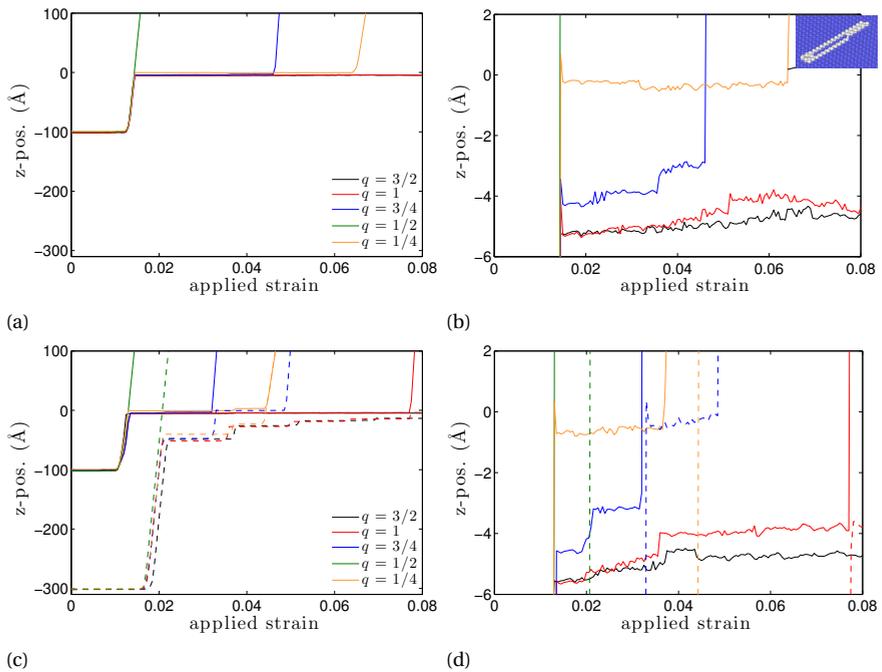
Figure 2.2: z-position of dislocations versus applied strain for Fe–X$^{(1)}$ systems with different interface strengths, loaded in shear with $\dot{\gamma} = 10^8\ \mathrm{s}^{-1}$. The interface is located at $z = 0$ Å. In (a) the position of a dislocation in a system with one dislocation is shown, (b) is an enlargement showing details in the interface region. In (c) the positions of the first (solid lines) and second (dashed lines) dislocation in a system with two dislocations are shown, (d) shows details in the interface region. The inset in (b) shows a twin that grows from the interface into the precipitate for the case $q = 1/4$. See the main text for more explanation.

stay in the interface rather than to move into the bulk. For the Fe–$X^{(1)}$ systems, apart from the dislocation(s) and the outer surfaces, the whole system is in a perfect bcc structure, since the lattice constant and the orientation of both grains is equal. The mechanism by which a dislocation moves into or through the interface or in the precipitate is therefore not different from the mechanism by which it moves inside the iron grain. The energy barrier for dislocation movement however, is different in the interface than in the bulk, due to the different pair interaction between Fe and X atoms from that between Fe atoms alone.

At the moment when the dislocation moves inside the interface, for $q = 1/4$, the resolved shear stress on the dislocation is already high enough to make it move in the iron grain and, due to the equality of Fe and $X^{(1)}$, also in the precipitate. It does not move into the precipitate, however. At first sight this may seem surprising. The explanation is that the interactions between Fe and $X^{(1)}$ are weaker than between Fe and Fe or $X^{(1)}$ and $X^{(1)}$, making it energetically more favourable for the dislocation to be at the interface than to move into $X^{(1)}$. When the dislocation enters the interface a small step in the iron side of the interface is formed. The precipitate atoms slightly move downwards at the lower side of the step. This downward movement of precipitate atoms leads to the shift of one atomic $(2\bar{1}1)$ plane in the precipitate with respect to another one and gives the formation of a twin in the precipitate, as shown in the inset in Figure 2.2b.

When we repeat the study in the presence of a second initial dislocation behind the first one on the same slip plane, we obtain the results in Figures 2.2c and 2.2d. They should be compared with the single-dislocation case of Figures 2.2a and 2.2b. The first thing one notices is that, as expected, the lower, second dislocation needs a larger applied strain to start moving (0.017) than the upper, first dislocation (0.010). In the 'unhindered' case, $q = 1/2$, the first dislocation has already crossed the interface before the second dislocation has even started to move. Therefore, in this case the second dislocation has a negligible effect. This is different for the other interface strengths. The orange solid lines (for the weak interface, $q = 1/4$) and the blue and red solid lines (for the strong interfaces, $q = 3/4$ and $q = 1$) show that in the two-dislocation case the first dislocation escapes from the interface region into the upper crystal significantly earlier than in the one-dislocation case. In other words, the second dislocation 'pushes' the first dislocation through the interface: the stress field of the second dislocation increases the resolved shear stress on the first dislocation and with that helps to move the dislocation into the precipitate at a lower applied strain. Note that in these cases the second dislocation finds an initial halting place at approximately 45 Å below the interfaces. At further shearing the stress builds up until it is high enough for the dislocation to move further towards the interface. Again it finds a halting place, where the stress has to build up again before the dislocation is capable of moving further towards the interface. This is seen in the stepwise fashion the dislocations approach the interface before ultimately crossing the interface (dashed lines).

For a very strong interface ($q = 3/2$, black lines) with 2 dislocations no slip transfer is seen. Repeating the simulation with 3 dislocations on the same slip plane did not lead to slip transfer either, but again to nucleation of multiple dislocations. The critical stress for slip transfer is not reached.

In a pile-up of dislocations in equilibrium, the force on each dislocation, consisting of contributions from the applied stress and the interaction with other dislocations, is zero, for every dislocation except the first. The stress on the first dislocation equals $n\tau_a$, where n is the number of piled-up dislocations behind the first dislocation and τ_a is the applied shear stress [23]. For a stronger interface, the critical resolved shear stress for slip transfer is increased and therefore a larger pile-up is needed to get slip transfer into the precipitate.

The results for dislocation/interface interactions for Fe-X$^{(1)}$ interfaces are summarised in Table 2.3.

Table 2.3: Summary of results for the Fe-X$^{(1)}$ interface. q defines the pair interaction strength between Fe and X$^{(1)}$ (see Equation 2.4). The first column (# D) lists the number of edge dislocation initially present in the lower crystal (Fe). The table shows the main events observed and the applied shear strains at which the events occur (in parentheses):
- twin: formation of twin grain in precipitate,
- transfer: the dislocation transfers into the precipitate and continues,
- immediate transfer: dislocation transfers interface without being temporarily stopped by the interface,
- blocked: the dislocation is blocked by the interface and cannot continue in the precipitate.

# D	$q = 1/4$	$q = 1/2$	$q = 3/4$	$q = 1$	$q = 3/2$
1	twin (0.065)	immediate transfer (0.014)	transfer (0.050)	blocked	blocked
2	twin (0.040)	immediate transfer (0.013, 0.022)	transfer (0.035, 0.050)	transfer (0.080, 0.095)	blocked

2.3.2. FE–X$^{(2)}$, INFLUENCE OF PRECIPITATE STIFFNESS + INTERFACE STRENGTH

The combined effects of the precipitate stiffness and the interface strength on the dislocation/interface interactions is studied with the Fe–X$^{(2)}$ interface. The pair interaction in X$^{(2)}$ is twice as strong as the pair interaction in iron, while the lattice constants are equal. The interface energy is varied by the parameter q as shown in Table 2.2.

For these stiff-precipitate systems Fe-X$^{(2)}$, it follows from our simulations that the critical stress for slip transfer is higher than the nucleation stress for lattice or interface dislocations. Of all the different cases of interface strength (q between 1/6 and 1) and number of dislocations (1-3), only one led to dislocation slip transfer: $q = 1/2$ and 1 dislocation. In all the other cases lattice dislocations nucleate from the interface into the iron grain as well as new interface dislocations. Figure 2.3 shows the critical stress levels found for the different systems. In all cases except one, it is dislocation nucleation that takes place at the critical stress value, showing that for all these cases slip transfer would need a higher stress. Since the interface is fully coherent, it is only the combination of

the higher Peierls stress for dislocation motion and the interface strength that causes this behaviour.

The critical stress shown in Figure 2.3 is the measured global stress at the boundary of the simulation box. This is not the same as the local stress that can be measured in different parts of the system. It is the local stress that determines if slip transfer or dislocation nucleation occurs. The critical local stress that has to be overcome for either dislocation nucleation or slip transfer does not change with increasing pile-up length. The moment (measured in global applied strain) at which this critical stress is reached, however, does change with increasing pile-up length, as can be seen in Figure 2.3.
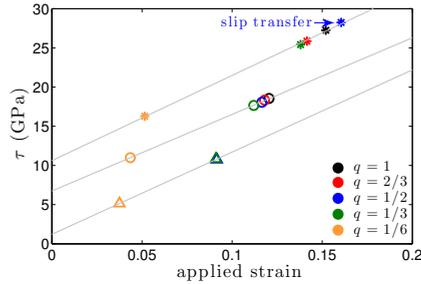
Figure 2.3: Critical stress at which dislocation nucleation occurs (in one case slip transfer) for different interface strengths and different numbers of dislocations for the Fe–X$^{(2)}$ system. $\star$: 1 dislocation, $\circ$: 2 dislocations, $\triangle$: 3 dislocations. Only for $q = 1/2$ and one dislocation slip transfer is found, while in all other cases dislocations are nucleated, at a lower stress. For clarity data for 1 and 2 dislocations have been shifted upwards by 10 and 5 GPa, respectively. Straight lines are fits to the data. The figure shows that the critical stress for slip transfer is higher than for dislocation nucleation.

For the case of $q = 1/2$ slip transfer is seen when only one dislocation interacts with the interface. When more dislocations interact with the interface, an avalanche of dislocations is nucleated from the interface. In these cases, similar to the single dislocation case, only the first dislocation has entered the interface. The other dislocations form a pile-up. This pile-up leads to a higher local stress at the interface for a certain amount of applied strain than without a pile-up. The same stress is therefore reached at lower applied strain, when there are more dislocations present in the pile-up. Since there is a mismatch in elastic modulus between iron and the precipitate, a lower applied strain leads to less distortion of the bcc structure at the interface, continuing from the iron grain into the precipitate. Apparently, for this interface strength, less distortion leads to a lower critical stress for dislocation nucleation than for slip transfer. Repeating the simulation with a 6 times as thick sample does not significantly alter the behaviour when two or three dislocations interact with the interface. For one dislocation, however, no slip transfer is seen in this cases, but also an avalanche of dislocations is nucleated at a strain of 0.1405, which is the expected result based on the simulations with other interface strengths and/or more dislocations. In the one dislocation case the thickness clearly influenced the nucleation stress.

For a weak interface, $q = 1/6$, the global stress at which nucleation occurs is significantly lower than for stronger interfaces, as can be seen in Figure 2.3. For this weak interface the first dislocation that approaches the interface immediately enters the inter-

face, while for stronger interfaces it turns out that it is stopped underneath the interface. This dislocation is reflected from the interface (C), upon nucleation of a pair of interface dislocations (A and B), as shown in Figure 2.4, top, and another lattice dislocation that moves into the iron grain (D). The total Burgers vector is conserved. Dislocation B in the right-hand side of Figure 2.4, top, is a mobile interface dislocation, moving to the right. When a second dislocation enters the interface (not shown), such a nucleation event of lattice and interace dislocations is repeated. The motion of the interface dislocations results in interface sliding.

For stronger interfaces not just one dislocation but an avalanche of dislocations is nucleated from the interface, leading to a completely damaged material, Figure 2.4, bottom. The precipitate has the same lattice constant and orientation as the iron grain. There is therefore no geometrical barrier for the dislocation to move from the iron grain into the precipitate. The precipitate, however, is stiffer than iron, leading to a higher critical resolved shear stress for dislocation motion in the precipitate than in iron in this particular case. The critical stress for dislocation nucleation in iron is reached before this critical resolved shear stress is reached, leading to the avalanche of dislocations nucleating from the interface into the iron grain, rather than a transfer of the incident dislocation into the precipitate.
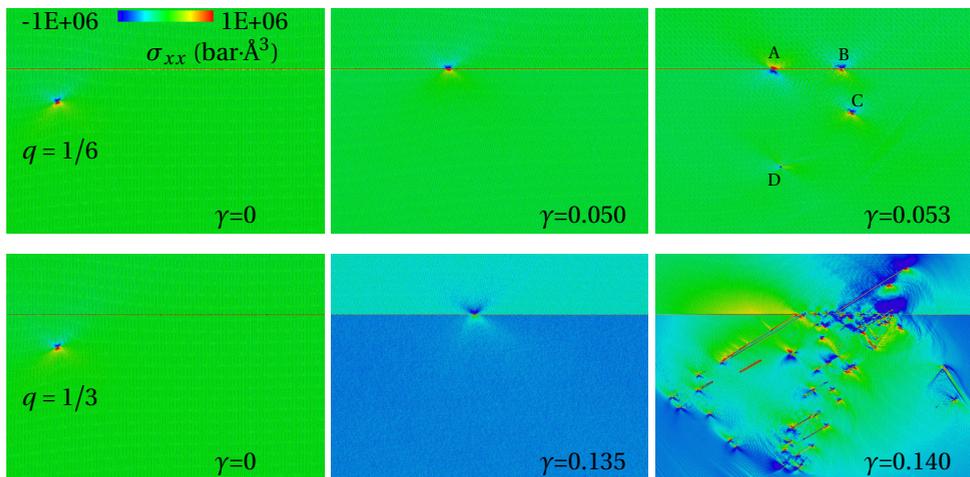
Figure 2.4: Dislocation/interface interactions for the Fe–X$^{(2)}$ system with $q = 1/6$ (top row) and $q = 1/3$ (bottom row). For $q = 1/6$ the dislocation moves into the interface, $\gamma = 0.050$, where it is reflected into the iron grain (C), upon nucleation of a pair of interface dislocations (A and B) and a lattice dislocation in the iron grain (D), $\gamma = 0.053$. For $q = 1/3$ the dislocation is initially stopped underneath the interface and then gradually moves into the interface, $\gamma = 0.135$. When the critical nucleation stress is reached, $\gamma = 0.140$, an avalanche of dislocations is nucleated, leading to damage all over the structure. Colours indicate local stress. The xx-component of the local stress tensor is shown to get a clear view on dislocation positions.

Similar to the Fe–X$^{(1)}$ system, the presence of a second dislocation on the same slip plane 'pushes' the first dislocation towards the interface at a lower global stress and strain level. The presence of the stress field of the second dislocation, however, is not enough to push the first dislocation into the precipitate. Since the precipitate is stiffer

than iron, it has a higher elastic modulus, making the critical resolved shear stress for dislocation motion in the precipitate higher than in iron. As is shown in Figure 2.3, for all cases except one, dislocation nucleation into iron or into the interface occurs before slip transfer is seen. We can therefore conclude that the local critical stress for slip transfer is higher than the local critical stress for dislocation nucleation. Due to the presence of multiple dislocations in the pile-up, the local stress is increased, and therefore the critical stress for dislocation nucleation is reached at a lower global stress and strain level and before the critical stress for slip transfer can be reached. A larger pile-up of dislocations will therefore not lead to slip transfer into the precipitate.

The results for dislocation/interface interactions for Fe-X$^{(2)}$ interfaces are summarised in Table 2.4.

Note that in the cases studied so far, the atomic structure at the interface is not modified for any of the interface strengths or precipitate stiffnesses. There is therefore no discontinuity in the glide plane that would make it more difficult for a dislocation to move into the precipitate. Such discontinuities are introduced in the upcoming section.

Table 2.4: Summary of results for the Fe-X$^{(2)}$ interface. q defines the pair interaction strength between Fe and X$^{(2)}$ (see Equation 2.4). The first column (# D) lists the number of edge dislocation initially present in the lower crystal (Fe). The table shows the main events observed and the applied shear strains at which the events occur (in parentheses):
  • transfer: the dislocation transfers into the precipitate and continues,
  • nucl.: nucleation of dislocation pair at the impact point of the dislocation(s),
  • avalanche: avalanche of dislocations nucleated from the impact point of the dislocation(s).

# D	$q = 1/6$	$q = 1/3$	$q = 1/2$	$q = 2/3$	$q = 1$
1	nucl. (0.051)	avalanche (0.138)	transfer (0.160)	avalanche (0.141)	avalanche (0.152)
2	nucl. (0.043)	avalanche (0.112)	avalanche (0.116)	avalanche (0.118)	avalanche (0.120)
3	nucl. (0.037)	avalanche (0.091)	avalanche (0.091)		

2.3.3. FE–X$^{(3)}$, INFLUENCE OF INTERFACE STRUCTURE + PRECIPITATE STIFF-NESS + INTERFACE STRENGTH

The influence of interface structure resulting from lattice mismatch, combined with the earlier effects of precipitate stiffness and interface strength, is studied with Fe–X$^{(3)}$ systems. The pair interaction in X$^{(3)}$ is the same as in X$^{(2)}$, being twice the pair interaction in Fe. The lattice constant of X$^{(3)}$ is 1.1 times the lattice constant of iron. This mismatch in lattice constant leads to a structure of misfit dislocations at the interface, resulting in a semi-coherent interface. A picture will be shown later, in Figure 2.8, top. As can be seen in Table 2.2, the interface energies for the different interface strengths are higher than those for Fe–X$^{(2)}$ systems, for same values of q.

Without dislocations, shearing the Fe–X$^{(3)}$ system eventually results in interface sliding for all values of q, as is shown by the black curves in Figure 2.5a to 2.5e. For medium

and strong interfaces, $q \geq 1/2$, the friction stresses are approximate equal (5 GPa), whereas for weak interfaces ($q < 1/2$) the friction stress is almost zero. Also the initial behaviour varies with q.

For low interface strengths, $q = 1/3$ and $q = 1/6$, the stress increases with the strain until a maximum stress, without initial overshoot. No further drop in stress is seen, Figures 2.5d and 2.5e. For these low interface strengths the structure of the interface does not change upon sliding, as is shown by the constant number of non-bcc atoms at the interface in Figure 2.6a. Since the interaction between Fe and X atoms is weak for these interfaces, the two grains with flat interfaces can easily slide over each other. This sliding occurs as an almost rigid motion of the $X^{(3)}$-grain with respect to the Fe-grain. The Fe-atoms at the interface move away from the nodes in the misfit dislocation structure, leading to a displacement of this misfit dislocation structure to the left with respect to the Fe-crystal.

For medium and strong interfaces, $q \geq 1/2$, the stress also monotonically increases with strain until a maximum stress level is reached at which the transition to sliding occurs. This transition stress decreases from 11 to 7 GPa for $q = 1$ to $q = 1/2$. However, as can be seen from the increase in the number of non-bcc atoms at the interface in Figure 2.6a, at this maximum stress the structure of the interface starts to change completely. For $q = 1$ this is shown in Figure 2.6b. Whereas the top panel shows the initially flat interface with misfit dislocations, the bottom panel shows the situation after considerable sliding has taken place ($\gamma = 0.2$). This atomic structure with significant mixing clearly illustrates the earlier mentioned tendency of an FeX crystal with $q > 1/2$ to form a compound. For these interfaces the interaction between Fe and X is strong, preventing sliding. The stress builds up at the interface until it is high enough to trigger mixing at the interface. This mixed interface structure can easily slide. This is because in this case sliding does not occur by two surfaces sliding over each other. Instead a gradual displacement across the mixed layer is seen, as is shown by the marked atoms in green in Figure 2.6b.

Note that the small modulation on the stress-strain lines before sliding is an artefact of the simulation. Given the applied strain rate, the period of this modulation is about 50 ps. The sound waves that are generated by starting the strain rate will travel at a speed of about 4000 m/s, which means that they will traverse approximately 200 nm in one modulation period. This is on the same order as the x and z lengths of the system. Very likely periodicity and reflection effects of these waves are responsible for this modulation. This explanation is supported by the fact that a 10 times slower strain rate leads to the same modulation time and a considerably smaller modulation amplitude. It is quite clear that the modulation is no thermal noise: the pattern is explicitly repetitive and looks the same for any number of dislocations present (coloured curves in Figure 2.5).

Noticeable effects from the dislocations in the system are seen in Figures 2.5a, 2.5b and 2.5c for medium and strong interfaces ($q \geq 1/2$). Upon impingement on the interface they reduce the maximum stress levels reached before interface sliding sets in. The stress reduction is stronger if the initial number of dislocations increases. This is most clearly seen for the strongest interface, Figure 2.5a. This stress reduction is attributed to the fact that the impinged dislocations locally modify the structure of the interface. Apparently

(a) $q = 1$

(b) $q = 2/3$

(c) $q = 1/2$

(d) $q = 1/6$

(e) $q = 1/3$
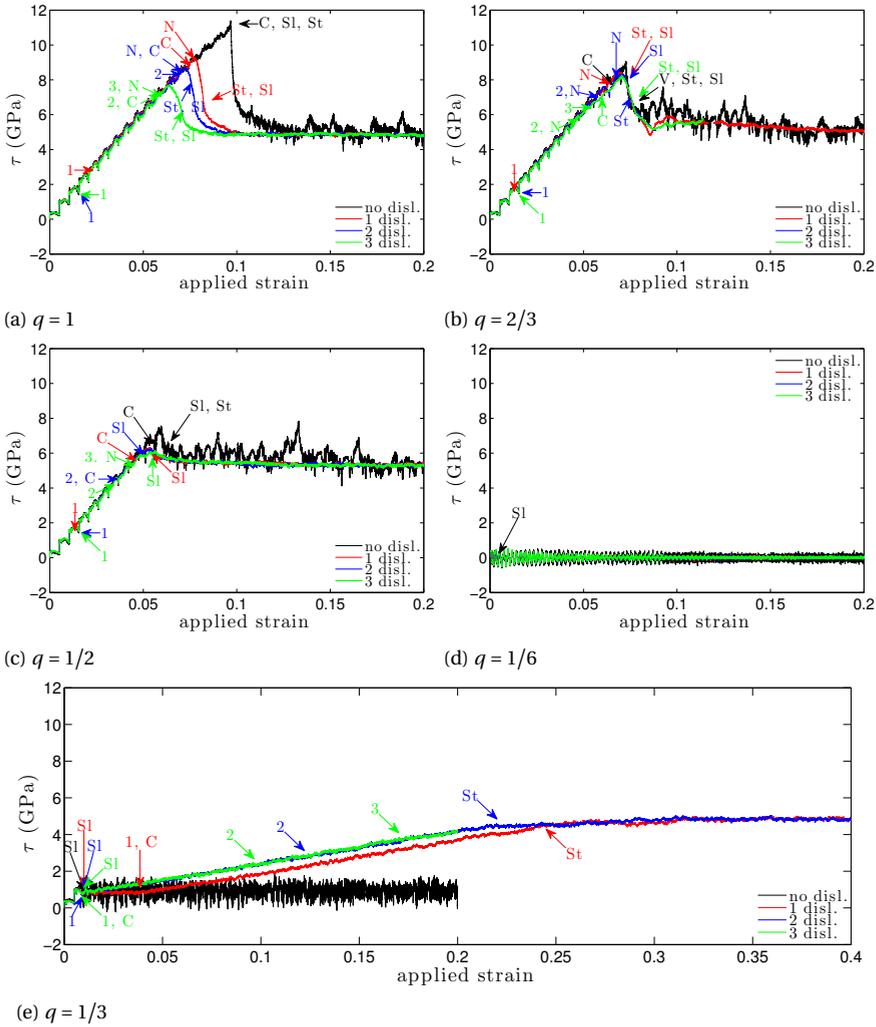
Figure 2.5: Shear stress versus applied strain for Fe–X[(3)] systems with different interface strengths loaded in shear, with $\dot{\gamma} = 10^8 \, \text{s}^{-1}$. The arrows indicate the events of interest, 1: dislocation #1 in interface, 2: dislocation #2 in interface, 3: dislocation #3 in interface, N: dislocation nucleated from interface, Sl: interface sliding, C: interface structure starts to change, St: initial structure of interface has disappeared. The figures show that for a strong interface, $q \geq 1/2$, imping dislocations on the interface facilitate interface sliding, whereas for a weak interface, $q = 1/3$, imping dislocations make it harder for the interface to slide. For $q = 1/6$ the interface slides at such low stress levels that the critical resolved shear stress on the dislocations to start moving is never reached.
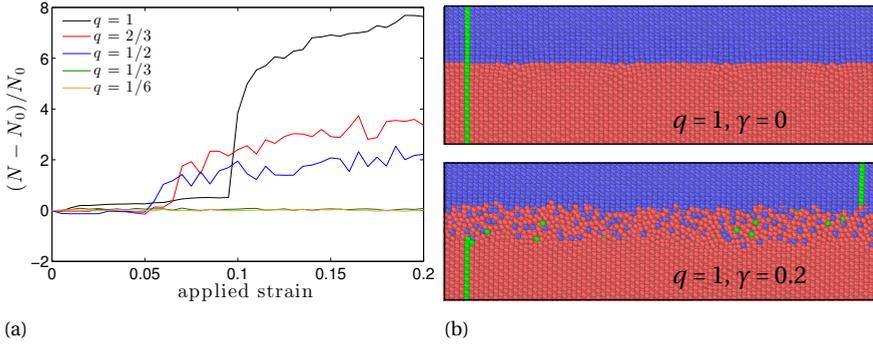
Figure 2.6: Increase in number of non-bcc atoms at the interface, N, relative to the initial number of non-bcc atoms at the interface, N_0, for Fe-X$^{(3)}$ systems with different interface strengths (a). For $q \geq 1/2$ the number of non-bcc atoms increases upon interface sliding, resulting in a completely changed interface structure. Atoms at the initial flat interface (b, top figure) show mixing upon sliding due to the strong interatomic potential (b, bottom figure). Atoms in red are Fe atoms, atoms in blue are X$^{(3)}$ atoms. The atoms in green are marked to show the gradual displacement through the interface layer upon mixing. The picture frames are chosen such that the green atoms are visible in both pictures.

this structure change facilitates the onset of sliding, which is why the sliding starts at lower maximum stress levels for increasing numbers of dislocation impingements. Note, however, that in all cases sliding sets in long after the first dislocation has entered the interface.

Interestingly, for a weaker interface, $q = 1/3$, impinging dislocations delay rather than facilitate interface sliding, Figure 2.5e. Without dislocations, the interface already slides at a relatively low stress of less than 1 GPa, without changing the structure of the interface (black curve). Impinging dislocations, however, modify the interface structure, as shown in Figure 2.8. The interface structure initially consists of a cross-structure of misfit $\{100\}\langle 100 \rangle$ dislocations with the bcc structure continuing from one grain into the other grain in between those misfit dislocations, Figure 2.8, top. Upon impingement of the dislocation into the interface the interface structure changes, as is shown in the other rows of Figure 2.8. This leads to a system with a very low apparent stiffness and ultimately the same stress levels are reached as those for the stronger interfaces (5 GPa) to continue interface sliding (coloured curves in Figure 2.5e).

For the weakest interface, $q = 1/6$, the strength has approached its lower limit: the interface slides at such low stress levels that the critical resolved shear stress on the dislocations to start moving is never reached.

Not just the energy of an interface, also its structure determines its strength. A comparison of the interface energies of the different systems, as given in Table 2.2, might suggest that an Fe–X$^{(3)}$ system with $q = 1/3$ is stronger than an Fe–X$^{(2)}$ system with $q = 1/6$. However, when both systems are sheared, the semi-coherent Fe–X$^{(3)}$ system shows interface sliding, while the fully coherent Fe–X$^{(2)}$ system can be sheared to much higher stress and strain levels without sliding, until dislocations are nucleated from the interface into the Fe grain leading to a completely damaged structure, Figure 2.9.

The results for dislocation/interface interactions for Fe-X$^{(3)}$ interfaces are summarised
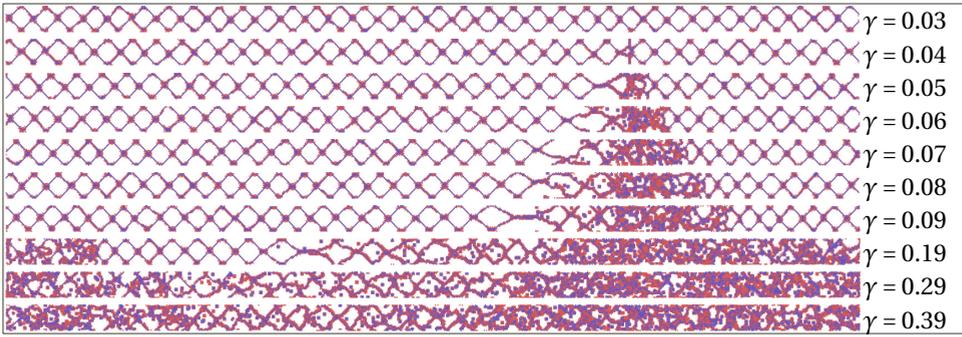
Figure 2.7: Time evolution of the interface structure for Fe–X$^{(3)}$ system with $q = 1/3$. Top three rows: before, when and after a dislocation has entered ($\gamma = 0.03$, $\gamma = 0.04$, $\gamma = 0.05$, respectively). The impinging dislocation locally modifies the interface structure, which initially consists of a regular network of misfit dislocations. Bottom seven rows: this change in structure spreads further over the interface in two directions, leading to an increase in stress while the interface continues to slide. When the structure is completely changed, $\gamma \geq 0.29$, the interface slides at constant stress, as shown in Figure 2.5e. Only those atoms are shown that are not in a bcc-structure, according to the adaptive common neighbour analysis as implemented in Ovito [24]. Atoms in red are Fe atoms, blue atoms are X$^{(3)}$ atoms.
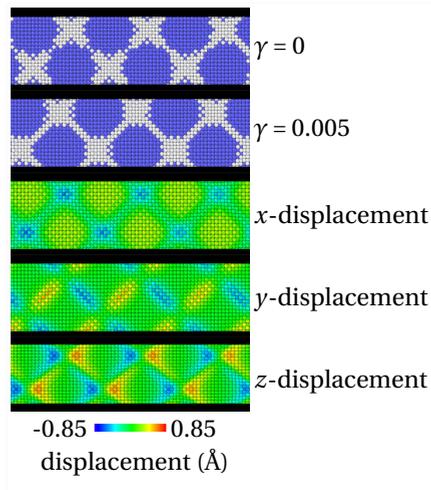
Figure 2.8: Top view of Fe-atoms at the interface for the Fe–X$^{(3)}$ system with $q = 1/6$. In the top two figures the structure according to the adaptive common neighbour analysis as implemented in Ovito [24] is shown. Atoms in blue have the bcc-structure, atoms in grey have an unknown structure. In the lowest three figures the displacements of the atoms in x, y and z directions are shown.
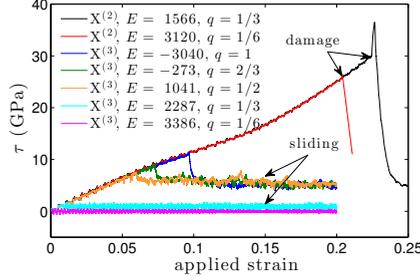
Figure 2.9: Shear stress versus applied shear strain for Fe–$X^{(2)}$ and Fe–$X^{(3)}$ systems with different interface energies (E in mJ/m^2). The figure shows that the semi-coherent Fe–$X^{(3)}$ interfaces show interface sliding, while the fully coherent Fe–$X^{(2)}$ interfaces resist significantly larger strains, even when they are higher in energy.

in Table 2.5.

2.4. DISCUSSION

From our simulations we observe that the coherency of the interface determines its dislocation accommodation capability. When a dislocation is accommodated in an interface, the interface is locally sheared. For perfect coherent interfaces the shear stress of the interface is much higher than for semi-coherent interfaces, making it much harder for dislocations to locally shear the interface and move into the interface. This was therefore only seen for very low interface strengths (Fe–$X^{(1)}$, $q = 1/4$) or at higher stress levels (Fe–$X^{(2)}$, $q \leq 1/2$). For semi-coherent interfaces (Fe–$X^{(3)}$) multiple dislocations can be accommodated in the interface.

The positive influence of the interface strength on dislocation transmission, as found by Shimokawa *et al.* [4], is only seen for the coherent Fe-$X^{(1)}$ interfaces if the $q = 1/4$ and $q = 1/2$ cases are considered. For the weakest of the two interfaces, $q = 1/4$, the dislocation is accommodated in the interface and eventually a twin grows into the precipitate, whereas for the higher interface strength the dislocation is directly transferred into the precipitate. When higher interface strengths are considered, however, a negative influence of interface strength on slip transfer is found. This coincides with the strength model by Hoagland *et al.*, since the coherency stress is higher for a higher value of q and, resulting from that, the stress that needs to be applied to make the dislocation transfer the interface is higher as well.

For the other precipitate materials no slip transfer is seen at all. The dislocations are trapped at the interface. In the mechanism described by Wang *et al.* this implies that the applied stress is not large enough to compact the spread dislocation core in the interface to allow slip transmission. However, in our case, as shown for the coherent Fe-$X^{(2)}$ interfaces, it is the stiffness of the precipitate that prevents slip transfer.

Twin formation is a well known mechanism during deformation of steel. Experimental determination of the location in a material where twins start to form and the mechanism by which they form, is difficult, however. In our simulations we did observe twin formation from the interface in a situation where the interface was weaker than the sur-

Table 2.5: Summary of results for the Fe-X$^{(3)}$ interface. q defines the pair interaction strength between Fe and X$^{(3)}$ (see Equation 2.4). The first column (# D) lists the number of edge dislocation initially present in the lower crystal (Fe). The table shows the main events observed and the applied shear strains at which the events occur (in parentheses):

- sliding: the upper grain (X$^{(3)}$) starts to slide w.r.t. the lower grain (Fe) along the interface,
- change: the structure of the interface starts to change,
- abs. change: the structure of the interface starts to change after dislocation absorption from impact point of dislocation(s),
- D immobile: dislocations stay immobile.

# D	q = 1/6	q = 1/3	q = 1/2	q = 2/3	q = 1
0	sliding (0.005)	sliding (0.010)	change sliding (0.060)	change sliding (0.073)	change sliding (0.096)
1	sliding (0.005) D immobile	sliding (0.010) abs. change	abs. change sliding (0.054)	abs. change sliding (0.070)	abs. change sliding (0.078)
2	sliding (0.005) D immobile	sliding (0.010) abs. change	abs. change sliding (0.054)	abs. change sliding (0.070)	abs. change sliding (0.073)
3	sliding (0.005) D immobile	sliding (0.010) abs. change	abs. change sliding (0.054)	abs. change sliding (0.070)	abs. change sliding (0.064)

rounding material. The impingement of a dislocation on this weak interface gave rise to a local stress and strain state at the interface which promoted twin formation. In a real material this specific situation might not occur, but twins may be generated in other situations, either from the interface or from within the bulk.

The set-up for our simulations, with the y-direction much smaller than the x- and z-direction, is chosen to reduce the computational time with respect to a system with a y-dimension comparable to the x- and z-dimensions. This choice, however, has an influence on the nucleation process of dislocations. Where in large systems dislocations would nucleate as a loop, this is suppressed by the small y-dimension. In our simulations dislocations are nucleated mainly as straight edge segments. We have repeated the simulations with a y-dimension up to 8 times larger, and these simulations did indeed show nucleation of dislocation loops instead of straight edge segments. The overall qualitative behaviour discussed in this study, however, is not found to be affected by increasing the thickness of the slab. As mentioned earlier, only for the case of an Fe-X$^{(2)}$ interface with $q = 1/2$ and one dislocation a qualitatively different behaviour is found when the thickness is increased, indicating that the nucleation stress is somewhat influenced by the thickness.

Interfaces are known to absorb, emit, transmit or reflect dislocations. Interfaces can also slide or migrate under loading [25–29]. In this work we do observe these dislocation interface reactions, depending on the interface strength and structure and the precipitate stiffness. Interface sliding is also observed, but only for semi-coherent interfaces. Van Swygenhoven *et al.* [27] showed that excess free volume plays a dominant role in interface sliding. For our coherent Fe-X$^{(1)}$ and Fe-X$^{(2)}$ interfaces there is no excess free volume at the interface, while there is for the Fe-X$^{(3)}$ interface. Sliding of Fe-X$^{(1)}$ and Fe-X$^{(2)}$ interfaces is therefore only possible if the whole X grain would rigidly translate with respect to the Fe grain. When there are misfit dislocations at the interface, as is the case for the Fe-X$^{(3)}$ interfaces described in this study, the misfit dislocations can move along the interface, thus leading to sliding. When the interface is non-coherent and consists of a layer with locally very complex atomic arrangements, which could be obtained by rotating the X grain around the y-axis, the excess free volume allows atomic displacements at the interface which can lead to sliding of one grain with respect to the other. Normal interface migration, which is observed for grain boundaries in polycrystalline materials, is not observed. Grain boundary migration occurs when atoms of one grain at the grain boundary adjust their positions to the orientation of the other grain, which leads to a migration of the interface. Since our interfaces are between two different materials, with already identical orientation, this process can not occur in this work.

In summary, it is the combination of interface strength, interface structure and precipitate stiffness that determines the dislocation/interface interaction. Whether dislocations are transmitted, reflected or adsorbed at an interface is determined by the combination of these three factors.

2.5. CONCLUSIONS

Molecular dynamics simulations of dislocation/interface interactions in Fe under the application of a shear load yield the following results:

- The interface strength is a combination of the pair interaction between atoms

across the interface and the structure at the interface, resulting from the structure and the orientation of the grains, the misfit in lattice constant, and the applied shear.

- The studied systems, with two equally oriented grains, have a coherent interface if there is no lattice misfit and a semi-coherent interface if there is a lattice misfit. A semi-coherent interface consists of non-coherent parts, the misfit dislocations, and coherent parts in between those dislocations.

- A dislocation moves easily into a semi-coherent interface, while it does not move easily into a coherent interface, even when this is much higher in energy.

- For a coherent iron/precipitate interface where the critical resolved shear stress for dislocation motion in the second grain is not the limiting factor (Fe–X$^{(1)}$), the interface strength determines how effectively an interface prevents slip transfer. The stronger the interface the more effectively slip transfer is (temporarily) prevented. A weak interface however, shows no direct slip transfer. Instead a twin is nucleated from the interface.

- For a stiff precipitate (X$^{(2)}$ and X$^{(3)}$) no slip transfer occurs. The precipitate itself is an efficient barrier for slip transfer. Dependent on the coherency and the strength of the interface, one or multiple dislocations can be accommodated inside the interface.

- For a coherent interface between iron and a stiff precipitate (Fe-X$^{(2)}$), the higher the interface strength, the higher the stress the system can undergo before it is completely damaged due to repeated nucleation of dislocations from the interface.

- For a coherent interface between iron and a stiff precipitate (Fe-X$^{(2)}$) with a low interface strength, only a single interface and lattice dislocation are nucleated, leading to interface sliding.

- A semi-coherent interface always shows interface sliding.

- For strong semi-coherent interfaces impinging dislocations reduce the maximum stress a system can undergo before sliding occurs.

- Weak semi-coherent interfaces become more resistant to interface sliding due to impinging dislocations.

Interface decohesion is not seen in the present study, due to the imposed boundary and loading conditions. From the obtained results however, some predictions regarding the susceptibility to interface decohesion under other loading directions can be made. The character of the interface, whether it is coherent, semi-coherent or non-coherent, determines for a large part the interaction of dislocations with the interface. For iron/precipitate interfaces where the precipitate is stiff, a coherent interface will not show interface decohesion, since it is not capable to accommodate dislocations inside the interface. Dislocations pile up at the interface, leading to a stress concentration, which results in the nucleation of many dislocations in the iron grain and damage all over the material. A semi-coherent interface however, is capable of accommodating multiple dislocations and weak semi-coherent interfaces slide easily. These interfaces are therefore expected to show decohesion easily. For strong semi-coherent interfaces a high stress concentration is needed to locally modify the interface, which then results in sliding. These interfaces are therefore expected also to show decohesion only at high

stress concentrations. A large pile-up of dislocations could lead to such a high stress concentration and therefore lead to decohesion. The behaviour of these systems under tensile loading will be the subject of further study.

2

REFERENCES

[1] A. Elzas and B. J. Thijsse, *Dislocation impacts on iron/precipitate interfaces under shear loading*, Modelling and Simulation in Materials Science and Engineering **24**, 85006 (2016).

[2] J. P. Hirth and J. Lothe, *Theory of Dislocations*, 2nd ed. (John Wiley & Sons, Inc., New York, 1982).

[3] Z. Pan and T. J. Rupert, *Damage nucleation from repeated dislocation absorption at a grain boundary*, Computational Materials Science **93**, 206 (2014).

[4] T. Shimokawa, T. Oguro, M. Tanaka, K. Higashida, and T. Ohashi, *A multiscale approach for the deformation mechanism in pearlite microstructure: Atomistic study of the role of the heterointerface on ductility*, Materials Science and Engineering A **598**, 68 (2014).

[5] R. G. Hoagland, T. E. Mitchell, J. P. Hirth, and H. Kung, *On the strengthening effects of interfaces in multilayer fcc metallic composites*, Philosophical Magazine A **82**, 643 (2002).

[6] J. Wang, R. G. Hoagland, X. Y. Liu, and A. Misra, *The influence of interface shear strength on the glide dislocation- interface interactions*, Acta Materialia **59**, 3164 (2011).

[7] J. Wang, A. Misra, R. G. Hoagland, and J. P. Hirth, *Slip transmission across fcc/bcc interfaces with varying interface shear strengths*, Acta Materialia **60**, 1503 (2012).

[8] J. Wang, *Atomistic Simulations of Dislocation Pileup: Grain Boundaries Interaction*, Jom **67**, 1515 (2015).

[9] L. Malerba, M. C. Marinica, N. Anento, C. Björkas, H. Nguyen, C. Domain, F. Djurabekova, P. Olsson, K. Nordlund, A. Serra, D. A. Terentyev, F. Willaime, and C. S. Becquart, *Comparison of empirical interatomic potentials for iron applied to radiation damage studies*, Journal of Nuclear Materials **406**, 19 (2010).

[10] J. J. Möller and E. Bitzek, *Comparative study of embedded atom potentials for atomistic simulations of fracture in α-iron*, Modelling and Simulation in Materials Science and Engineering **22**, 045002 (2014).

[11] P. A. Gordon, T. Neeraj, M. J. Luton, and D. Farkas, *Crack-tip deformation mechanisms in α-Fe and binary Fe alloys: An atomistic study on single crystals*, Metallurgical and Materials Transactions A: Physical Metallurgy and Materials Science **38 A**, 2191 (2007).

[12] M. I. Mendelev, S. Han, D. J. Srolovitz, G. J. Ackland, D. Y. Sun, and M. Asta, *Development of new interatomic potentials appropriate for crystalline and liquid iron*, Philosophical Magazine **83**, 3977 (2003).

[13] G. J. Ackland, M. I. Mendelev, D. J. Srolovitz, S. Han, and A. V. Barashev, *Development of an interatomic potential for phosphorus impurities in α-iron*, Journal of Physics: Condensed Matter **16**, S2629 (2004).

[14] Y. Mishin, *Interatomic Potentials for Metals*, in *Handbook of Materials Modeling*, edited by S. Yip (Springer Netherlands, 2005) pp. 459–478.

[15] G. Simmons and H. Wang, *Single crystal elastic constants and calculated aggregate properties: a handbook* (M.I.T. Press, 1971).

[16] C. Kittel, *Introduction to Solid State Physics*, 6th ed. (John Wiley & Sons, Inc., New York, 1986).

[17] D. R. Lide, *CRC Handbook of Chemistry and Physics, 85th Edition*, CRC Handbook of Chemistry and Physics, 85th Ed No. v. 85 (Taylor & Francis, 2004).

[18] M. Acet, H. Zähres, E. F. Wassermann, and W. Pepperhoff, *High-temperature moment-volume instability and anti-Invar of γ-Fe*, Physical Review B **49**, 6012 (1994).

[19] R. A. Johnson, *Alloy models with the embedded-atom method*, Physical Review B **39**, 12554 (1989), arXiv:arXiv:1011.1669v3 .

[20] M. A. Tschopp and D. L. McDowell, *Structures and energies of Σ3 asymmetric tilt grain boundaries in copper and aluminium*, Philosophical Magazine **87**, 3147 (2007).

[21] *LAMMPS Molecular Dynamics Simulator*, http://lammps.sandia.gov.

[22] A. Stukowski, *Visualization and analysis of atomistic simulation data with OVITO–the Open Visualization Tool*, Modelling Simul. Mater. Sci. Eng. **18**, 015012 (2009).

[23] D. Hull and D. J. Bacon, *Introduction to Dislocations*, 5th ed., Vol. 1 (Elsevier Ltd, 2011) pp. 128–144.

[24] A. Stukowski, *Structure identification methods for atomistic simulations of crystalline materials*, Modelling Simul. Mater. Sci. Eng. **20**, 45021 (2012), arXiv:1202.5005 .

[25] J. W. Cahn, Y. Mishin, and A. Suzuki, *Coupling grain boundary motion to shear deformation*, Acta Materialia **54**, 4953 (2006).

[26] M. Velasco, H. van Swygenhoven, and C. Brandl, *Coupled grain boundary motion in a nanocrystalline grain boundary network*, Scripta Materialia **65**, 151 (2011).

2

[27] H. van Swygenhoven and P. M. Derlet, *Grain-boundary sliding in nanocrystalline fcc metals,* Physical Review B **64**, 1 (2001).

[28] N. Ahmed and A. Hartmaier, *Mechanisms of grain boundary softening and strain-rate sensitivity in deformation of ultrafine-grained metals at high temperatures,* Acta Materialia **59**, 4323 (2011).

[29] S. S. Quek, Z. Wu, Y. W. Zhang, and D. J. Srolovitz, *Polycrystal deformation in a discrete dislocation dynamics framework,* Acta Materialia **75**, 92 (2014).

3

COHESIVE LAW DESCRIBING CRACK GROWTH AT IRON/PRECIPITATE INTERFACES

Single dislocations and dislocation pile-ups at crystalline interfaces cause stress concentrations. This can lead to decohesion of the interfaces under tensile loading. To describe this decohesion quantitatively, a cohesive law for planar crack growth at iron/precipitate interfaces is developed. This cohesive law is based on a universal description of the adhesive energy for different interfaces. Only a single scaling factor c must be applied to convert the prediction based on this universal adhesive energy into the actual traction-separation behaviour during crack growth. This scaling factor takes into account the atomic strain and relaxations. The cohesive law derived here can be implemented in a Discrete Dislocation Plasticity framework to describe crack growth at a larger scale. The method presented in this paper for the derivation of a cohesive law can be applied to other material combinations showing brittle crack growth as well.

3.1. Introduction

Interfaces in iron and other metals act as a barrier for dislocation motion. Due to the crystallographic mismatch across an interface and the atomic disorder in an interface, there is a discontinuity of slip planes across the interface, which impedes dislocation motion. When dislocations encounter an interface, they can be stopped, transmitted, reflected, broken up, dissolve or even spawn new dislocations. By reducing the grain size, a material can be made stronger, since dislocations encounter more obstructing interfaces and slip is reduced, as is expressed by the Hall-Petch relation [2]. According to this relation the yield strength of a polycrystalline material is proportional to $d^{-1/2}$, where d is the mean grain size. The mechanical properties of a material, however, can also be negatively influenced by interface effects. Hindered dislocation motion at an interface leads to a pile-up of dislocations at this interface, which, in turn, gives a stress concentration. If this stress concentration becomes high enough, this can lead to decohesion of the interface, which leads to the formation of a void and eventually, by coalescence of multiple voids, can lead to the formation of a macroscopic crack. Advanced high-strength steels and other multiphase alloys show limited ductility due to interface decohesion.

In this work we derive a cohesive law for interface decohesion during crack growth. This cohesive law can be implemented in a cohesive zone model to improve existing larger-scale models such as Discrete Dislocation Plasticity. To derive this cohesive law we study the interaction of single edge dislocations and dislocation pile-ups with interfaces between an α-iron crystal and a precipitate. With Molecular Dynamics simulations (MD) we study for different orientations and different numbers of dislocations how and when interface decohesion occurs under tensile loading. From these simulations the cohesive law for interface decohesion during crack growth is derived. The influence of pure shear loading on dislocation-interface interactions was previously studied [3]. In forthcoming work the combination of tensile and shear loading, mixed-mode loading condition, will be considered, as well as crack nucleation.

Based on effective displacement and effective traction data, various constitutive relationships for interface decohesion, such as cubic polynomial [4], trapezoidal [5], smoothed trapezoidal [6], exponential [7], linear softening [8], and bilinear softening [9] have been defined. Most of these relationships are a phenomenological characterisation of the zone where separation takes place along the interface, and not a description of the true atomic separation process between the interfaces. Only the exponential potential based on the work of Rose *et al.* [10] is based on information from atomistic calculations.

Gall *et al.* [11] have fitted their results from MD simulations to three models by Needleman [4, 12], Tvergaard and Hutchinson [13] and Tvergaard and Hutchinson [13–15] for an aluminium-silicon interface. For aluminium Yamakov *et al.* [16, 17] developed a cohesive zone representation of intergranular fracture based on results of MD simulations. Zhou *et al.* [18] determined the traction-separation behaviour for a pre-cracked bimetal with a weak interface under mixed mode loading conditions. In [19] the effect of elastic constant mismatch was also included. Using MD simulations on single-crystal aluminium, Krull and Yuan [20] confirmed that steady-state crack growth can be described with the exponential traction-separation relation by Needleman [21], while crack initiation shows a non-uniform traction-separation relation. For a symmetric tilt

grain boundary in copper Paliwal and Cherkaoui [22] developed a mixed-mode cohesive zone law for non-planar crack growth.

In all of the above studies the growth of a pre-existing crack in an fcc material is considered, while in the current study we focus on cracks nucleated from stress concentrations due to a dislocation pile-up in a bcc material.

We start our study by determining the adhesive energy as function of separation for different interfaces and interface strengths. In this work the term 'adhesive energy' is used for the separation energy between two crystal halves as rigid blocks, i.e. without any relaxation of the atomic positions. From these different adhesive energy curves we are able to derive a universal adhesive energy curve by scaling. The predicted traction-separation behaviour derived from this energy curve, called 'template curve', is compared with real traction curves from MD simulations. To obtain a match between the template curve and the calculated traction-separation relations from the MD simulations, the template curve is scaled with a scaling factor c. We find that only one universal scaling factor is needed for all iron/precipitate interfaces. In this way we are able to derive a cohesive law for interface decohesion, where the different interfaces are only characterised by a different adhesion energy. The small deviations in behaviour between the calculated curves for different interfaces and different numbers of dislocations in the pile-up and the predicted curve obtained by scaling the template curve show the atomic-scale details. These are no longer important for Discrete Dislocation Plasticity models. We expect the method to be universal and also applicable for other bimetal interfaces. The thus derived cohesive law captures the essence of separation physics.

This paper is organised as follows. In Section 3.2 we describe the choice of the materials (Section 3.2.1), the set-up of our simulations (Section 3.2.2), and the calculation method for interfacial traction and separation (Section 3.2.3). The derivation of the traction versus separation relation from the adhesion energy is given in Section 3.3 and this relation is compared with the results from tensile simulations in Section 3.4, which leads to the formulation of a cohesive law. The results are discussed in Section 3.5 and conclusions are presented in Section 3.6.

3.2. Method

For different iron/precipitate interfaces we derive a cohesive law describing the traction-separation relation upon decohesion of the interface under the influence of a tensile load. In order to capture the effects of atomic relaxation, the results are then compared with MD simulations under tensile loading for different interface orientations and different numbers of dislocations interacting with the interface.

3.2.1. Material description

To describe iron in our simulations a potential had to be chosen that accurately describes both edge dislocations in iron and the structures far from equilibrium resulting from dislocation pile-up/interface interactions. To describe a single edge dislocation in iron, the potential developed by Malerba *et al.* [23], optimised to describe interstitials and vacancy defects, is a reliable choice. However, since in the present study not just single edge dislocations but also pile-ups of dislocations interacting with interfaces are stud-

ied, structures far from equilibrium are expected for which this potential is less appropriate [24]. Studies of crack tips [24, 25] have shown that both 'potential 2' developed by Mendelev *et al.* [26] and the potential developed by Ackland *et al.* [27] are reliable potentials for this type of study. Although they are both derived from nearly the same input data and predict nearly the same material properties, this does not result in a qualitatively same description of material behaviour at a crack tip [25]. In this study iron is described with the EAM-potential by Ackland *et al.* [27].

In the EAM-format the potential energy per atom i is given by

$$U_i = F(\rho_i) + 1/2 \sum_j \phi_{ij}(r), \tag{3.1}$$

where F is the embedding energy as function of the local electron density ρ_i and ϕ_{ij} gives the pair interaction between the atom and the surrounding atoms j as function of their distance r. The local electron density is made up of the contributions ψ to the electron density by the atoms j surrounding atom i,

$$\rho_i = \sum_j \psi_j(r). \tag{3.2}$$

F, ϕ and ψ are relatively simple functions, parametrised for Fe.

In general practice, precipitates in iron are stiffer than the matrix, which hinders dislocation transfer. They also form semi- or non-coherent interfaces with the matrix, depending on their different lattice constant and/or crystal structure. As a model material for a precipitate we create an artificial material X, which is stiffer and has a different lattice constant than iron. Furthermore, we vary the orientations of both the Fe and the X grains, which gives rise to different interface structures. The potential to describe the precipitate material, material X, is based on the Fe-potential. In this study, X is chosen to be material $X^{(3)}$ from [3]. This precipitate material has a 10 % larger lattice constant than Fe and a 49 % larger Young's modulus.

Similar to [3] the pair interaction between Fe and X is a linear combination of the individual pair interactions in Fe and X, as defined by

$$\phi_{Fe-X} = q(\phi_{Fe} + \phi_X), \tag{3.3}$$

where the factor q is varied between 1/6 and 1 to obtain different pair interaction strengths. The combination of a given Fe–X pair interaction and a given orientation of the two grains determines the interface strength, in the absence of additional defects at the interface.

3.2.2. SETUP
The Fe/X system is schematically shown in Figure 3.1. The system size is dependent on the orientation but on average equals $165 \times 4.4 \times 110$ nm. The system is periodic in x and y. To determine the adhesive energy of the interface as function of normal separation, one crystal is rigidly displaced with respect to the other crystal and the energy is determined as function of separation.

Different interfaces are studied. In iron the (100) plane is the typical cleavage plane. Similarly to the orientations chosen by [28], we here study this (100) crack plane, with
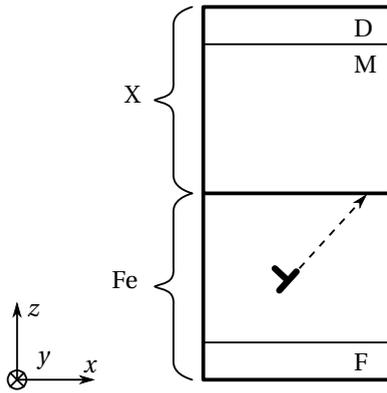
Figure 3.1: Setup of the simulations. For the study of the adhesive energy as function of separation, the X grain is rigidly displaced with respect to the Fe grain (without dislocations). For the study of dislocation-interface interactions, atoms in region F are kept fixed, atoms in region M are mobile atoms, whose positions are updated by time integration, and the atoms in region D are moved in the z-direction with a constant strain rate of $\dot{\varepsilon} = 10^8$ s^{-1}. In the Fe grain one or multiple $\{112\}\langle111\rangle$ edge dislocations are inserted on the same slip plane.

the crack front direction in the [011] direction and the crack growth direction in the [01$\bar{1}$] direction, as well as the (110) crack plane, with the crack front direction along [1$\bar{1}$0] and the crack growth direction along [001]. Either the iron grain, or the precipitate grain, or both are oriented along these directions. To obtain different interfaces and study their influence on dislocation-interface interactions, we rotate one of the grains around the crack front direction. Table 3.1 shows the different orientations of the Fe and X grains. A tensile load is applied to the system shown in Figure 3.1, so that the edge dislocations, which are initially placed in the Fe grain, move towards the interface. To avoid boundary effects, the dislocations are placed with their dislocation line along a periodic direction of the simulation box. In all cases, this is the (expected) crack front direction, which is the y-direction of the simulation box. The studied slip system is therefore the $\{112\}\langle111\rangle$ slip system.

For the tensile MD simulations, zero, one or multiple edge dislocations are inserted in the iron grain on the same (2$\bar{1}$1) slip plane. To create an edge dislocation in the system a half plane of atoms perpendicular to the slip plane is removed and the system is let to equilibrate. The first dislocation is placed 100 Å underneath the interface, the second dislocation is placed 300 Å underneath the interface and the third dislocation is placed 500 Å underneath the interface. Atoms in the lower 10 Å are kept fixed, region F in Figure 3.1. On atoms in the upper 10 Å, region D, a tensile displacement is imposed with a constant strain rate $\dot{\varepsilon}$ of 10^8 s^{-1}. For the mobile atoms, region M, time integration is performed at 1 K with a Nosé-Hoover thermostat, using a time step of 5 fs. Prior to loading, the system is equilibrated at 1 K for 100 ps. The stress σ that results from the applied strain is calculated by summing the resulting forces on the atoms in region D and dividing this by the area of the system in the x, y-plane.

The very low temperature of 1 K was chosen to get a clear view on the dislocation-interface interactions. At higher temperature these details would be hidden by thermal vibrations.

The interface structures are created using the method described by Tschopp and Mc-Dowell [29]. Of all the possible structures created, a structure of which the interface energy has the highest number of occurrences is chosen. The MD-simulations are performed with LAMMPS [30, 31] and the structures are visualised with OVITO [32].

Table 3.1: Orientations of the Fe and X grains giving the 11 different interface structures. The angle between the dislocation glide direction and the interface is given as ζ in Fe and η in X. All interfaces have been given a label just to identify them. Interfaces with the same letter(s) have one grain in the same orientation.

		Fe			X			ζ (°)	η (°)
		x	y	z	x	y	z		
(100) Fe	S1	$[01\bar{1}]$	$[011]$	$[100]$	$[11\bar{1}]$	$[011]$	$[2\bar{1}1]$	35.3	0.00
	S2	$[01\bar{1}]$	$[011]$	$[100]$	$[01\bar{1}]$	$[011]$	$[100]$	35.3	35.3
	S3	$[01\bar{1}]$	$[011]$	$[100]$	$[\bar{2}3\bar{3}]$	$[011]$	$[31\bar{1}]$	35.3	60.5
	S4	$[01\bar{1}]$	$[011]$	$[100]$	$[21\bar{1}]$	$[011]$	$[1\bar{1}1]$	35.3	90.0
(100) X	Fe1	$[11\bar{1}]$	$[011]$	$[2\bar{1}1]$	$[01\bar{1}]$	$[011]$	$[100]$	0.00[a]	35.3
	Fe3	$[\bar{2}3\bar{3}]$	$[011]$	$[31\bar{1}]$	$[01\bar{1}]$	$[011]$	$[100]$	60.5	35.3
	Fe4	$[21\bar{1}]$	$[011]$	$[1\bar{1}1]$	$[01\bar{1}]$	$[011]$	$[100]$	90.0[b]	35.3
(110) Fe	X1	$[001]$	$[1\bar{1}0]$	$[110]$	$[111]$	$[1\bar{1}0]$	$[11\bar{2}]$	54.7	0.00
	X2	$[001]$	$[1\bar{1}0]$	$[110]$	$[113]$	$[1\bar{1}0]$	$[33\bar{2}]$	54.7	29.5
	X3	$[001]$	$[1\bar{1}0]$	$[110]$	$[001]$	$[1\bar{1}0]$	$[110]$	54.7	54.7
	X4	$[001]$	$[1\bar{1}0]$	$[110]$	$[\bar{1}\bar{1}2]$	$[1\bar{1}0]$	$[111]$	54.7	90.0

[a] The dislocation is placed in the $[1\bar{1}1]$ direction, giving an angle between slip plane and crack plane of 70.6°.

[b] The dislocation is placed in the $[\bar{1}\bar{1}1]$ direction, giving an angle between slip plane and crack plane of 19.4°.

3.2.3. LOCAL BEHAVIOUR

To calculate the local response in the interface region, the region is divided into multiple bins along the x-direction. Each bin is then divided in two: one half above the interface, one half underneath, as shown in Figure 3.2. The width of each bin, δx, was chosen to be 8.8 Å. When the [100] direction is perpendicular to the interface, each bin then holds five atomic planes. The height of the bins, δz, was chosen as 20 Å. As is shown further on in this paper, in Figure 3.9, this height of the bin ensures that the total interface region, which is the region in which significant extra strain is seen with respect to the bulk, is taken into account in the calculations made over each bin.
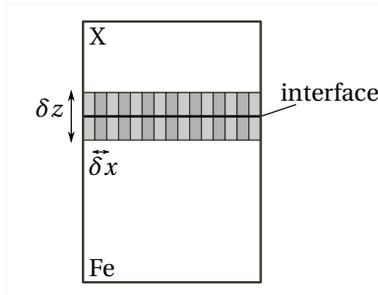
Figure 3.2: Division of interface region into bins.

For every bin k the stress is calculated as the average of the stresses on the N_k atoms j in the bin, according to

$$\sigma_{\alpha\beta k} = \frac{1}{N_k}\sum_{j=1}^{N_k}\sigma_{\alpha\beta kj}. \tag{3.4}$$

The normal traction T_n in a bin is equal to the $\alpha\beta = zz$ component of this average stress in the bin.

The normal separation u_n between the bins above and underneath the interface is calculated at the time of interest t as the increase in normal distance between the centers of mass (c) of these bins

$$u_n(t) = z_c^X(t) - z_c^{Fe}(t) - (z_c^X(0) - z_c^{Fe}(0)), \tag{3.5}$$

where z_c^{Fe} is the z-position of the center of mass of the Fe-bin, below the interface, and z_c^X is the z-position of the X-bin, above the interface. For simplicity of notation T_n and u_n do not carry a subscript designating the bin to which they apply. The values for T_n and u_n were calculated every 100 time steps (500 fs) as an average over 10 time steps (50 fs).

3.3. ADHESIVE ENERGY

The adhesive energy of an interface is defined as [10]

$$E_{ad}(u_n) = [E(u_n) - E(\infty)]/(2A), \tag{3.6}$$

where E is the total potential energy, A the cross-sectional area, and u_n the separation of the two crystals, i.e. the distance between the two surfaces making up the interface relative to the distance in equilibrium. In the present study the adhesive energy is calculated as a function of the distance by rigidly displacing one crystal with respect to the other crystal and determining the energy of the system and the separation. No atomic relaxation is performed. Figure 3.3 shows the adhesive energy as function of u_n for five different S$_2$ interfaces, resulting from five different choices of q.
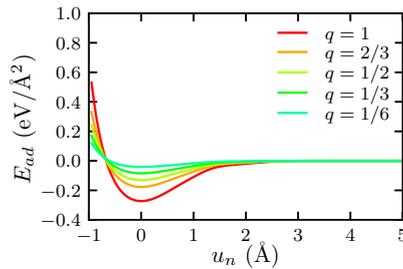
Figure 3.3: Adhesive energy versus separation for the S$_2$ system and different values of q. The separation is given with respect to the equilibrium distance in contact.

3.3.1. UNIVERSAL ADHESIVE ENERGY FUNCTION

By scaling both the energy and the separation, Rose *et al.* [10] obtained an analytical expression for a universal adhesive energy curve. In [10] the separation is scaled with the Thomas-Fermi screening length λ and for bimetallic interfaces with the average $(\lambda_1 + \lambda_2)/2$ of the Thomas-Fermi screening lengths of the two metals. In the present study we choose to scale the separation with the equilibrium pair interaction length α for Fe and X, the position of the Fe-X pair potential ϕ^{Fe-X} minimum. For the current EAM-potential $\alpha = 2.84$ Å. The scaled separation u^* is given by

$$u^* = \frac{u_n}{\alpha}. \tag{3.7}$$

The adhesive energy is, similar to [10], scaled by its minimum value ΔE. We find from Figure 3.3 that the scaled adhesive energy E_{ad}^*, given by

$$E_{ad}(u_n) = \Delta E \cdot E_{ad}^*(u^*), \tag{3.8}$$

follows a universal curve, independent of the pair interaction strength between iron and the precipitate as determined by q, as can be seen in Figure 3.4.
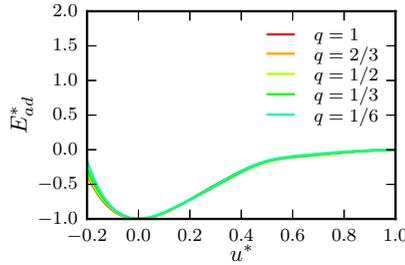
Figure 3.4: Scaled adhesive energy versus scaled separation for system in S_2 orientation and different values of q.

Rose *et al.* [10] give an analytic fit of a universal adhesive energy function to data for ten bimetallic contacts,

$$E_{ad}^* = -(1 + \beta u^*) \exp(-\beta u^*), \tag{3.9}$$

with $\beta = 0.90$ and $u^* = 2u_n/(\lambda_1 + \lambda_2)$.

Inspired by this result, we use an extended version of this function in the present work,

$$E_{ad}^* = -(1 + \theta u^* + \mu(\theta u^*)^3) \exp(-\theta u^*), \tag{3.10}$$

with θ and μ fitting parameters and $u^* = u_n/\alpha$ according to Equation 3.7. For $\mu = 0$ this is similar to the description by Rose *et al.*. This description for the universal adhesive

energy obeys the relations

$$E_{ad}^*(0) = -1,$$
$$E_{ad}^* \to 0 \text{ for } u^* \to \infty,$$
$$E_{ad}^{*\,'}(0) = 0,$$
$$E_{ad}^{*\,'} \to 0 \text{ for } u^* \to \infty. \tag{3.11}$$

Figure 3.5 shows a fit of Equation 3.10 to the data for all orientations given in Table 3.1. The curve is fitted to datapoints with $E_{ad}^* \leq 0$, giving $\theta = 5.29$ and $\mu = -0.06$.
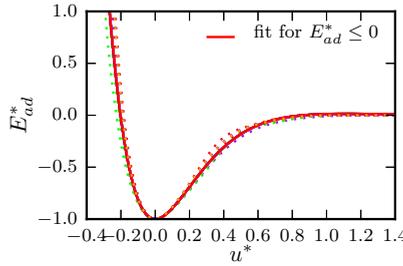
Figure 3.5: Fit of Equation 3.10 to scaled adhesive energy versus scaled separation for all orientations given in Table 3.1. The curve is fitted to datapoints with $E_{ad}^* \leq 0$. $\theta = 5.29$ and $\mu = -0.06$.

3.3.2. TRACTION-SEPARATION

The mechanical response of an interface can be described by a potential that gives the dependence of traction on separation [4],

$$V(u_n, u_t, u_b) = \int_0^u \left[T_n du_n + T_t du_t + T_b du_b \right]. \tag{3.12}$$

The traction is given by a traction field **T**, in force per unit of reference area, and can have both normal and shearing components. The traction is assumed to depend only on the displacement difference between two points A and B at opposite sides of the interface, $\Delta\mathbf{u}_{AB}$.

Defining a right-hand coordinate system **n**, **t**, **b**, with **n** normal to the interface and **t** and **b** parallel to the interface, the separation and traction can be decomposed into

$$u_n = \mathbf{n} \cdot \Delta\mathbf{u}_{AB} \qquad u_t = \mathbf{t} \cdot \Delta\mathbf{u}_{AB} \qquad u_b = \mathbf{b} \cdot \Delta\mathbf{u}_{AB}$$
$$T_n = \mathbf{n} \cdot \mathbf{T} \qquad T_t = \mathbf{t} \cdot \mathbf{T} \qquad T_b = \mathbf{b} \cdot \mathbf{T} \tag{3.13}$$

From the universal adhesive energy a potential to describe the mechanical response of the interface can be derived. Similar to the description by Needleman [21], this potential is given by

$$V(u^*) = \Delta E + \Delta E \cdot E_{ad}^*(u^*). \tag{3.14}$$

With the description of the universal adhesive energy according to Equation 3.10, this potential can be written as

$$V(u_n) = \Delta E - \Delta E \left[1 + \theta \frac{u_n}{\alpha} + \mu \left(\theta \frac{u_n}{\alpha} \right)^3 \right] \exp \left(-\theta \frac{u_n}{\alpha} \right), \tag{3.15}$$

where, as before, u_n is the separation normal to the interface, and only normal traction and separation are considered ($u_t \equiv u_b \equiv 0$).

The traction following from this potential is given by

$$T_n(u_n) = \frac{dV}{du_n} = \theta \frac{\Delta E}{\alpha} \left[\mu \left(\theta \frac{u_n}{\alpha} \right)^3 - 3\mu \left(\theta \frac{u_n}{\alpha} \right)^2 + \theta \frac{u_n}{\alpha} \right] \exp \left(-\theta \frac{u_n}{\alpha} \right). \tag{3.16}$$

In the next section we will compare this so-called template curve for the traction versus separation behaviour with traction-separation curves following from MD simulations.

3.4. TENSILE SIMULATIONS

Loading the systems described in Table 3.1 in tension leads to failure. The specific behaviour is dependent on the orientation, as well as on the pair interaction between Fe and X, given by the factor q in Equation 3.3. For $q \leq 1/3$ a crack is nucleated at the interface, leading to decohesion between the two crystals. For $q \geq 1/2$ either no crack is nucleated, or a crack is nucleated below the interface, in the iron grain. In this case the pair interaction between Fe and Fe atoms is weaker than between Fe and X atoms, given the value of q. To describe interface decohesion and to develop a cohesive law describing crack growth, in the remainder of this study only $q = 1/3$ is considered.

3.4.1. GLOBAL STRESS

Dislocation impingement on the interface leads to a local stress concentration. This local stress concentration in turn leads to crack nucleation and interface decohesion at lower global stress σ_D, i.e. the stress developing in region D in Figure 3.1 during application of the strain rate, than without dislocations, as shown in Figure 3.6 for the S_2 system. The global stress increases until failure occurs in the form of interface decohesion. The stress then drops to zero. This drop takes place at lower applied strain when more dislocations impinge on the interface.

Knowing that the number of impinging dislocations has a large effect on the global stress-strain behaviour, we will now look at the local traction-separation behaviour and see how this depends on the position along the interface, the number of impinging dislocations, and the orientation of the grains making up the interface.

3.4.2. LOCAL TRACTION

The local traction as function of the local separation is determined for every bin along the interface, as explained in Section 3.2.3. The local stress, from which the traction along the interface is derived, is influenced by the stress fields of impinging dislocations in a large region surrounding the impingement position, as illustrated in Figure 3.7a.
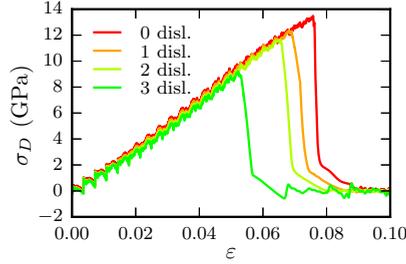
Figure 3.6: Global stress versus applied strain for S_2 system and $q = 1/3$ with different numbers of dislocations impinging on the interface during tensile loading with $\dot{\varepsilon} = 10^8$ s^{-1}.

Here the traction along the interface is shown after impingement of three dislocations and before crack nucleation. In a region as large as 50 bins around the impingement position, dislocations influence the traction at a specific moment in time. However, the traction versus separation behaviour, developing over different time intervals for different positions along the interface, is modified by impinging dislocations only in a much smaller region around the impingement position. This is shown in Figure 3.7b, which displays the traction versus separation in different bins surrounding the crack nucleation point N when 3 dislocation impinge on the interface. At the crack nucleation point, which in this case is also the dislocation impingement position, every new dislocation that impinges on the interface changes the traction-separation curve, as shown by the initial oscillations in the curve for point N in Figure 3.7b. A point 10 Burgers vectors away from the nucleation point, which means a shift of only 3 bins to either left or right, exhibits the same traction versus separation behaviour as at a remote point R, lying half of the simulation box width away from N, as illustrated in Figure 3.7c. Only within a region of 10 Burgers vectors to both sides of the nucleation point the traction versus separation behaviour is influenced by crack nucleation. At all other points along the interface a similar crack growth behaviour is observed.

A comparison of the traction versus separation curves for simulations with different numbers of dislocations impinging on the interface, shows that the local response at a remote point R during crack growth is not influenced by the number of impinging dislocations, Figure 3.7d. This is a significant result, enabling the modelling of crack growth in a Discrete Dislocation Plasticity framework, independent of the crack nucleation process.

3.4.3. Cohesive law

We will next investigate whether the template curve based on the universal adhesion energy derived in Section 3.3.2 for rigid-block separation can also be used to describe interface decohesion as we have seen in our MD simulations. The idea behind this is to look upon the template curve as the essential trend in mechanical separation of the system under study, and to represent stress, strain and atomic relaxation in the interface region simply by one or two scaling factors for modifying the template curve.

3
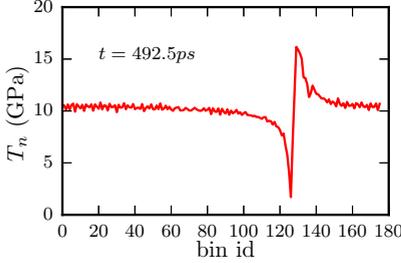
(a) Local traction along interface at one particular moment during loading, for a simulation where three dislocations interact with the interface. The stress is shown after dislocation impingement and before crack nucleation.
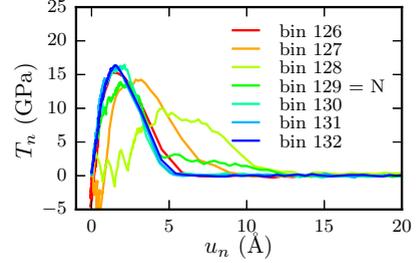
(b) Traction versus separation during crack nucleation and growth, calculated at different bins surrounding crack nucleation point N, for a simulation where three dislocations interact with the interface. Neighbouring bins have a centre-to-centre distance of 8.8 Å
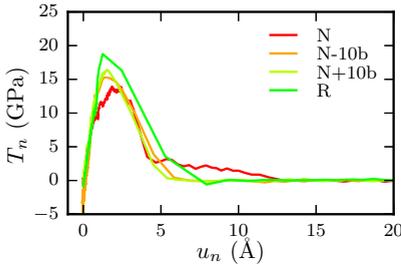
(c) Traction versus separation during crack nucleation and growth, calculated in four bins along the interface, for a simulation where three dislocations interact with the interface. N: nucleation point, $N - 10b$: $10b$ left from nucleation point, $N + 10b$: $10b$ right from nucleation point, R: remote point.
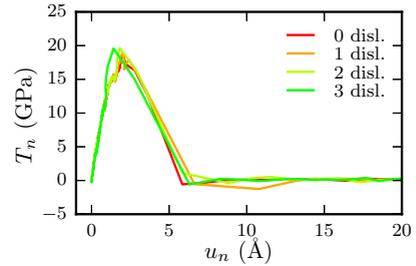
(d) Traction versus separation during crack growth, calculated at remote point R. Results are shown for simulations with different numbers of dislocations interacting with the interface.

Figure 3.7: Traction for the S_2 interface loaded in tension, with $q = 1/3$.

For the S_4 system Figure 3.8a shows the calculated traction versus separation during crack growth and the template curve of Equation 3.16 with the values for θ (5.29) and μ (-0.06) following from a fit to the scaled adhesive energy for datapoints with $E^*_{ad} \leq 0$.
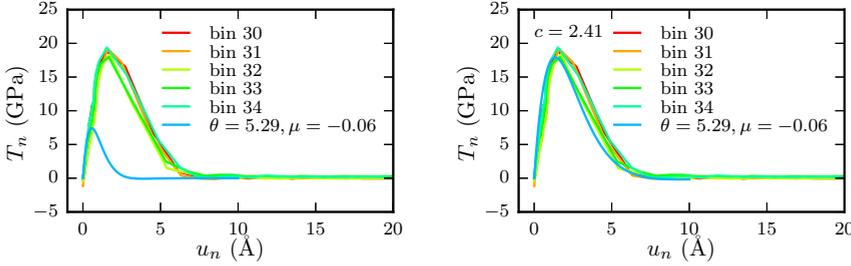
(a) Template curve for traction versus separation (light blue) compared with MD results for different bins.

(b) Template curve scaled with c to match $\overline{T_n^{max}}$ of all bins except those in a region of 15 bins around the crack nucleation point.

Figure 3.8: Traction versus separation as calculated in different bins far from the nucleation point and as predicted from the adhesive energy, for the system in S_4 orientation loaded in tension, with $q = 1/3$, and three dislocations impinging on the interface.

The adhesive energy curves shown in Figure 3.3 are calculated by rigidly displacing one crystal with respect to the other and calculating the energy. No energy minimisation is performed, i.e. the atoms are not allowed to relax. However, in realistic simulations of the tensile loading of a bi-crystal, surface relaxation will take place upon separation. Furthermore, upon tensile loading of the bi-crystal strain will develop in both crystals. Therefore our template curve underestimates the traction and separation. During tensile loading, the strain in the system is not equally distributed along the height of the system, as shown in Figure 3.9. Close to the interface, the region where the traction and separation are calculated in this work, the system experiences a larger strain than in the bulk. Since the separation u_n is calculated as the distance between the centers of mass of the two bins above and below the interface, this separation will significantly increase when there is more strain in the bins. The separation at maximum traction and at total decohesion will therefore be larger than given by the template curve. Since not only separation is accomplished upon tensile loading of the system, but also strain in the system is induced, the traction will increase as well. Following our hypothesis, we find that a good match between the traction versus separation as calculated from the MD simulations and the template curve can be obtained by scaling both the predicted traction and predicted separation of the template curve by a factor c. The scaling factor c is determined by

$$c(T_n^{max})_{template} = (\overline{T_n^{max}})_{MD}, \tag{3.17}$$

where $(\overline{T_n^{max}})_{MD}$ is the average maximum traction during the MD simulation of all the bins along the interface except those in a region of 15 bins at both sides of the crack nucleation point.

The cohesive law for crack growth is then given by

$$T_n(u_n) = c\theta \frac{\Delta E}{\alpha} \left[\mu \left(\theta \frac{u_n}{c\alpha} \right)^3 - 3\mu \left(\theta \frac{u_n}{c\alpha} \right)^2 + \theta \frac{u_n}{c\alpha} \right] \exp \left(-\theta \frac{u_n}{c\alpha} \right). \qquad (3.18)$$
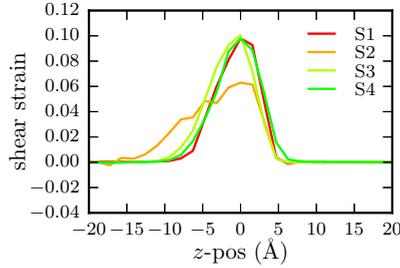
Figure 3.9: Shear strain as calculated along the height of the system for Fe/X interface loaded in tension, with $q = 1/3$ and different orientations. The strain is calculated with the routine built-in in Ovito [32] by comparing the atomic positions just before decohesion and before loading of the system. The average shear strain of the atoms at a certain z−position is plotted in the figure with respect to the initial z−position.

Figure 3.10 shows the scaling factor c as well as the well depth ΔE for the different interfaces. The scaling factor c has been determined for different numbers of dislocations and, where multiple dots of the same color are shown, for simulations executed with different initial velocity distributions too check the sensitivity to this type of random variations. As can be seen in Figure 3.10b, different initial velocity distributions lead to a small variation in the obtained value for c. This variation however, is smaller than the variation in c resulting from different numbers of impinging dislocations.

(a) ΔE
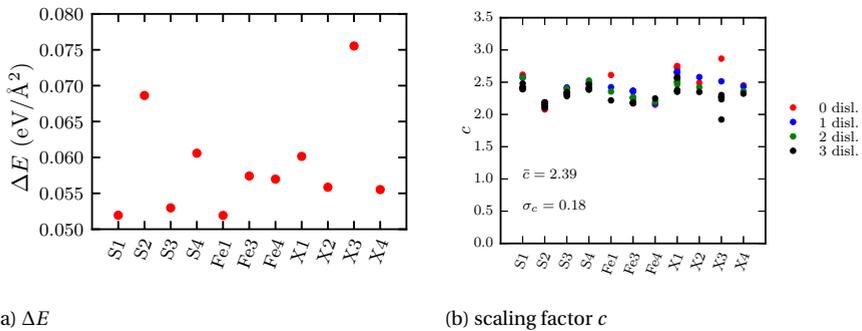
(b) scaling factor c

Figure 3.10: Well depth ΔE and scaling factor c for different orientations and, for c, also for different numbers of dislocations and simulations with different initial velocity distributions.

To determine if our prediction, following from scaling of the template curve, gives an accurate cohesive law for interface decohesion during crack growth, we investigate

how well this prediction matches the results from the MD simulations. To make this practical, we determine the horizontal deviations (in u_n) between the curves at full and half maximum predicted traction, the latter in the upward and downward slopes of the curves, as shown in Figure 3.11. To determine the deviation, the average deviation in all the bins, except those in a region of 15 bins at both sides of the crack nucleation point, is determined. Figures 3.12a, 3.12c and 3.12e show the deviations d_{up}, d, and d_{down} for all orientations and different numbers of dislocations.
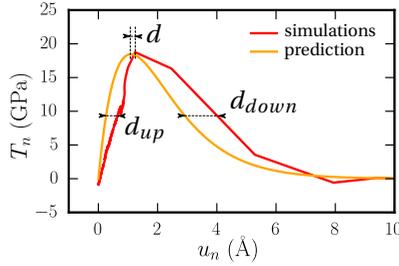
Figure 3.11: Example of determination of deviations d_{up}, d, and d_{down} between prediction and MD simulations.

Since the standard deviation σ_c of the scaling factor c is only 0.18, Figure 3.10b, we test if our cohesive law has an even stronger universality. We therefore determine a universal scaling factor for Fe/X interfaces based on the individual scaling factors obtained for all simulations. For every orientation an average scaling factor is determined from the average scaling factor per number of dislocations. The universal scaling factor is the average scaling factor of all the orientations, $c = 2.39$. The deviations between the calculated curves from the MD simulations and the predicted curves with this universal scaling factor are shown in Figures 3.12b, 3.12d and 3.12f, where it can be seen that indeed a universal scaling factor can be applied in our cohesive law, with only a minor influence on the results.

3.4.4. NUMBER OF IMPINGING DISLOCATIONS

The influence of the number of impinging dislocations on the traction-separation behaviour becomes clear when the values of d_{up}, d, and d_{down} are compared, Figure 3.12. For d_{up}, Figure 3.12b, there is no significant difference for different numbers of dislocations. For d and d_{down}, Figures 3.12d and 3.12f, we see a difference between different numbers of impinging dislocations. Dislocations that impinge on the interface increase the local stress concentration, leading to decohesion at a lower global applied strain than without impinging dislocations, Figure 3.6. The fewer dislocations impinge on the interface, the more the interface region is strained before decohesion. The traction-separation curve becomes broader at the top, leading to a larger deviation d at the top. The deviation on the downward slope of the curve d_{down} shows more pronounced variation, not only for different numbers of dislocations, but also for different simulations with the same numbers of dislocations. We conclude that in general the shape of the

3

(a) d_{up}

(b) d_{up}

(c) d

(d) d

(e) d_{down}

(f) d_{down}
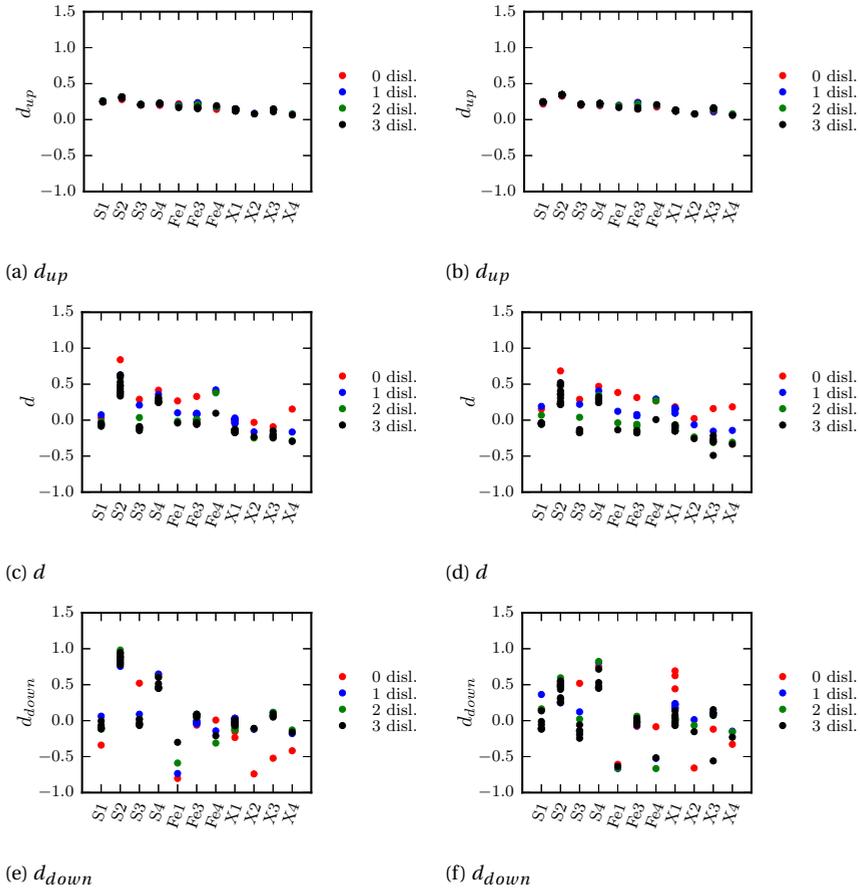
Figure 3.12: Deviations between predictions and MD results of traction versus separation for different orientations and for different numbers of dislocations. On the left-hand side results are shown with different scaling factors for every simulation. Results at the right-hand side are obtained with the average scaling factor $c = 2.39$.

traction-separation curve is quite well predicted by our cohesive law.

The universal scaling factor c has been obtained from results for 11 interfaces and up to three dislocations. With a fourth dislocation initially present in the system, the deviations between the prediction with this value of c and the calculated traction-separation curves are not much different from those with three dislocations, Figure 3.13. In these cases the crack at the interface nucleates before the fourth dislocation has impinged on the interface. Apparently, for these interfaces at this temperature the interface can hold only three dislocations and the stress concentration reached with these three dislocations is high enough to lead to crack nucleation.

(a) d (b) d_{down}
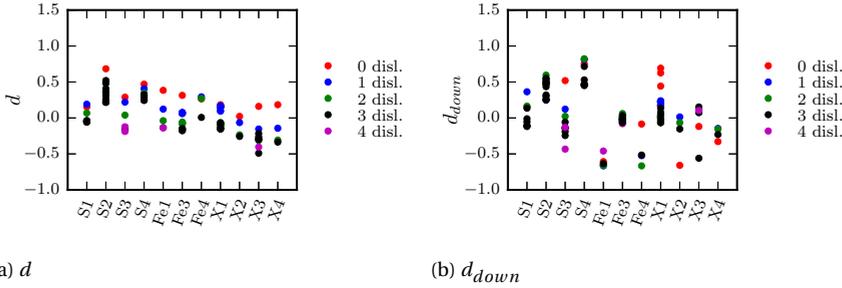
Figure 3.13: Deviations d and d_{down} between predictions with the universal scaling factor c = 2.39 and MD results of traction versus separation for different orientations and for different numbers of dislocations. The results with four dislocations were not included in the determination of the universal scaling factor.

3.4.5. INTERFACES

The orientations of the grains influence the interface strength and therefore the response during crack growth. The interface bonding is stronger for S_2 and S_4 systems than for S_1 and S_3 systems, Figure 3.14. When comparing the traction versus separation for these four systems, Figure 3.15, one not only notices a higher maximum traction for the S_2 and S_4 systems than for the S_1 and S_3 systems, but also a broader peak. Because of the stronger bonding not only more work has to be done to separate the two surfaces, reflected in a higher traction, but also more atomic rearrangements occur before decohesion sets in. This can be seen in an increase in the number of non-bcc atoms, as determined by the common neighbour analysis routine implemented in Ovito [32], at the interface, Figure 3.16. These atomic rearrangements occur at constant stress while the separation is increased, which leads to the broader peak for these systems. For the S_2 system the number of non-bcc Fe atoms shows a large increase, at around 750 ps, long before decohesion sets in, which occurs at around 1400 ps, as shown by the increase of X atoms. This increase in Fe atoms is caused by reorientation of interface atoms. Initially the S_2 system has an ordered structure of misfit dislocation at the interface, with the bcc structure continuing from the Fe grain into the X grain in between those misfit dislocations. A detailed picture is shown in Figure 7 from [3]. During tensile loading the structure changes, initially only in the, softer, Fe grain. For both Fe and X the number of non-bcc atoms has to increase in order to form two surfaces. In the X grain the structure only changes upon decohesion. For the S_4 system the number of non-bcc atoms shows a

large increase around 600 ps indicating a large amount of atomic rearrangements. Upon total decohesion the number of non-bcc atoms reduces again when two surfaces are formed.

Due to the larger number of atomic rearrangements in the S_2 and S_4 systems, the peak of the traction versus separation curve becomes broader, which leads to a larger deviation d between the prediction and the curves as calculated from the MD simulations for these systems, as is shown in Figure 3.12d, compared with the S_1 and S_3 systems. Because of the broader peak of the curve, the downward part of the curve is shifted to the right, leading to a larger deviation d_{down}, as is shown in Figure 3.12f.
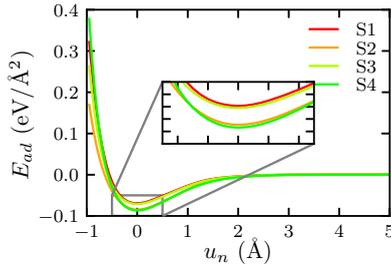
Figure 3.14: Adhesive energy versus separation for the Fe/X interface for four different orientations of the X grain and q=1/3.
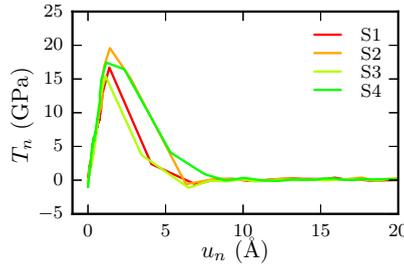
Figure 3.15: Traction versus separation at remote point R for different orientations, $q = 1/3$, and three dislocations impinging on the interface, during tensile loading with $\dot{\varepsilon} = 10^8$ s^{-1}.

3.4.6. IMPINGEMENT POSITION OF THE DISLOCATIONS

For all interfaces up to now the intersection point of the dislocation slip plane and the interface was kept constant throughout the simulations. Changing the dislocation slip plane, did not significantly influence the results. The spread in the results for different impingement positions was comparable to the spread in results with different initial velocities. Therefore, the results obtained with different impingement positions were included in the dataset used to determine the universal scaling factor c.

(a) Fe   (b) X
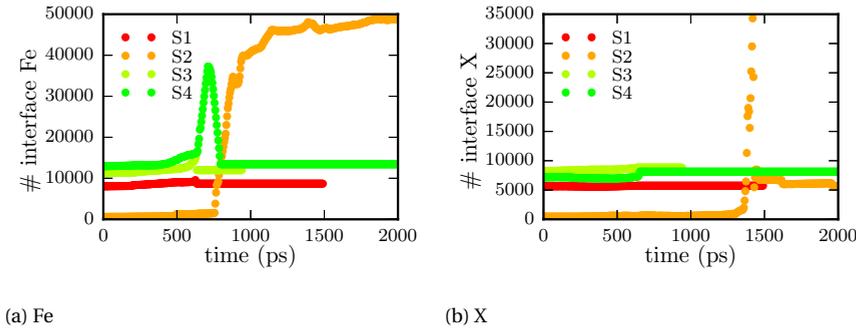
Figure 3.16: Number of non-bcc atoms at the interface versus time for four different systems. At around 600 ps decohesion occurs for the S_1, S_3 and S_4 systems, which can be seen in the increase in both Fe and X atoms. At around 700 ps the structure of the interface for the S_2 system begins to change, leading to a much larger amount of non-bcc Fe atoms at the interface. Only around 1400 ps decohesion occurs at this interface, which goes together with an increase in non-bcc X atoms at the interface.

3.5. DISCUSSION

Number of dislocations   A cohesive law for crack growth should ideally be completely independent of crack nucleation. How the crack is nucleated should not influence the crack growth. Therefore, the number of dislocations that impinge on the interface, leading to the local stress concentration, which in turn leads to crack nucleation, should also not influence the cohesive law for crack growth. However, the number of impinging dislocations does influence our results. As is shown in Figure 3.12d, for most orientations the deviation d between the top of the predicted curve and the curves calculated from the MD simulations reduces with the number of impinging dislocations. The reason for this is that when more dislocations impinge on the interface, decohesion occurs at lower global stress and applied strain than with fewer or no dislocations. As is previously explained in Section 3.4.4, a higher global stress and strain leads locally, on account of the finite size of the bins over which this is calculated, to higher strain as well. Also, more atomic rearrangements occur in the interface region for higher global stress and strain, leading to a broader peak of the traction-separation curve and therefore a larger d. If truly local separation between the surfaces making up the interface would be calculated in the bins, the result would always be the same. However, due to the finite size of the bins, a smaller global strain with more dislocations can lead to a smaller local strain in the bins and therefore a smaller calculated separation. This in turn leads to a smaller deviation between prediction and MD simulations. The differences in deviation between different numbers of dislocations are small however, and converge to a constant value for four initial dislocations, indicating that the cohesive law for crack growth has then become independent of crack nucleation.

Universality   For the universal adhesive energy curve to be truly universal, the curves for different orientations, different interface strengths, and different materials should coincide. Figure 3.5 shows for $q = 1/3$ that the differences between the curves for different orientations are very small. In Figure 3.4 it is shown for the S_2 orientation that for

different interface strengths, given by different values of q, only a very small deviation is seen between the curves, in the compressive part of the curve. For the other orientations the deviations between such curves are of the same size as, or smaller than those between curves for different orientations and therefore also small. For different materials it was already shown by Rose *et al.* [10] that various bi-metallic interfaces follow a universal adhesive energy curve. Our version of the universal adhesive energy curve has an extra factor μ which gives a better description of the curvature of the curve for large separation.

Separation calculation   In this study, with $q = 1/3$, cracks exhibit a planar growth along the interface. The separation between the crack surfaces is determined from the distance between the centers of mass of the bins above and underneath the interface. All Fe atoms are assumed to be at the lower crack surface, while all X atoms are assumed to be at the upper crack surface. Therefore, the division of atoms between bins above and bins underneath the interface is determined *a priori* based on their atom type. Although this assumption is generally quite well obeyed, and only up to 1% of the Fe atoms stick to the upper crack surface after decohesion, for the S_4 and X_1 orientations up to 5% of the Fe atoms stick to the upper crack surface. This influences the separation calculation. When a considerable number of Fe atoms stick to the upper crack surface, the calculated separation will be smaller than the actual separation. For non-planar crack growth a dynamical division in bins should be applied, as is done in e.g. [22].

Size   In our simulations the y-dimension is much smaller than the x- and z-dimensions, to keep the computational time within reasonable bounds. When dislocations are nucleated in the system, which is found in several simulations, the small y-size forces them to nucleate as a straight edge segment instead of as a dislocation loop. This influences the global stress and strain when decohesion occurs. The calculated local traction and separation values during crack growth, however, are independent of the crack nucleation behaviour and therefore also independent of dislocation nucleation. The cohesive laws derived in this study are therefore not influenced by the small y-dimension.

Validity   The cohesive law derived in this work is based on an extended version of the universal adhesive energy function by Rose *et al.* [10]. This extended version gives a closer fit to the scaled adhesive energy versus scaled separation data than can be obtained with Equation 3.9. As a result, the cohesive law based on this extended version gives a description of the traction versus separation relation closer to the simulation data than can be obtained with a cohesive law based on Equation 3.9, especially after the maximum normal traction is reached. Equation 3.18 allows the traction to become zero at finite separation, whereas a cohesive law based on Equation 3.9 only asymptotically moves towards zero and real decohesion is than never reached. Although, as shown in Figure 3.5, Equation 3.10 gives a good description of the simulation data for small negative separations, the functional form of Equation 3.10 (and as a result Equation 3.18) shows an unphysical maximum (minimum) in E^*_{ad} (T_n) at a larger negative separation. The cohesive law derived in this work therefore should only be used to describe the decohesion behaviour for separations ranging between small negative values towards full

decohesion is reached at $u_n = c\alpha(3 + \sqrt{9 - 4/\mu})/(2\theta)$.

3.6. CONCLUSIONS

In this study we have used MD simulations to derive a traction versus separation relation $T_n(u_n)$, or cohesive law, for crack growth along different Fe/X interfaces. Here X denotes a bcc precipitate with a 10% larger lattice constant and a 49% larger Young's modulus than Fe. 11 different interface orientations were studied, and one particular value was selected for the Fe/X cross interaction strength. In addition to the simple case without initial dislocations, also crack growth after impingement of one to four dislocations was investigated. Note that a cohesive law applies locally, at the interface. It can not be used to describe the applied tensile stress-strain curves.

It turns out that one single analytic form of the cohesive law, Equation 3.18, can be used for all cases that we have studied. This straightforward mathematical form, inspired by the classical work by Rose and co-workers [10], allows fast computation in, e.g., Discrete Dislocation Plasticity modelling, where such a cohesive law will be a natural ingredient. The level of universality of our cohesive law is best examined by looking at the five parameters in Equation 3.18:

- The scaling length α is taken as the position of the Fe-X pair potential minimum in the EAM potential (2.84 Å). For every other material combination the value for α will have to be determined in the same way.

- The exponential decay factor θ (= 5.29) and the Rose-refinement prefactor μ (= −0.06) are obtained from fits of Equation 3.10 to the calculated adhesive energy data for all orientations, i.e., the energy versus separation relations under the restriction that the two crystals are separated without allowing atomic strain or relaxation ('rigid block movement'). For other systems than Fe/X one may expect that the values for θ and μ are different. However, Rose *et al.* already showed for ten bimetallic interfaces that the adhesive energy can be described with a universal curve. We do therefore expect Equation 3.10 to hold for other material combinations, with nearly the same values for θ and μ. To improve the universality of θ and μ these should be fitted to a dataset containing other material combinations as well.

- The scaling energy ΔE depends on the particular orientation of the two crystals, Figure 3.10a. For other systems than Fe/X and for other orientations the values will be different.

- The scaling factor c is perhaps the most interesting parameter in this work. We find that it is the only parameter needed to transform the simple adhesive energy curve (scaled with ΔE) into a cohesive law. In other words, operating in this way, c incorporates all effects of atomic strain and relaxation. Interestingly, the same factor c scales both the traction and the separation. Essentially this means that the effective force constant between the two separating crystal halves is unaffected by atomic strain and relaxation. It is found that the values of c for all orientations and numbers of impinging dislocations have an average $\bar{c} = 2.39$ and a standard

deviation of only σ_c = 0.18 (Figure 3.10b). For the Fe/X system this is therefore virtually a universal value. It is an interesting open question whether the same value is also universal for other systems and system types.

In this study impinging dislocations on the interface lead to crack nucleation. The global stress-strain behaviour is influenced by the number of impinging dislocations. The crack growth behaviour, for which we derived the cohesive law, is not influenced by the number of impinging dislocations. The impingement position of the dislocations on the interface also does not influence the crack growth behaviour.

The deviations d_{up}, d, and d_{down} between the prediction by the cohesive law and the actual calculations along the interface have been determined. The prediction of the upward part of the curve is very good, resulting in very small values of d_{up}. These values are also independent of the number of impinging dislocation. The deviations at the top and in the downward part of the curve, d and d_{down}, are slightly larger and are dependent on the number of impinging dislocations. These values are still smaller than 1 Å however, and converge to a limiting value when four dislocations impinge on the interface.

REFERENCES

[1] A. Elzas and B. J. Thijsse, *Cohesive law describing crack growth at iron/precipitate interfaces,* Computational Materials Science **134**, 214 (2017).

[2] J. P. Hirth and J. Lothe, *Theory of Dislocations*, 2nd ed. (John Wiley & Sons, Inc., New York, 1982).

[3] A. Elzas and B. J. Thijsse, *Dislocation impacts on iron/precipitate interfaces under shear loading,* Modelling and Simulation in Materials Science and Engineering **24**, 85006 (2016).

[4] A. Needleman, *A continuum model for void nucleation by inclusion debonding,* Journal of Applied Mechanics **54**, 525 (1987).

[5] V. Tvergaard and J. W. Hutchinson, *The influence of plasticity on mixed mode interface toughness,* Journal of the Mechanics and Physics of Solids **41**, 1119 (1993).

[6] I. Scheider and W. Brocks, *Simulation of cup-cone fracture using the cohesive model,* Engineering Fracture Mechanics **70**, 1943 (2003).

[7] A. Needleman, *Micromechanical modelling of interfacial decohesion,* Ultramicroscopy **40**, 203 (1992).

[8] H. D. Espinosa and P. D. Zavattieri, *A grain level model for the study of failure initiation and evolution in polycrystalline brittle materials. Part I: Theory and numerical implementation,* Mechanics of Materials **35**, 333 (2003).

[9] F. H. Wittmann, K. Rokugo, E. Brühwiler, H. Mihashi, and P. Simonin, *Fracture energy and strain softening of concrete as determined by means of compact tension specimens,* Materials and Structures **21**, 21 (1988).

[10] J. H. Rose, J. Ferrante, and J. R. Smith, *Universal binding energy curves for metals and bimetallic interfaces,* Physical Review Letters **47,** 675 (1981).

[11] K. Gall, M. F. Horstemeyer, M. Van Schilfgaarde, and M. I. Baskes, *Atomistic simulations on the tensile debonding of an aluminum-silicon interface,* Journal of the Mechanics and Physics of Solids **48,** 2183 (2000).

[12] A. Needleman, *An analysis of tensile decohesion along an interface,* Journal of the Mechanics and Physics of Solids **38,** 289 (1990).

[13] V. Tvergaard and J. W. Hutchinson, *The relation between crack growth resistance and fracture process parameters in elastic-plastic solids,* Journal of the Mechanics and Physics of Solids **40,** 1377 (1992).

[14] V. Tvergaard and J. W. Hutchinson, *Toughness of an interface along a thin ductile layer joining elastic solids,* Philosophical Magazine A **70,** 641 (1994).

[15] V. Tvergaard and J. W. Hutchinson, *On the toughness of ductile adhesive joints,* Journal of the Mechanics and Physics of Solids **44,** 789 (1996).

[16] V. Yamakov, E. Saether, D. R. Phillips, and E. H. Glaessgen, *Molecular-dynamics simulation-based cohesive zone representation of intergranular fracture processes in aluminum,* Journal of the Mechanics and Physics of Solids **54,** 1899 (2006).

[17] V. Yamakov, E. Saether, and E. H. Glaessgen, *Multiscale modeling of intergranular fracture in aluminum: Constitutive relation for interface debonding,* Journal of Materials Science **43,** 7488 (2008).

[18] X. W. Zhou, J. A. Zimmerman, E. D. Reedy Jr., and N. R. Moody, *Molecular dynamics simulation based cohesive surface representation of mixed mode fracture,* Mechanics of Materials **40,** 832 (2008).

[19] X. W. Zhou, N. R. Moody, R. E. Jones, J. A. Zimmerman, and E. D. Reedy Jr., *Molecular-dynamics-based cohesive zone law for brittle interfacial fracture under mixed loading conditions: Effects of elastic constant mismatch,* Acta Materialia (2009), 10.1016/j.actamat.2009.06.023.

[20] H. Krull and H. Yuan, *Suggestions to the cohesive traction-separation law from atomistic simulations,* Engineering Fracture Mechanics **78,** 525 (2011).

[21] A. Needleman, *An analysis of decohesion along an imperfect interface,* International Journal of Fracture **42,** 21 (1990).

[22] B. Paliwal and M. Cherkaoui, *An improved atomistic simulation based mixed-mode cohesive zone law considering non-planar crack growth,* International Journal of Solids and Structures **50,** 3346 (2013).

[23] L. Malerba, M. C. Marinica, N. Anento, C. Björkas, H. Nguyen, C. Domain, F. Djurabekova, P. Olsson, K. Nordlund, A. Serra, D. A. Terentyev, F. Willaime, and C. S. Becquart, *Comparison of empirical interatomic potentials for iron applied to radiation damage studies,* Journal of Nuclear Materials **406,** 19 (2010).

3

[24] J. J. Möller and E. Bitzek, *Comparative study of embedded atom potentials for atom-istic simulations of fracture in α-iron,* Modelling and Simulation in Materials Science and Engineering **22**, 045002 (2014).

[25] P. A. Gordon, T. Neeraj, M. J. Luton, and D. Farkas, *Crack-tip deformation mechanisms in α-Fe and binary Fe alloys: An atomistic study on single crystals,* Metallurgical and Materials Transactions A: Physical Metallurgy and Materials Science **38 A**, 2191 (2007).

[26] M. I. Mendelev, S. Han, D. J. Srolovitz, G. J. Ackland, D. Y. Sun, and M. Asta, *Development of new interatomic potentials appropriate for crystalline and liquid iron,* Philosophical Magazine **83**, 3977 (2003).

[27] G. J. Ackland, M. I. Mendelev, D. J. Srolovitz, S. Han, and A. V. Barashev, *Development of an interatomic potential for phosphorus impurities in α-iron,* Journal of Physics: Condensed Matter **16**, S2629 (2004).

[28] J. R. Rice, *Tensile crack tip fields in elastic-ideally plastic crystals,* Mechanics of Materials **6**, 317 (1987).

[29] M. A. Tschopp and D. L. McDowell, *Structures and energies of Σ3 asymmetric tilt grain boundaries in copper and aluminium,* Philosophical Magazine **87**, 3147 (2007).

[30] *LAMMPS Molecular Dynamics Simulator,* http://lammps.sandia.gov.

[31] S. J. Plimpton, *Fast Parallel Algorithms for Short-Range Molecular Dynamics,* Journal of Computational Physics **117**, 1 (1995).

[32] A. Stukowski, *Visualization and analysis of atomistic simulation data with OVITO–the Open Visualization Tool,* Modelling Simul. Mater. Sci. Eng. **18**, 015012 (2009).

4

COHESIVE LAWS FOR SHEARING OF IRON/PRECIPITATE INTERFACES

The behaviour of 11 differently oriented iron-precipitate interfaces under a shear load is studied with molecular dynamics simulations. We find that the behaviour depends not only on the interface orientation but also on the shear direction. Furthermore, for many interfaces the presence of a dislocation at the interface triggers a structure change in the interface, and with that completely modifies the shear behaviour. Several interface characteristics are inspected for their possibly decisive influence on the observed loading curves. However, none of these characteristics is found to correlate conclusively with the shear behaviour of the different interfaces. This indicates that actual shear behaviour is rooted in a deeper level of complexity than just depending on the properties of the initial interface. Clearly the time evolution of the interface during shearing is crucial. From the observations a comprehensive cohesive law is derived that represents the shear behaviour for every interface and for both shear directions. This cohesive law can be used in numerical methods at a larger length sale, such as discrete dislocation plasticity.

4.1. INTRODUCTION

In everyday use, interfaces in metallic microstructures are routinely subjected to stresses. Deformation and in certain cases mechanical failure are sometimes the ultimate results. Dislocations play an important role in this, but the stress response at interfaces between grains is equally important. Advanced high strength steels show limited ductility due to interface decohesion. To correctly model the material behaviour, so that the limited ductility can be explained, it is crucial to understand the interface behaviour under different loading conditions. This paper sets out to describe interface behaviour under shear loading, using large-scale atomistic simulations as principal method. Dislocation-interface interactions are part of this study. It will be shown that the same crystals but with different orientations on both sides of the interface give rise to widely different mechanical responses to shear. The ultimate purpose of this paper is not only to identify "weak" interfaces and the reasons therefor, but also to derive from the simulation results cohesive laws, which can be used in numerical methods at the next larger length scales beyond atomic, such as discrete dislocation plasticity where interfaces are modelled by cohesive zone models.

The system under study is Fe – X, with X being a material modelling a hard precipitate. Details are given later. In earlier work [2] we derived tensile traction relations $T_n(u_n)$, where T is traction, u is displacement of two points on opposite sides of the interface and n is the direction normal to the interface. Tensile loading is just one case.

In the present study we use classical molecular dynamics (MD) simulations to derive shear traction relations $T_t(u_t)$, where t is a direction parallel to the interface, for the same 11 interfaces as those studied earlier ($u_n \equiv u_b \equiv 0$, where n is the direction normal to the interface and b is a direction parallel to the interface forming a right-hand coordinate system with n and t). The shear loading is applied in two opposite directions to examine symmetry aspects in the interface behaviour. The simulations are done with and without a dislocation initially present at the interface. The main results of the present work are the cohesive laws that are derived from the observed traction data and a deeper insight in the differences between the various Fe – X interfaces.

Cohesive zone models were introduced by Barenblatt [3] and Dugdale [4], who addressed fracture as a gradual process. They assumed that there is no stress transmission between the fully separated crack surfaces, while a cohesive zone ahead of the crack continues to transmit forces between a pair of virtual surfaces. This behaviour is governed by a traction-crack opening displacement constitutive law.

Cohesive zone models can be either potential-based or non-potential-based. The most commonly implemented cohesive zone model is the potential-based model developed by Xu and Needleman [5]. Here the first derivatives of an interface potential function give the traction-separation relations. The normal and tangential behaviour are coupled, which means that both tractions depend on both the normal and tangential separation. The coupling is controlled by two coupling parameters r and q. The ratio between the work of tangential separation and the work of normal separation, $q = \phi_t/\phi_n$, determines the relative strength of the interface under mode I and mode II separation. The coupling parameter r gives the ratio between the normal separation after complete shear separation without normal traction and a characteristic length for the normal debonding process. Van den Bosch *et al.* [6] have shown that only for $r = q$ the

required tangential traction increases with increasing normal compression, as it does in friction. Furthermore, physically realistic coupling is obtained only for $q = 1$, since only then the required normal traction reduces to zero at complete shear separation. However, that implies that $\phi_t = \phi_n$ which experimental studies [7] have shown is often not true. Van den Bosch *et al.* [6] modified the Xu-Needleman cohesive zone model by allowing for $\phi_n \neq \phi_t$. This model is no longer potential-based.

Park *et al.* [8] proposed a potential-based constitutive model where fracture energies are different for the different fracture modes, which they showed is necessary to correctly simulate the mixed-mode fracturing. McGarry *et al.* [9] analysed various cohesive zone models with respect to over-closure and found that when traction-separation relations are obtained from a potential function, non-physical repulsive normal tractions can result when the work of tangential separation exceeds the work of normal separation. They proposed a number of new potential-based and non-potential-based models to control, respectively eliminate, the problem of repulsive normal tractions. Dimitri *et al.* [10] checked various models for their thermodynamical consistency and found that most produce inconsistencies at the local level, which may cause undesirable features in the global behaviour. They also proposed a reformulation of the cohesive zone model by Xu and Needleman [5] as modified by van den Bosch *et al.* [6] within a thermodynamically consistent framework.

Conventionally the parameters for a traction-separation law are obtained empirically, from polycrystalline samples. However, they then reflect the average response of many interfaces. This is therefore inappropriate as a representation of constitutive behaviour of interfacial debonding at the nano-scale. To obtain the parameters of the cohesive law to accurately describe interfacial debonding at the nano-scale atomistic simulations can be used.

Zhou *et al.* [11, 12] derived with MD simulations a cohesive zone law for crack growth at the interface of a brittle material under mixed mode loading. Only one interface was considered. Given the set-up of their simulations, interface sliding and dislocation nucleation and movement were not possible. Spearot *et al.* [13] performed MD simulations on a copper bi-crystal interface under pure shear and pure tensile loading to extract information as input for a cohesive law. In [14] they showed the effect of the deformation path on the resulting microstructure for a nano-scale copper bi-crystal interface. They conclude that 'in order to incorporate path-history dependent effects into continuum interface separation potentials, additional parameters must be used to describe dissipative structural rearrangement within the deformation boundary layer'. Dandekar and Shin [15] parametrised, based on molecular dynamics simulations, a cohesive law for pure mode I and mode II decohesion for an Al-SiC interface. Yamakov *et al.* [16, 17] derived a cohesive zone law from molecular dynamics simulations for implementation in a cohesive zone finite element model for simulating fracture in nano-crystalline or ultra-fine grained aluminium. Gupta *et al.* [18] performed MD simulations on an Al(metal)-$Cu_{50}Zr_{50}$(metallic glass) interface under mode I and mode II loading conditions to predict the strength of the interface. Paliwal and Cherkaoui [19] developed for a specific symmetric tilt grain boundary in copper an atomistic simulation based cohesive zone law which accounts for the non-planarity of crack propagation.

Although many studies, as can already be seen in the short selection described above,

studied interface behaviour, only little information is available on interfaces in steel. In the present study we therefore examine the behaviour of iron-precipitate interfaces, as a model for the interfaces between the matrix and precipitates that can be encountered in advanced high strength steels. Most of the literature in which cohesive zone law parameters are determined from MD simulations focusses on one particular interface for a certain material (combination). In the present study we derive a cohesive law for 11 different iron-precipitate interfaces under pure shear loading, with and without dislocations interacting with the interface. We show that not just the material combination across the interface, but also the specific orientations of the crystals give a large variety in the response to a shear load. Furthermore, this response is shear direction dependent. Section 4.2 describes the material, the set-up of the simulations and the analysis methods. The tangential traction relations and the differences in sliding behaviour are described in Section 4.3.1 for simulations without initial dislocations. The role of the geometrical and structural characteristics of the interfaces is studied in Section 4.3.1. The influence of an initial dislocation is described in Section 4.3.2. In Section 4.4 cohesive laws are derived which quantitatively describe the relation between T_t and u_t for all interfaces. Finally, conclusions are given in Section 4.5.

4.2. METHOD

The response of 11 different iron-precipitate interfaces to a shear load is studied by classical molecular dynamics simulations. The response to a tensile load applied to the same interfaces was already reported in [2]. In the tensile case it was found that stress concentrations may develop which in turn lead to crack nucleation. Here, because of periodic boundaries of the simulation volume, crack nucleation is impossible.

4.2.1. MATERIAL DESCRIPTION

Iron is described with the EAM potential by Ackland *et al.* [20]. In the EAM format the potential energy of atom i is given by

$$U_i = F(\rho_i) + 1/2 \sum_j \phi_{ij}(r), \tag{4.1}$$

where F is the embedding energy of atom Fe or atom X as a function of the local electron density ρ_i, and ϕ_{ij} is the pair interaction between atom i and the surrounding atoms j as a function of their distance r. The local electron density ρ_i is made up from the contributions ψ_j to the electron density by the atoms j surrounding atom i at distances r,

$$\rho_i = \sum_j \psi_j(r). \tag{4.2}$$

F, ϕ and ψ are relatively simple functions, parametrised for Fe. They can be found in the original paper [20].

The artificial precipitate material X is chosen to be material X$^{(3)}$ from [21]. In this work we choose $\phi_{XX} = 2\phi_{FeFe}$, $a_X = 1.1a_{Fe}$, and the embedding term $F(\rho_i)$ is equal for

Fe and X atoms. To create material X with lattice constant $a_X = 1.1 a_{Fe}$, we use

$$\phi_{XX}(r) = \phi_{FeFe}(r/1.1),$$
$$\psi_X(r) = \psi_{Fe}(r/1.1).$$
(4.3)

X has thus a 10 % larger lattice constant than Fe and, as a result of the X – X pair interaction being twice as strong as that of Fe – Fe and the X- and Fe-embedding terms being equal, X has a 49 % larger Young's modulus than Fe. Material X is thus stiffer than Fe and, due to the different lattice constant, forms semi- or non-coherent interfaces with Fe. Dislocation transfer into the precipitate material is therefore hindered, just as it is in real precipitate materials found in steel, such as carbides and nitrides of different alloying elements. Similar to [21] the mixed Fe – X pair interaction is a linear combination of the individual Fe – Fe and X – X pair interactions,

$$\phi_{FeX} = q(\phi_{FeFe} + \phi_{XX}),$$
(4.4)

where the factor q in this study equals 1/3. This Fe–X pair interaction in combination with the orientations of the Fe and X grains on either side of the interface determines the interface strength. However, defects at the interface, initially present but also those developing during loading and grain sliding, may be of significant additional influence.

4.2.2. SETUP
The Fe – X system is schematically shown in Figure 4.1. The system size is dependent on the orientation of the crystals, and on average equals $165 \times 4.4 \times 110$ nm^3, with the number of atoms per system varying between 6 and 9 million. The system is periodic in x and y.
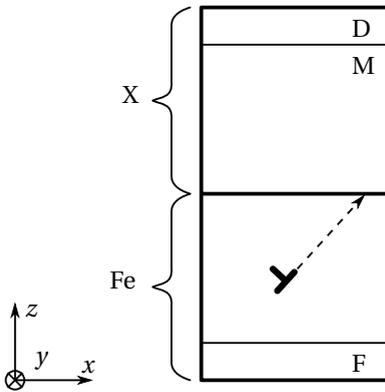
Figure 4.1: Setup of the simulations. The simulation box consists of an Fe – X bicrystal, which is periodic in x- and y-directions. The atoms in region F are kept fixed, atoms in region M are mobile atoms, whose positions are updated by time integration, and the atoms in region D are moved in the positive or negative x-direction with a constant strain rate of $\dot{\varepsilon} = 10^8$ s^{-1}. In the Fe grain one {112}⟨111⟩ edge dislocation can be inserted close to the interface, so that upon minimisation it moves towards the interface. The X grain is the precipitate material.

The orientations of the 11 different interfaces, being the same as the ones studied in [2], are listed in Table 4.1. Since in α-iron the typical cleavage plane is the (100) plane, with the crack front direction in either the [001] or the [011] direction, the most logical starting point for the study of interface decohesion, as is also the focus of [2], is a system with the (100) plane at the interface, which upon decohesion becomes the crack plane. To study the interaction of a dislocation with such an interface, the dislocation line has

to be in a periodic direction to avoid edge effects. In both [21] and [2] the choice was therefore made to study dislocations of the $\{112\}\langle 111\rangle$ slip system, so that the dislocation line is in the [011] direction, which, with the (100) plane at the interface, is the crack front direction. With this as starting point, the orientations of the iron and precipitate crystal are varied to obtain the orientations given in Table 4.1. In [2] it was shown that the relation between normal traction T_n and normal separation u_n during crack *growth* is independent of the number of dislocations in the iron grain impinging on the interface. These impinging dislocations cause a stress concentration at the interface, which helps triggering crack *nucleation*. Note that the time needed for crack nucleation does depend on the number of dislocations. In the present study no crack nucleation or decohesion will take place, since only a pure shear load is applied to the system, the system has periodic boundary conditions in the loading direction, and atomic z-displacements are not allowed in regions F and D. The simulations are performed both without dislocations and with one dislocation present in the iron grain at the interface. In this manner not only the pure shear behaviour but also the influence of a dislocation can be studied. The dislocation is initially placed in the iron grain at 10 Å underneath the interface by removing a half plane of atoms. Upon energy minimisation the dislocation moves to the interface where it halts. By starting the simulations with the dislocation at the interface, instead of far below the interface, the influence of the different angles between glide plane and loading direction for the different oriented Fe grains is minimised.

In the simulations, atoms in the lower 10 Å are kept fixed, region F in Figure 4.1. On atoms in the upper 10 Å, region D, a tangential displacement is imposed with a constant strain rate $\dot{\varepsilon}$ of 10^8 s^{-1}. For the mobile atoms, region M, time integration using a time step of 5 fs is performed at 1 K with a Nosé-Hoover thermostat. Prior to loading, the system is equilibrated at 1 K for 100 ps. The stress σ that results from the applied strain is calculated by summing the resulting forces on the atoms in region D and dividing this by the area in the x, y-plane.

The very low temperature of 1 K was chosen to be able to see details of the atomic behaviour driving the interface dynamics. At higher temperatures these details would be hidden by thermal vibrations.

The particular interface realisations for each of the 11 crystal orientations are taken from [2], where they were created using the method described by Tschopp and McDowell [22]. A systematic collection of interface structures was generated by energy minimisation following extremely small initial displacements in the x and y directions. Of all the possible interface structures thus generated, the structure of which the interface energy has the highest number of occurrences in the collection is chosen as the final realisation.

Table 4.1: Orientations of the Fe and X grains giving the 11 different interface structures. The angle between the dislocation glide direction and the interface is given as ζ in Fe and η in X. All interfaces have been given a label just to identify them. Interfaces with the same letter(s) have one grain in the same orientation.

		Fe			X			ζ (°)	η (°)
		x	y	z	x	y	z		
(100) Fe	S1	$[01\bar{1}]$	$[011]$	$[100]$	$[11\bar{1}]$	$[011]$	$[2\bar{1}1]$	35.3	0.00
	S2	$[01\bar{1}]$	$[011]$	$[100]$	$[01\bar{1}]$	$[011]$	$[100]$	35.3	35.3
	S3	$[01\bar{1}]$	$[011]$	$[100]$	$[\bar{2}3\bar{3}]$	$[011]$	$[31\bar{1}]$	35.3	60.5
	S4	$[01\bar{1}]$	$[011]$	$[100]$	$[21\bar{1}]$	$[011]$	$[1\bar{1}1]$	35.3	90.0
(100) X	Fe1	$[11\bar{1}]$	$[011]$	$[2\bar{1}1]$	$[01\bar{1}]$	$[011]$	$[100]$	0.00[a]	35.3
	Fe3	$[\bar{2}3\bar{3}]$	$[011]$	$[31\bar{1}]$	$[01\bar{1}]$	$[011]$	$[100]$	60.5	35.3
	Fe4	$[21\bar{1}]$	$[011]$	$[1\bar{1}1]$	$[01\bar{1}]$	$[011]$	$[100]$	90.0[b]	35.3
(110) Fe	X1	$[001]$	$[1\bar{1}0]$	$[110]$	$[111]$	$[1\bar{1}0]$	$[11\bar{2}]$	54.7	0.00
	X2	$[001]$	$[1\bar{1}0]$	$[110]$	$[113]$	$[1\bar{1}0]$	$[33\bar{2}]$	54.7	29.5
	X3	$[001]$	$[1\bar{1}0]$	$[110]$	$[001]$	$[1\bar{1}0]$	$[110]$	54.7	54.7
	X4	$[001]$	$[1\bar{1}0]$	$[110]$	$[\bar{1}\bar{1}2]$	$[1\bar{1}0]$	$[111]$	54.7	90.0

[a] The dislocation is placed in the $[1\bar{1}1]$ direction, giving an angle between slip plane and crack plane of 70.6°.

[b] The dislocation is placed in the $[\bar{1}\bar{1}1]$ direction, giving an angle between slip plane and crack plane of 19.4°.

4.2.3. LOCAL BEHAVIOUR

Similar to [2], to calculate the local response to the applied load in the interface region, the region is divided into multiple bins along the x-direction. Each bin is then divided in two: one half above the interface, one half underneath, as shown in Figure 4.2. The width of each bin, δx, was chosen to be 8.8 Å, or five atomic [100] planes. The height of the bins, δz, was chosen as 20 Å. This ensures that the total interface region, which is the region in which significant extra strain is seen with respect to the bulk, is taken into account in the calculations made over each bin [2].

For every bin k the stress is calculated as the average of the stresses on the N_k atoms j in the bin, according to

$$\sigma_{\alpha\beta k} = \frac{1}{N_k} \sum_{j=1}^{N_k} \sigma_{\alpha\beta k j}. \tag{4.5}$$

The tangential traction T_t is equal to the $\alpha\beta = xz$ component.

The tangential separations u_t between the bins above and underneath the interface is calculated at the time of interest t as the increase in tangential distance between the centers of mass (c) of these bins

$$u_t(t) = x_c^X(t) - x_c^{Fe}(t) - (x_c^X(0) - x_c^{Fe}(0)), \tag{4.6}$$

where x_c^{Fe} is the x-position of the center of mass of the Fe-bin, below the interface, and x_c^X is the x-position of the X-bin, above the interface. For simplicity of notation T_t and
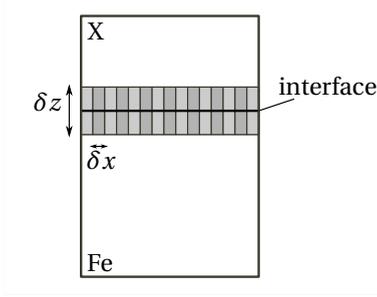
Figure 4.2: Division of interface region into bins with width δx of 8.8 Å and height δz of 20 Å. The bins have a role only in the data analysis, not in the simulation.

u_t do not carry a subscript designating the bin to which they apply. The values for T_t and u_t were calculated every 100 time steps (500 fs) as an average over 10 time steps (50 fs).

To determine T_n and u_n in [2], the allocation of atoms to bins was made every time step when these values were calculated. To determine T_t and u_t in this study, the allocation to bins is made once, at the beginning of the simulation. This difference is necessary since interface sliding occurs under shear loading. To determine the tangential displacement, the displacements with respect to the original positions need to be used.

In addition to the $T_t(u_t)$ results for individual bins, the data are also averaged over the entire interface and over time intervals of 10 ps. This averaging is done to smoothen the curves and get a better view on the similarities and differences between the different interfaces and loading directions. These average traction data are indicated as $\overline{T_t}(u_t)$. Also, in isolated cases, the standard deviation of these data points $S(T_t(u_t))$ is reported. This quantity reflects the homogeneity of the traction value along the interface.

4.2.4. METHODS
The MD-simulations are performed with LAMMPS [23, 24] and the GPU-accelerated version hereof [25–27]. The structures are visualised with OVITO [28]. As a measure for changes in the interface structure the number of non-bcc atoms at the interface is determined with the common neighbour analysis as implemented in LAMMPS [29, 30]. We found this to be a sensitive diagnostic for recording structural changes at an interface.

4.3. RESULTS
In the following we present the results of this work. Section 4.3.1 shows that without dislocations present the interfaces can be divided in three different categories: those that show equal behaviour under opposite shearing direction, Section 4.3.1, those that show a small difference in behaviour under opposite shearing directions, Section 4.3.1, and those that show a large difference in behaviour under opposite shearing directions, Section 4.3.1. Section 4.3.1 discusses the characteristics of the different interfaces and their relation, or the absence of a relation, with the behaviour of the interfaces under a shear load. With an initial dislocation present at the interface, the interfaces can be

divided in two categories : those where the dislocation does not influence the behaviour under a shear load, Section 4.3.2, and those where the dislocation changes the interface structure and with that the behaviour under a shear load, Sections 4.3.2 and 4.3.2. The influence of the dislocation slip plane and the loading direction is discussed in Section 4.3.2.

As a reference to the 11 different Fe – X bicrystal interfaces, of which the crystallographic data were given in Table 4.1, we show the initial atomic structures in Figure 4.3 and those after 500 ps shear loading in positive x-direction in Figure 4.4.
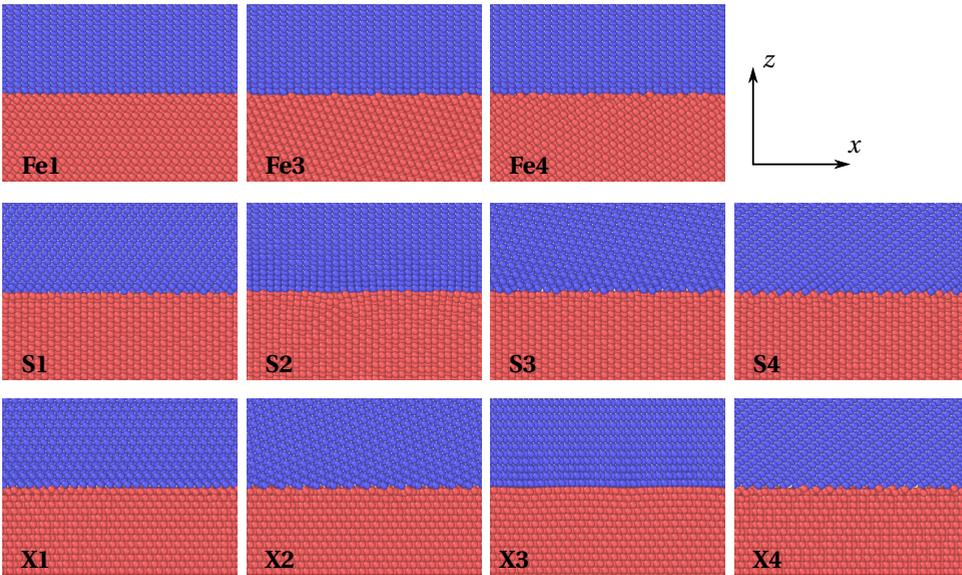
Figure 4.3: Atomic positions at the interfaces. Atoms in blue are X, atoms in red are Fe.

4.3.1. SHEAR LOADING WITHOUT DISLOCATIONS

For all interfaces and loading directions the upper crystal eventually slides over the lower crystal. Yet, the system responses vary. For some interfaces the tangential traction versus tangential separation ($T_t(u_t)$) for all bins follows a very similar periodic behaviour, as illustrated in Figure 4.5a for the X1 interface, where the traction behaviour is shown for five different bins, indicated by their initial x-positions x_0 (for clearer visibility the curves for the different bins have been shifted along the T_t-axis). For some other interfaces, however, first a barrier needs to be overcome in every bin before sliding starts, as is shown by a non-zero value (roughly 3 GPa) of the sliding resistance T_t^s. This is illustrated for five bins of the Fe4 interface in Figure 4.5b.

As can be seen in Figure 4.5a, for all the bins along the X1 interface the behaviour is similar. For the Fe4 interface the behaviour of the individual bins is dissimilar, more chaotic and not as clearly periodic as for the X1 interface (Figure 4.5b). It is therefore harder to notice common patterns in the different bins. However, the averages and the standard deviations over time of the tangential traction during sliding are equal for the
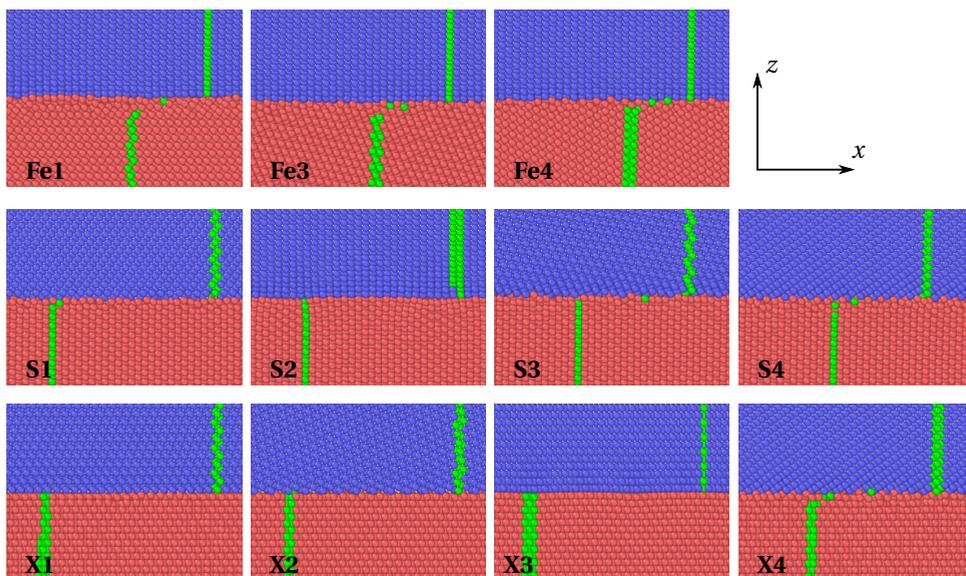
Figure 4.4: Atomic positions at the interfaces after 500 ps of shearing in the positive x-direction. Atoms in blue are X, atoms in red are Fe. Atoms marked in green formed one vertical plane before shearing.

(a) X1

(b) Fe4
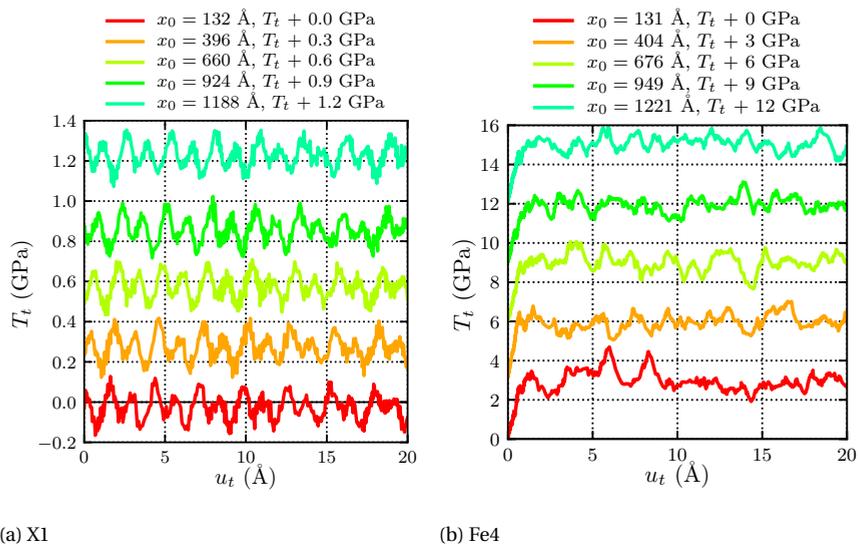
Figure 4.5: Two examples of different sliding behaviour at different interfaces. Tangential traction versus tangential separation for five bins along the X1 and Fe4 interfaces under shearing in the positive x-direction. For a clearer view on the behaviour of individual bins the curves have been shifted vertically. The initial bin positions are indicated by x_0. Note the difference in vertical scale for the two interfaces.

different bins, which does show a certain similarity between the bins. Therefore, for easy comparison, for every interface and loading direction the average $\overline{T_t}$ over the bins is determined. Also, the interface structures are analysed. As mentioned above, three different kinds of behaviour are seen for the 11 interfaces: 1. equal behaviour for shearing in opposite directions, 2. slightly different behaviour for shearing in opposite directions, 3. very different behaviour for shearing in opposite directions. We will next discuss these different types.

EQUAL BEHAVIOUR FOR SHEARING IN OPPOSITE DIRECTIONS

For the S2, X1 and X3 systems the average tangential tractions $\overline{T_t}(u_t)$ are equal for shearing in opposite directions, see Figures 4.6 and 4.7 (X1 is similar to X3). These interfaces all have a structure that is quite flat and is mirror symmetric along the $y-z$ plane, Figure 4.3. Therefore it is not surprising that the behaviour is the same in both shearing directions. Because of the flatness of the Fe and X surfaces at the interface, these Fe and X crystals clearly slide along the interface as rigid blocks, and not, as is seen for most of the other interfaces, following a gradual slip profile of the top Fe planes, Figure 4.4.

This can be further quantified by looking at the structure of the interface. As a measure for changes in the interface structure we record the number of non-bcc atoms per unit of interface area, n_{int}. This number hardly changes for S2 (Figure 4.7(bottom)), X1 and X3 (Figure 4.6(bottom)), and one can therefore conclude that the interface structure does not change, which again indicates that the sliding takes place as rigid crystal blocks along these interfaces. The sliding along the X3 interface, Figure 4.6(top), and along the X1 interface (not shown) takes place at near-zero resistance. For S2 a barrier in $\overline{T_t}(u_t)$ has to be overcome before the crystals start sliding, as shown by the non-zero steady-state resistance, Figure 4.7.
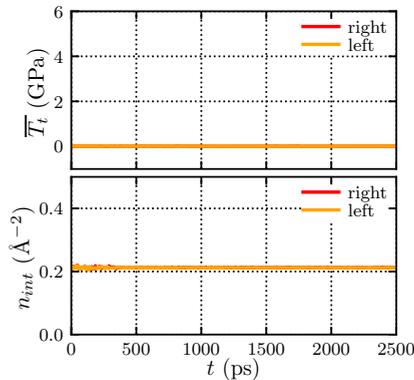
Figure 4.6: Time evolution of tangential traction averaged over all bins along the interface (top) and number of non-bcc atoms per unit interface area (bottom) for the X3 interface (see Figure 4.3) under shear loading in opposite directions. To smoothen the curves the data points are averaged over 10 ps.
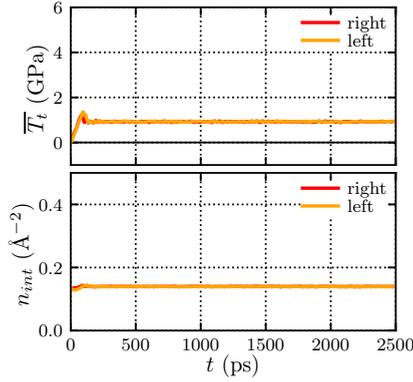
Figure 4.7: Time evolution of tangential traction averaged over all bins along the interface (top) and number of non-bcc atoms per unit interface area (bottom) for the S2 interface (see Figure 4.3) under shear loading in opposite directions. To smoothen the curves the data points are averaged over 10 ps.

SMALL DIFFERENCE BETWEEN SHEARING IN OPPOSITE DIRECTIONS

The Fe1, Fe3, Fe4, S1, S3, and S4 interfaces show small differences for shearing in opposite directions. This is caused by the initial interface structures, Figure 4.3, having deviations from mirror-symmetry. After 500 ps of shearing, Figure 4.4, all these interfaces show sliding of the X crystal with respect to the Fe crystal in another way than sliding as rigid blocks. The upper atomic Fe layers exhibit a gradual slip profile in the shearing direction, as can be seen by the displacement of the atoms marked in green.

During shearing and before sliding, the tangential traction increases and the number of non-bcc Fe and X atoms changes, as is illustrated in Figure 4.8 for the Fe4 interface. Once the upper crystal slides with respect to the lower crystal, the structure of the interface no longer changes, as is indicated by the constant n_{int}, and the tangential traction becomes constant: a steady-state sliding behaviour develops. We find a small difference between the responses to shearing in the two directions. The barrier which needs to be overcome to start sliding is higher when shearing to the left, which is reflected by a small peak in the tangential traction and a different change in interface structure compared to shearing to the right.

The Fe1, S1, S3, and S4 interfaces show a similar behaviour as the Fe4 interface, i.e. with only a small difference between shearing to the left or to the right. The Fe3 interface shows a slightly different behaviour, which is explained in Appendix 4.A.

LARGE DIFFERENCE FOR SHEARING IN OPPOSITE DIRECTIONS

For the X2 and X4 interfaces, due to their saw tooth structure as shown in Figure 4.3, there are large differences between shearing in opposite directions. In one direction sliding takes place almost without resistance, while in the other a barrier has to be overcome, and sliding occurs with a resistance of almost 2 GPa. Figure 4.9 illustrates this behaviour for the X2 interface. Shearing to the right leads to sliding at near zero friction, without a change in interface structure, as indicated by the constant number of non-bcc atoms. As can be seen in Figure 4.4, this sliding occurs as rigid blocks. When sheared to the left,
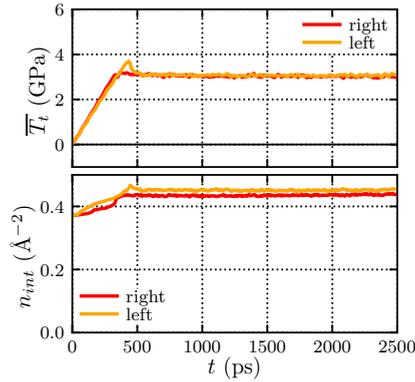
Figure 4.8: Time evolution of tangential traction averaged over all bins along the interface (top) and number of non-bcc atoms per unit interface area (bottom) for the Fe4 interface (see Figure 4.3) under shear loading in opposite directions. To smoothen the curves the data points are averaged over 10 ps.

a barrier has to be overcome and the structure slides at a tangential traction of almost 2 GPa while the interface structure changes. In this case, atoms in the upper Fe planes follow a gradual slip profile in the shearing direction. Conversely, the X4 crystals show the same behaviour but in opposite direction.
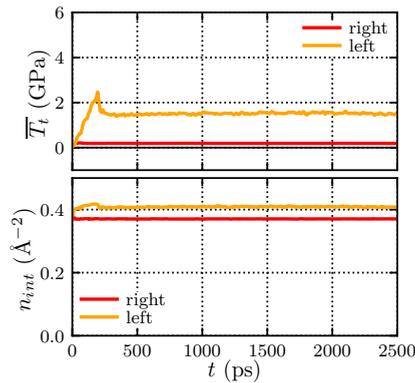
Figure 4.9: Time evolution of tangential traction averaged over all bins along the interface (top) and number of non-bcc atoms per unit interface area (bottom) for the X2 interface (see Figure 4.3) under shear loading in opposite directions. To smoothen the curves the data points are averaged over 10 ps.

INTERFACE CHARACTERISTICS

To understand the different sliding behaviours of the different interfaces, we need to study the interfaces in more detail. They can be characterised by the orientations of the crystals on either side, but this alone does not specify the interface completely, as the precise geometrical structure and the energy play additional roles. In this section we

will therefore describe first the energy of the interface and its relation with the sliding behaviour and then the geometrical structure and its relation with sliding.

As explained in Section 4.2.2, for every orientation the particular interface realisation studied has a structure of which the energy has the highest number of occurrences among all realisations studied. Only for the S2, X1 and X3 systems this energy is equal to the minimum interface energy for these particular orientations, and only these three systems slide as rigid blocks in both shearing directions. A possible reason for this is that during sliding, systems for which the minimum interface energy is the most occurring interface energy can move from one lowest-energy configuration to the next, whereas this is not possible for the other systems. The value of the interface energy itself shows no relation with the resistance of the interface to sliding. We find that for systems with one common crystal orientation, however, a lower interface energy does give a higher resistance to sliding and therefore a higher T_t^s.

The geometrical structure of the interface can be described in terms of the atomic density, the number of non-bcc atoms, the minimum distance between Fe and X atoms at the interface, and the degree of intermixing of Fe and X at the interface. No relation is found between the atomic density at the interface and T_t^s. A general relation (valid for all interfaces) between any of the other three terms and the sliding resistance is not found either. However, for systems with one common crystal orientation, certain correlations are found. For these systems (1) a higher number of non-bcc Fe atoms at the interface gives a higher T_t^s. The number of non-bcc X atoms does not play a role in determining the sliding resistance, since X is stiffer than Fe and therefore only Fe, and not X, atoms follow a gradual slip profile in the shearing direction. The number of non-bcc X atoms is therefore not a factor determining the sliding resistance. (2) A smaller distance between Fe and X atoms at the interface gives a higher sliding resistance, as does (3) an increased level of intermixing at the interface.

4.3.2. SHEAR LOADING WITH DISLOCATION
With one dislocation initially present in the iron grain at the interface the systems are again subjected to shear loads in opposite directions to investigate how the dislocation influences the behaviour of the interfaces. Three different kinds of influence are observed: 1. No influence, 2. A large influence under both shearing directions, 3. An influence for shearing in one direction only.

NO INFLUENCE OF DISLOCATION
The overall interface behaviour without a dislocation is not changed by the presence of a dislocation for the Fe1, Fe3, Fe4, S1, S3, S4, and X4 interfaces. The initial stress profile along the interface is locally influenced by the presence of a dislocation, as illustrated in Figure 4.10 for the Fe4 interface and in Figure 4.11 for the X4 interface. After 2500 ps of shearing we find two different types of behaviour. Either the dislocation can no longer be distinguished in the stress profile because it has dissolved in the interface, and the interface behaviour is not modified (Figure 4.10), or the dislocation can still be clearly distinguished, since the stress profile is only locally modified, just as it was initially. The behaviour along the rest of the interface, however, is not modified, as illustrated in Figure 4.11.
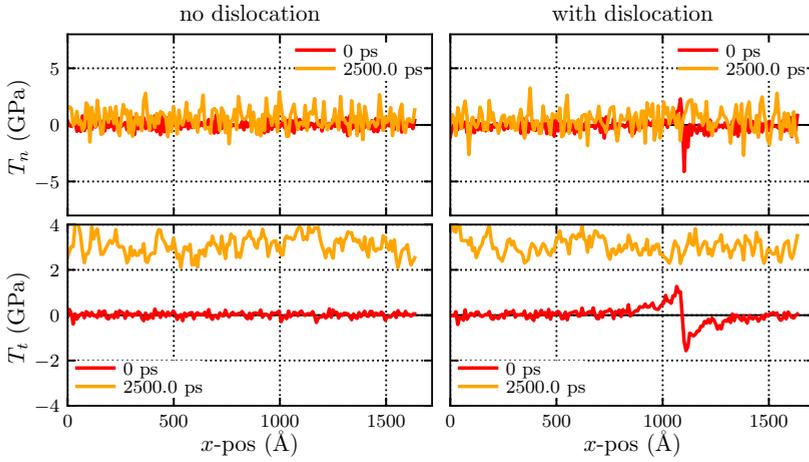
Figure 4.10: Initial and final (after 2500 ps shear in the negative x-direction) normal and tangential traction profiles along the Fe4 interface with and without an initial dislocation.
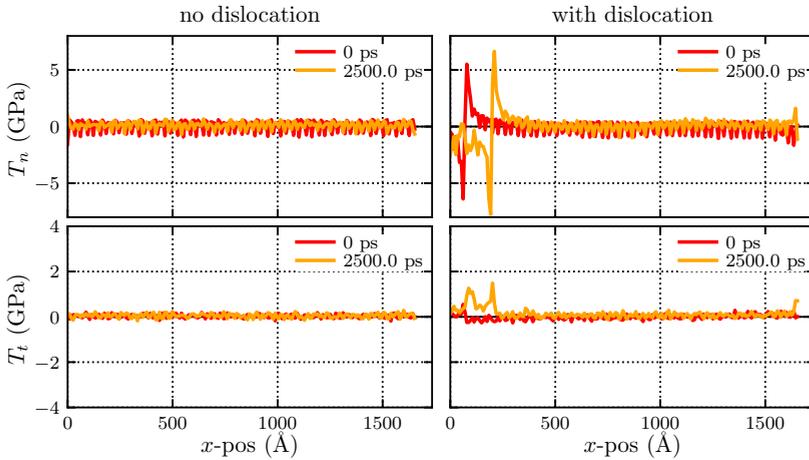
Figure 4.11: Initial and final (after 2500 ps shear in the negative x-direction) normal and tangential traction profiles along the X4 interface with and without an initial dislocation.

LARGE INFLUENCE OF DISLOCATION IN BOTH DIRECTIONS

As can be seen when comparing Figures 4.7 and 4.12, an initial dislocation at the S2 interface has a large but unequal influence on the shearing behaviour in both directions. Initially this interface has a regular structure of misfit dislocations, in which the initial dislocation in the iron crystal can be clearly distinguished (Figure 4.13, top). When a shear load in positive x-direction is applied to the system, the interface structure starts to change from this dislocation onward in both directions along the interface. After 900 ps of shear loading, the structure change has reached bin 60 (about 300 Å to the right of the initial dislocation position), as shown in Figure 4.13, bottom. This change in structure is accompanied by a change in the tangential traction, as can be seen in Figure 4.14, where the tangential traction is shown versus time at different positions along the interface. Since in Figure 4.12 averages over the interface are shown, the graphs in this figure show a gradual increase. Although the S2 interface is symmetric along the z-axis, the dislocation placed in the iron crystal has a slip plane at an angle with this axis, and therefore the symmetry is broken and the structure change, and with that the observed traction, is different under different loading directions.
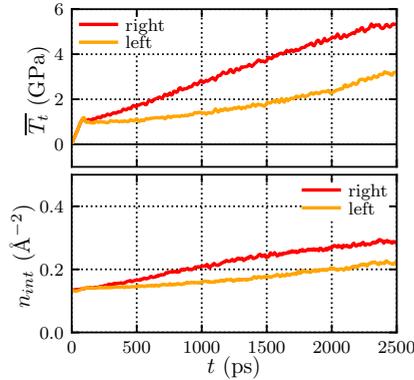
Figure 4.12: Time evolution of tangential traction averaged over all bins along the interface (top) and number of non-bcc atoms per unit interface area (bottom) for the S2 interface (see Figure 4.3) with one initial dislocation in the Fe crystal, under shear loading in opposite directions. To smoothen the curves the data points are averaged over 10 ps.

INFLUENCE OF DISLOCATION IN ONE DIRECTION ONLY

The behaviour of the X1, X2, and X3 interfaces only changes by an initial dislocation when sheared to the right. Without a dislocation shearing to the right leads to interface sliding at a near-zero tangential traction and without a change of interface structure, as illustrated in Figure 4.6 for the X3 interface. With a dislocation, as illustrated in Figure 4.15, the structure still starts sliding at a very low traction, but once the structure slides the mean tangential traction and the size of its oscillations gradually increase and the number of non-bcc atoms at the interface changes. Similar as for the S2 interface a gradual structure change along the interface from the dislocation position on explains this behaviour.
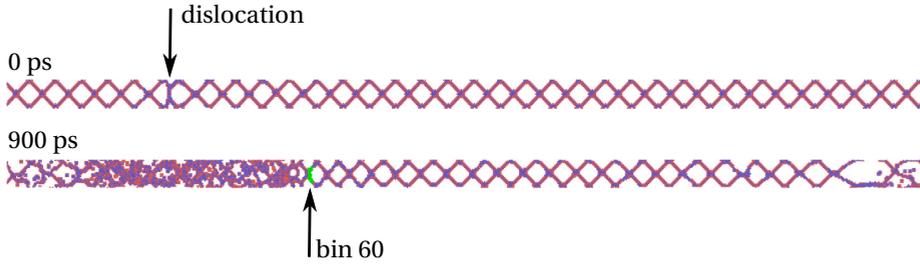
Figure 4.13: Top view of the non-bcc atoms in the S2-interface before (top) and after 900 ps of tangential loading (bottom). In the top figure the dislocation can be clearly distinguished in the interface. In the bottom figure, after 900 ps, the atoms in bin 60 are marked in green, and the interface structure to the left of this bin has undergone a change, which is accompanied by an increase in tangential traction (shown in Figure 4.14).
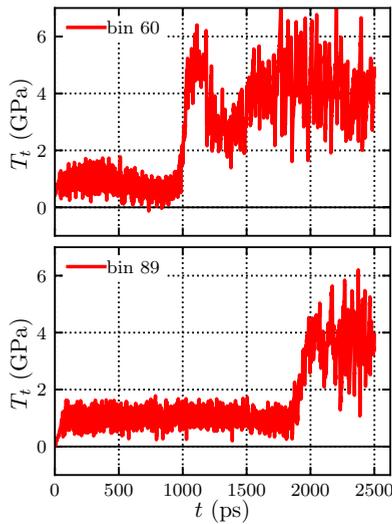
Figure 4.14: Tangential traction versus time at two different positions (bins) along the S2-interface under shear loading.
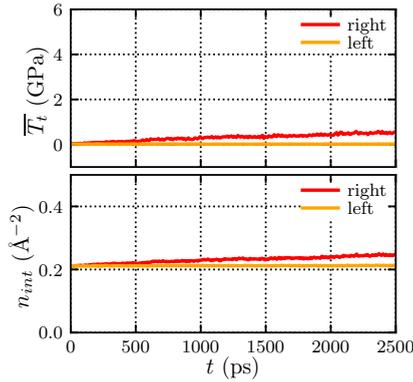
Figure 4.15: Time evolution of tangential traction averaged over all bins along the interface (top) and number of non-bcc atoms per unit interface area (bottom) for the X3 interface (see Figure 4.3) with one initial dislocation in the Fe crystal, under shear loading in opposite directions. To smoothen the curves the data points are averaged over 10 ps.

INFLUENCE OF SLIP PLANE AND LOADING DIRECTION

From the previous sections we can conclude that a dislocation only influences the response during shearing when the crystals, without a dislocation, slide as rigid blocks, so without a structure change at the interface. Only when the dislocation triggers a structure change, the response of the system is modified. This can depend on the loading direction, and therefore on the resolved shear stress on the dislocation, as seen for the X1 and X3 interface for which the shear behaviour is modified by the presence of a dislocation only when sheared in the positive x-direction.

When the crystals slide along the interfaces by an atomic slip profile of the upper Fe planes with some changes in the interface structure, the interface can accommodate the dislocation, either by letting it dissolve in the interface or leaving it in the interface unmodified, and its presence does not influence the response along the interface outside the region where the dislocation is accommodated.

As shown in the previous sections a structure change of the interface leads to a different interface behaviour. The loading direction, the interface, and the dislocation all determine the structure change. A different structure change leads to a different interface behaviour.

4.4. COHESIVE LAW

Subjecting the 11 different interfaces to a shear load shows that the relation between tangential traction T_t and tangential separation u_t is not only interface dependent. It also depends on the shearing direction. Furthermore, the relation can be modified by impinging dislocations. A cohesive law giving the relation between tangential traction and separation should therefore capture all these effects.

We find from the simulation results that, without dislocations present, the relation between T_t and u_t can be described in three parts (Figure 4.16): an elastic part for sep-

arations smaller than the critical separation u_t^{crit}, a steady-state sliding part for separations larger than u_t^s and a quadratic part in between, where the steady-state sliding behaviour develops:

$$
\begin{aligned}
T_t &= \frac{T_t^{crit}}{u_t^{crit}} u_t, & \text{for } 0 \le u_t \le u_t^{crit}, \\
T_t &= \frac{T_t^{crit} - T_t^s}{(u_t^s - u_t^{crit})^2}(u_t - u_t^s)^2 + T_t^s, & \text{for } u_t^{crit} \le u_t \le u_t^s, \\
T_t &= T_t^s, & \text{for } u_t \ge u_t^s.
\end{aligned}
\tag{4.7}
$$

Here u_t^{crit} is the separation at which the structure starts to slide, T_t^{crit} is the corresponding value of the traction, u_t^s is the separation at which steady-state sliding behaviour is reached, and T_t^s is the corresponding sliding traction. For shearing in the negative x-direction the same relation is found, with negative values for the tractions and separations. Figure 4.17 shows the obtained results for three of the interfaces. In Table 4.2 in Appendix 4.B the parameters for the cohesive law are given for all the interfaces and for both shearing directions. This is one of the principal results of this work.
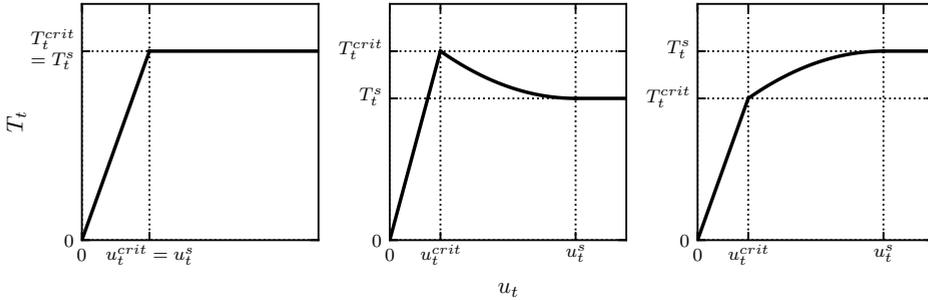
Figure 4.16: Three possible shapes of the cohesive law (Equation 4.7) describing the relation between T_t and u_t.

With dislocations present, as was shown in Section 4.3.2, it is found that for several interfaces the structure of the interface changes upon sliding, which results in a changed relation between traction and separation. When this happens, the structure changes gradually outward from the dislocation position, not unlike the fronts of a phase transition. During shearing there will be a part of the interface which still has the original structure A_{orig} and a part which has a new structure A_{new}. The fraction ξ of changed interface area can be used as a running parameter representing the progress of the "phase transition",

$$
\xi = \frac{A_{new}}{A_{orig} + A_{new}}.
\tag{4.8}
$$

In our current model it is assumed that for the unchanged part of the interface the original cohesive law T_t derived without a dislocation is still valid. For the changed part of
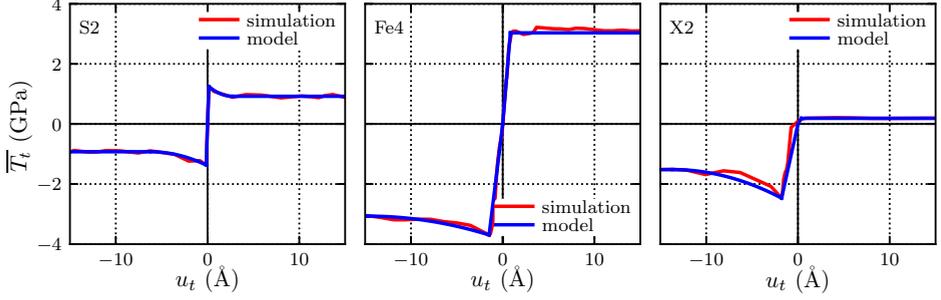
Figure 4.17: T_t versus u_t for three interfaces as obtained from the simulations and as expressed by the fitted cohesive law, Equation 4.7, with the parameters given in Table 4.2

4

the interface a different relation between T_t and u_t exists, T_t^{new}. The overall cohesive law for the changing interface is then given by

$$T_t = (1 - \xi) T_t^{orig} + \xi T_t^{new}, \tag{4.9}$$

where T_t^{orig} is now used for the original cohesive law T_t of Equation 4.7. For those interfaces where the structure changes by the presence of a dislocation, the boundaries between the changed and unchanged parts of the interface are determined by analysing the number of non-bcc Fe and X atoms in every bin along the interface, since this number changes when the structure changes. The time dependence then yields the rate of structure change $\dot{A}_{new}$. Upon sliding, the initial positions of the dislocation in the upper and lower crystal move apart, as is schematically illustrated in Figure 4.18. When initially the structure of both the Fe and the X crystal is locally modified at the initial position of the dislocation, one can imagine that when these two locally modified parts move apart, the structure of the region in between will also change. As is shown in Figure 4.18, the part of the interface with the new structure, A_{new}, would be then the part in between the initial dislocation positions in Fe and X and the rest of the interface, A_{orig}, would stil have the original structure. $\dot{A}_{new}$ would then be equal to the sliding velocity, which is determined by $\dot{\varepsilon}$.

However, the rate of structure change $\dot{A}_{new}$ is always larger than the sliding velocity, which is 110 Å/ns for $\dot{\varepsilon} = 10^8 \text{s}^{-1}$. This is shown in Figure 4.19, where for the different interfaces $\dot{A}_{new}$ is shown versus different applied strain rates. From Figure 4.19 it can be concluded that the changed part of the interface is not confined to the region between the dislocation fragments in Fe and X. The structure change extends outside this region in the negative x-direction for the X1, X2, and X3 interface and in both positive and negative x-directions for the S2 interface. The rate of structure change shows a linear dependence on the strain rate, as indicated by the dashed curves in Figure 4.19 which are linear fits to the data. $\dot{A}_{new}$, however, is always larger than the sliding velocity and the dependence on the strain rate is interface and shear direction dependent.

With the change rate as given in Figure 4.19 the overall tangential traction of the interface can be calculated with Equation 4.9 and compared with the actual obtained trac-
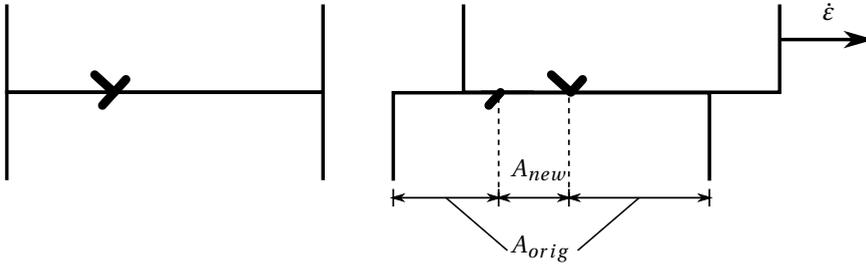
Figure 4.18: Schematic representation of structure change at the interface caused by sliding of the crystals. Once the upper crystal slides with respect to the lower crystal, the locations in the upper and lower crystal which were affected by the initial dislocation move apart, as is schematically illustrated by the two parts of the dislocation symbol. A_{new} and A_{orig} are the areas of the changed and original interface structures, $\dot{\varepsilon}$ determines the sliding velocity (110 Å/ns).
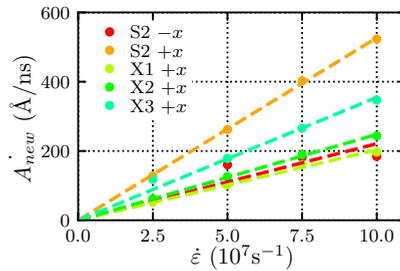
Figure 4.19: Rate of structure change versus applied strain rate for different interfaces. For all interfaces and strain rates the rate of structure change is larger than the sliding velocity. The dashed lines are linear fits to the data.

tion in the simulations as given in Section 4.3.2. This is illustrated for the S2 interface in Figure 4.20. As can be seen in Figure 4.20a, the cohesive law as given in Equation 4.9 is able to capture the increase in T_t caused by the changing interface structure. From Figure 4.20b it becomes clear, however, that for large separation T_t increases more than the cohesive law predicts. This is caused by the (artificial) periodicity of the simulation box. When the structure in a large part of the interface has changed, the stress in that part has increased. The unchanged part of the interface then feels the stress field from the changed region from both sides, due to the periodicity, leading to an increase in T_t in the unchanged part of the interface and therefore to an increase in the total T_t averaged over the interface.

In this study the focus is only on the interface behaviour during loading. If no structure change would occur at the interface, the unloading behaviour is expected to simply follow the cohesive law for the opposite shearing direction. However, as we have seen that the structure of the interface changes during loading, one cannot predict the behaviour during unloading with the current cohesive law and the parameters in Table 4.2. Further study is necessary to capture the unloading behaviour in a cohesive law.

Only for interfaces which slide as rigid blocks without a dislocation, an influence of the dislocation on the shearing behaviour is seen. In this study only the influence of one dislocation of the $\{112\}\langle111\rangle$ slip system per interface is studied. Since the dislocation interacts with the interface under an angle, it can be expected that a different structure change would result for a dislocation of the same slip system but on a slip plane under a different angle with the interface, and therefore the interface behaviour would be different. Similarly, a dislocation of another slip system may cause a different structure change at the interface and therefore have a different influence on the shearing behaviour. With the current set-up of the simulations, it is not possible to study the effect of dislocations of the $\{110\}\langle111\rangle$ slip system on the interface behaviour for the interfaces in this study.

With the cohesive law derived in this section the traction-separation relations of different interfaces under a shear load can be implemented in larger-scale simulations.

(a)   (b)
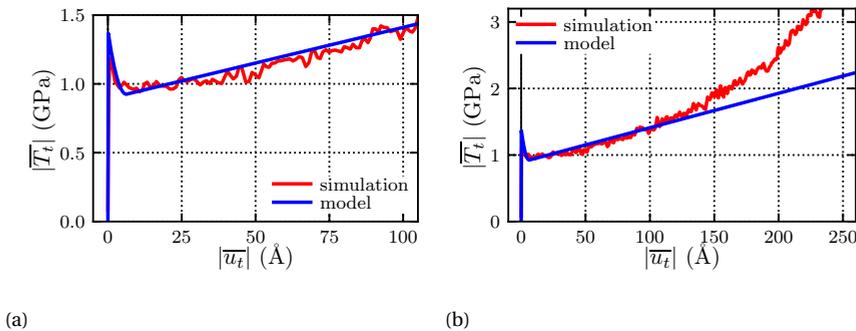
Figure 4.20: T_t versus u_t for the S2 interface under shearing in the negative x-direction, as obtained from the simulations and as expressed by the fitted cohesive law, Equation 4.9. Note that panel (a) is an enlargement of panel (b).

4.5. CONCLUSIONS

From the response to a shear load of Fe – X bicrystals with 11 different interfaces we conclude that the interfaces can be divided into three different categories:

1. Interfaces along which the crystals slide as rigid blocks, with an equal behaviour of $T_t(u_t)$ for shearing in opposite directions, Section 4.3.1. These interfaces are found to be all those for which the energy of the most occurring realisation is also the minimum energy for the given crystal orientation relation. These are the interfaces S2, X1, and X3.

2. Interfaces along which the crystals slide following a gradual slip profile of the atoms in the upper atomic Fe planes, Section 4.3.1. These interfaces show a somewhat different behaviour of $T_t(u_t)$ for shearing in opposite directions. These are the interfaces Fe1, Fe3, Fe4, S1, S3, and S4.

3. Interfaces with mixed behaviour, i.e. with crystals sliding as rigid blocks in one direction and following a gradual slip profile of atoms in the upper Fe planes in the opposite direction, Section 4.3.1. These interfaces show a significantly different behaviour of $T_t(u_t)$ for the two opposite directions. These are the interfaces X2 and X4.

Considering only the interfaces from categories 2 and 3, and comparing only interfaces with one common crystal orientation, we conclude that, Section 4.3.1,

4. A lower interface energy leads to sliding at a higher tangential resistance.

5. The local atomic density at the interface does not determine the value of the sliding resistance.

6. A higher number of non-bcc Fe atoms at the interface leads to a higher sliding resistance.

7. There is no correlation between the number of non-bcc X atoms at the interface and the sliding resistance.

8. A stronger intermixing of Fe and X atoms across the interface, i.e. rougher surfaces at the interface, leads to a higher sliding resistance.

The influence of an initial dislocation in the Fe crystal just below the interface depends on the interface type:

9. For interfaces that slide following a gradual slip profile of the atoms in the upper atomic Fe planes two types of behaviour are observed, Section 4.3.2:

    • the dislocation completely dissolves in the interface and the overall response to a shear load is not modified,

    • the dislocation stays intact and the overall response to a shear load is not modified.

10. For interfaces that slide as rigid blocks two different types of behaviour are found:

- the dislocation moves into the interface, triggers a structure change of the interface which makes it no longer possible for the crystals to slide as rigid blocks, and the overall response of the interface is significantly modified, Sections 4.3.2 and 4.3.2,

- due to the sliding of the crystals the resolved shear stress does not increase enough for the dislocation to move into the interface, and the response of the interface is not modified, Section 4.3.2.

We derived a cohesive law to describe the relation between tangential traction and tangential separation at an interface during shearing.

11. The shear behaviour is described in three parts: an elastic part, a steady-state sliding part and a part in between, where the steady-state sliding behaviour develops.

12. This cohesive law is described by four parameters for every interface and for every loading direction.

13. The influence of a structure change of the interface triggered by the presence of a dislocation can be taken into account into this cohesive law by making it a linear combination of the original relation and the relation found for the changed structure, depending on the fraction of changed interface area. The rate of structure change is dependent on the interface, the shear direction and the strain rate.

APPENDIX
4.A. Behaviour of Fe3 interface under a shear load

As described in Section 4.3.1 the Fe3 interface shows a small difference for shearing in opposite directions. Apart from what was described in Section 4.3.1 there is another reason for this difference. When sheared to the right, as shown in Figure 4.21(top), the Fe3 interface shows a decrease in average tangential traction. Shearing in both directions leads to a change in interface structure, with only a small difference in the number of non-bcc atoms Figure 4.21(bottom). The resulting structures, however, are different, as shown in Figure 4.22(top). When sheared to the right a wavy interface structure develops, while when sheared to the left the surfaces become rough. These different structures result in different atomic stresses along the interface, as can be clearly seen in Figure 4.22(bottom), where stress concentrations corresponding to the wavy structure are shown. Since the different bins along the interface move through these stress concentrations at different moments in time, the standard deviation of the traction increases when the system is sheared to the right, Figure 4.21(middle). The average tangential traction, as shown in Figure 4.21(top), shows only a small deviation from the tangential traction that results when sheared to the left.
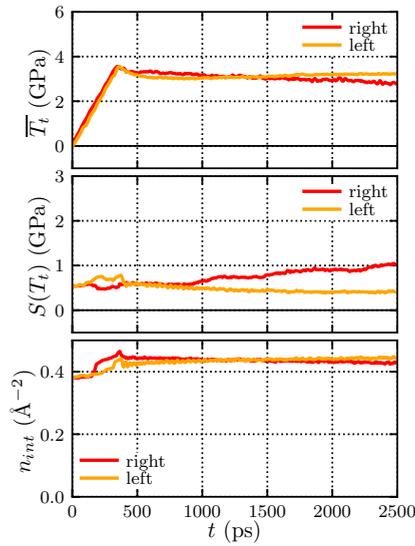
Figure 4.21: Time evolution of the average (top) and standard deviation (middle) of the tangential traction in all bins and the number of non-bcc atoms per unit interface area (bottom) for the Fe3 interface (see Figure 4.3) under shear loading in opposite directions. To smoothen the curves the data points are averaged over 10 ps.
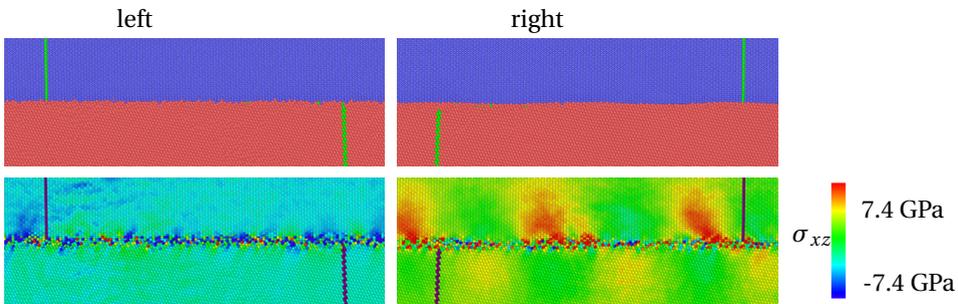
Figure 4.22: Positions of Fe and X atoms (top) and stresses σ_{xz} (bottom) at the Fe3 interface after 2500 ps of shearing in the positive (right) and negative (left) x-directions. In the top panels atoms in blue are X, atoms in red are Fe. Atoms marked in green formed one vertical plane before shearing. In the lower panels this plane is marked in purple, and the other atoms are coloured according to σ_{xz}.

4.B. PARAMETERS

Table 4.2: Parameters for the cohesive law as given in Equation 4.7 describing the relation between T_t and u_t for all the studied interfaces. Values for u_t^{crit} and u_t^s are in Å, values for T_t^{crit} and T_t^s are in GPa.

Interface	positive x-direction				negative x-direction			
	u_t^{crit}	u_t^s	T_t^{crit}	T_t^s	u_t^{crit}	u_t^s	T_t^{crit}	T_t^s
Fe1	8.08	143.35	2.92	1.95	-3.75	-84.09	-2.64	-1.95
Fe3	2.36	132.67	3.56	2.99	-4.00	-20.91	-3.56	-3.15
Fe4	0.83	0.83	3.03	3.03	-1.49	-14.74	-3.70	-3.07
S1	0.69	82.26	0.86	0.34	-0.29	-0.29	-0.41	-0.41
S2	0.15	2.72	1.24	0.92	-0.14	-6.24	-1.37	-0.92
S3	3.72	5.16	2.71	2.47	-2.04	-28.92	-1.94	-2.80
S4	1.92	6.64	3.08	2.96	-1.58	-11.09	-3.57	-3.10
X1	0.14	0.14	0.02	0.02	-0.12	-0.12	-0.03	-0.03
X2	0.38	0.38	0.19	0.19	-1.78	-13.69	-2.47	-1.52
X3	0.00	0.00	0.01	0.01	0.00	0.00	-0.01	-0.01
X4	2.19	8.17	0.96	1.67	0.00	0.00	-0.06	-0.06

REFERENCES

[1] A. Elzas, T. P. C. Klaver, and B. J. Thijsse, *Cohesive laws for shearing of iron / precipitate interfaces,* Computational Materials Science **152**, 417 (2018).

[2] A. Elzas and B. J. Thijsse, *Cohesive law describing crack growth at iron/precipitate interfaces,* Computational Materials Science **134**, 214 (2017).

[3] G. I. Barenblatt, *The Mathematical Theory of Equilibrium Cracks in Brittle Fracture,* Advances in Applied Mechanics **7**, 55 (1962).

[4] D. Dugdale, *Yielding of steel sheets containing slits,* Journal of the Mechanics and Physics of Solids **8**, 100 (1960), arXiv:0021-8928(59)90157-1 [10.1016] .

[5] X. P. Xu and A. Needleman, *Void nucleation by inclusion debonding in a crystal matrix,* Modelling and Simulation in Materials Science and Engineering **1**, 111 (1993).

[6] M. J. van den Bosch, P. J. G. Schreurs, and M. G. D. Geers, *An improved description of the exponential Xu and Needleman cohesive zone law for mixed-mode decohesion,* Engineering Fracture Mechanics **73**, 1220 (2006).

[7] J. Dollhofer, W. Beckert, B. Lauke, and K. Schneider, *Fracture mechanical characterisation of mixed-mode toughness of thermoplast/glass interfaces,* Computational Materials Science **19**, 223 (2000).

[8] K. Park, G. H. Paulino, and J. R. Roesler, *A unified potential-based cohesive model of mixed-mode fracture,* Journal of the Mechanics and Physics of Solids **57**, 891 (2009).

[9] J. P. McGarry, É. Ó. Máirtín, G. Parry, and G. E. Beltz, *Potential-based and non-potential-based cohesive zone formulations under mixed-mode separation and over-closure. Part I: Theoretical analysis,* Journal of the Mechanics and Physics of Solids **63**, 336 (2014).

[10] R. Dimitri, M. Trullo, L. De Lorenzis, and G. Zavarise, *Coupled cohesive zone models for mixed-mode fracture: A comparative study,* Engineering Fracture Mechanics **148**, 145 (2015).

[11] X. W. Zhou, J. A. Zimmerman, E. D. Reedy Jr., and N. R. Moody, *Molecular dynamics simulation based cohesive surface representation of mixed mode fracture,* Mechanics of Materials **40**, 832 (2008).

[12] X. W. Zhou, N. R. Moody, R. E. Jones, J. A. Zimmerman, and E. D. Reedy Jr., *Molecular-dynamics-based cohesive zone law for brittle interfacial fracture under mixed loading conditions: Effects of elastic constant mismatch,* Acta Materialia (2009), 10.1016/j.actamat.2009.06.023.

[13] D. E. Spearot, K. I. Jacob, and D. L. McDowell, *Non-local separation constitutive laws for interfaces and their relation to nanoscale simulations,* Mechanics of Materials **36**, 825 (2004).

4

[14] D. E. Spearot, K. I. Jacob, D. L. McDowell, and S. J. Plimpton, *Effect of deformation path sequence on the behavior of nanoscale copper bicrystal interfaces,* Journal of Engineering Materials and Technology **127**, 374 (2004).

[15] C. R. Dandekar and Y. C. Shin, *Molecular dynamics based cohesive zone law for describing Al-SiC interface mechanics,* Composites Part A: Applied Science and Manufacturing **42**, 355 (2011).

[16] V. Yamakov, E. Saether, D. R. Phillips, and E. H. Glaessgen, *Molecular-dynamics simulation-based cohesive zone representation of intergranular fracture processes in aluminum,* Journal of the Mechanics and Physics of Solids **54**, 1899 (2006).

[17] V. Yamakov, E. Saether, and E. H. Glaessgen, *Multiscale modeling of intergranular fracture in aluminum: Constitutive relation for interface debonding,* Journal of Materials Science **43**, 7488 (2008).

[18] P. Gupta, S. Pal, and N. Yedla, *Molecular dynamics based cohesive zone modeling of Al (metal)-Cu50Zr50 (metallic glass) interfacial mechanical behavior and investigation of dissipative mechanisms,* Materials and Design **105**, 41 (2016).

[19] B. Paliwal and M. Cherkaoui, *An improved atomistic simulation based mixed-mode cohesive zone law considering non-planar crack growth,* International Journal of Solids and Structures **50**, 3346 (2013).

[20] G. J. Ackland, M. I. Mendelev, D. J. Srolovitz, S. Han, and A. V. Barashev, *Development of an interatomic potential for phosphorus impurities in α-iron,* Journal of Physics: Condensed Matter **16**, S2629 (2004).

[21] A. Elzas and B. J. Thijsse, *Dislocation impacts on iron/precipitate interfaces under shear loading,* Modelling and Simulation in Materials Science and Engineering **24**, 85006 (2016).

[22] M. A. Tschopp and D. L. McDowell, *Structures and energies of $\Sigma 3$ asymmetric tilt grain boundaries in copper and aluminium,* Philosophical Magazine **87**, 3147 (2007).

[23] *LAMMPS Molecular Dynamics Simulator,* http://lammps.sandia.gov.

[24] S. J. Plimpton, *Fast Parallel Algorithms for Short-Range Molecular Dynamics,* Journal of Computational Physics **117**, 1 (1995).

[25] W. M. Brown, P. Wang, S. J. Plimpton, and A. N. Tharrington, *Implementing Molecular Dynamics on Hybrid High Performance Computers - Short Range Forces,* Computer Physics Communications **182**, 898 (2011).

[26] W. M. Brown, A. Kohlmeyer, S. J. Plimpton, and A. N. Tharrington, *Implementing Molecular Dynamics on Hybrid High Performance Computers - Particle-Particle Particle-Mesh,* Computer Physics Communications **183**, 449 (2012).

[27] W. M. Brown and Y. Masako, *Implementing molecular dynamics on hybrid high performance computers – Three-body potentials,* Computer Physics Communications **184**, 2785 (2013).

[28] A. Stukowski, *Visualization and analysis of atomistic simulation data with OVITO–the Open Visualization Tool,* Modelling Simul. Mater. Sci. Eng. **18**, 015012 (2009).

[29] D. Faken and H. Jónsson, *Systematic analysis of local atomic structure combined with 3D computer graphics,* Computational Materials Science **2**, 279 (1994).

[30] H. Tsuzuki, P. S. Branicio, and J. P. Rino, *Structural characterization of deformed crystals by analysis of common atomic neighborhood,* Computer Physics Communications **177**, 518 (2007).

4

5

COHESIVE LAWS DESCRIBING THE INTERFACE BEHAVIOUR OF IRON/PRECIPITATE INTERFACES UNDER MIXED LOADING CONDITIONS

The behaviour of 11 differently oriented iron-precipitate interfaces under mixed loading conditions is studied with molecular dynamics simulations. We find that the interface structure and the change in this structure play a key role in the response to the loading. The structure change is influenced by both the loading history and the loading direction. Depending on the interface and the loading direction, the presence of a dislocation at the interface may have an additional influence on the structure change. We update our previously derived cohesive laws for pure shear and pure tensile loading to take into account the influence of the other loading direction on the behaviour during mixed loading conditions. However, not for every interface a unique relation exists between the separations at the interface and the tractions. In those cases our cohesive laws give no exact prediction, but rather a range of possible values. The cohesive laws are intended to be used in numerical methods at the next larger length scale, such as discrete dislocation plasticity.

5.1. INTRODUCTION

In everyday use, interfaces in metallic microstructures are routinely subjected to stresses. Deformation and in certain cases mechanical failure are sometimes the ultimate results. Dislocations play an important role in this, but the stress response at interfaces between grains is equally important. Advanced high strength steels show limited ductility due to interface decohesion. To correctly model the material behaviour, so that the limited ductility can be explained, it is crucial to understand the interface behaviour under different loading conditions.

In this paper we describe the interface behaviour of iron-precipitate interfaces under mixed loading, elaborating on our previous studies of normal and shear loading. Not only is the interface behaviour described in detail, also cohesive laws are derived describing the behaviour under various forms of mixed loading. These cohesive laws can be used in numerical methods at the next larger length scale beyond atomic, such as discrete dislocation plasticity where interfaces are modelled by cohesive zone models.

Cohesive zone models were introduced by Barenblatt [2] and Dugdale [3] to avoid the unrealistic stress singularity at the crack tip in classical fracture mechanics. Fracture is addressed as a gradual process, where it is assumed that no stress is transmitted between the fully separated crack surfaces, while a cohesive zone ahead of the crack continues to transmit forces between a pair of virtual surfaces. A traction-crack opening displacement constitutive law governs this behaviour.

Cohesive laws can either be coupled or uncoupled, and potential-based or non-potential-based. In an uncoupled cohesive law the normal traction is independent of the tangential crack opening, while the tangential traction is independent of the normal crack opening. This is appropriate when the debonding process occurs for one mode or is largely dominated by it. In coupled cohesive laws both the normal and the tangential tractions depend on the normal and tangential separations.

In a potential-based cohesive law the first derivatives of an interface potential function give the traction-separation relations. The most commonly implemented cohesive zone model is the model developed by Xu and Needleman [4] based on the potential ϕ:

$$\phi(u_n, u_t) = \phi_n + \phi_n \exp\left(-\frac{u_n}{\delta_n}\right)\left[\left\{1 - r + \frac{u_n}{\delta_n}\right\}\left(\frac{1-q}{r-1}\right)\right.$$
$$\left. -\left\{q + \left(\frac{r-q}{r-1}\right)\frac{u_n}{\delta_n}\right\}\exp\left(-\frac{u_t^2}{\delta_t^2}\right)\right], \quad (5.1)$$

where u_n and u_t are the normal and tangential separation across the interface, δ_n and δ_t are interface-characteristic length parameters, and q and r are coupling parameters that couple the normal and tangential behaviour,

$$q = \frac{\phi_t}{\phi_n}, \quad (5.2)$$

where ϕ_t is the work of tangential separation and ϕ_n is the work of normal separation, and

$$r = \frac{u_n^*}{\delta_n}, \quad (5.3)$$

where u_n^* is the normal separation after complete shear separation under zero normal traction.

The normal and tangential tractions are obtained by differentiating Equation 5.1 with respect to u_n, respectively u_t, which gives unique relations for $T_n(u_n, u_t)$ and $T_t(u_n, u_t)$. This cohesive zone model allows for shear-failure, since the tangential response is not periodic.

In order for this model to describe physically realistic interface behaviour the normal and tangential behaviour should be adequately coupled. Van den Bosch *et al.* [5] showed that only for $r = q$ the required tangential traction increases with increasing normal compression, as it does in friction. Furthermore, physical realistic coupling is obtained only for $q = 1$, since only then the required normal traction reduces to zero at complete shear separation. However, this implies that $\phi_t = \phi_n$, which experimental studies [6] have shown is often not true. Van den Bosch *et al.* [5] modified the Xu-Needleman cohesive zone model by allowing for $\phi_n \neq \phi_t$. This model is no longer potential-based.

Other cohesive zone models were developed by Park *et al.* [7], McGarry *et al.* [8], and Dimitri *et al.* [9], as we described in a previous work [10].

Conventionally the parameters for a traction-separation law are obtained empirically, from polycrystalline samples. However, in that case they reflect the average response of many interfaces. This is therefore inappropriate as a representation of constitutive behaviour of interfacial debonding at the nano-scale. To obtain the parameters of the cohesive law for accurately describing interfacial debonding at the nano-scale, atomistic simulations can be used.

As described in [10], various studies have been performed to determine cohesive zone law parameters with molecular dynamics (MD) simulations, such as [11–19]. However, none of these studies describe iron-precipitate interfaces under mixed loading conditions.

In a previous study we used MD to derive a cohesive law for pure normal loading for various iron-precipitate interfaces, assuming that the separations parallel to the interface are zero, which gives the relation between traction and separation during crack growth based on a universal adhesive energy equation [20]. In this study we used a model material X for the precipitate. Material properties of X will be given later on. To derive the universal adhesive energy relation, both the normal separation and the adhesive energy are scaled, according to

$$u^* = \frac{u_n}{\alpha}, \tag{5.4}$$

where α is the equilibrium pair interaction length between Fe and X as given by the Fe – X pair potential, and

$$E_{ad}^*(u^*) = E_{ad}/\Delta E, \tag{5.5}$$

where ΔE is the absolute value of the minimum adhesive energy. The universal adhesive energy relation is then given by

$$E_{ad}^* = -\left(1 + \theta u^* + \mu(\theta u^*)^3\right)\exp(-\theta u^*), \tag{5.6}$$

with parameter values that we found to be $\theta = 5.29$ and $\mu = -0.06$. From this universal adhesive energy relation the cohesive law describing the relation between normal traction

and normal separation is derived as

$$T_n(u_n) = c\theta \frac{\Delta E}{\alpha} \left[\mu \left(\theta \frac{u_n}{c\alpha} \right)^3 - 3\mu \left(\theta \frac{u_n}{c\alpha} \right)^2 + \theta \frac{u_n}{c\alpha} \right] \exp \left(-\theta \frac{u_n}{c\alpha} \right). \tag{5.7}$$

where c is a scaling factor, which is material (combination) dependent, to take into account atomic strains and rearrangements. For the Fe – X interfaces $c = 2.39$.

Previously we also derived a cohesive law to describe the response to a pure shear load for the same iron-precipitate interfaces [10]. Under a shear load these interfaces showed interface sliding. The relation between tangential traction and tangential separation depends on the interface structure and the loading direction. In [10] we found that a cohesive law describing the relation between tangential traction and tangential separation should be described in three parts: an elastic part for small separations, a steady-state sliding part for large separations, and a transition part in between, where the steady-state sliding behaviour develops. This cohesive law is given by

$$\begin{aligned}
T_t &= \frac{T_t^{crit}}{u_t^{crit}} u_t, & &\text{for } 0 \leq u_t \leq u_t^{crit}, \\
T_t &= \frac{T_t^{crit} - T_t^s}{(u_t^s - u_t^{crit})^2} (u_t - u_t^s)^2 + T_t^s, & &\text{for } u_t^{crit} \leq u_t \leq u_t^s, \\
T_t &= T_t^s, & &\text{for } u_t \geq u_t^s,
\end{aligned} \tag{5.8}$$

where u_t^{crit} is the separation at which the structure starts to slide and T_t^{crit} is the corresponding value of the traction; u_t^s is the separation at which steady-state sliding behaviour is reached and T_t^s is the corresponding sliding traction.

When a dislocation impinges on the interface when the system is subjected to a shear load, the dislocation might trigger a structure change of the interface from the impingement position onwards. In this case the cohesive law relating tangential traction to tangential separation should be modified to take this gradual structure change into account. The modified cohesive law is given by

$$T_t = (1 - \xi) T_t^{orig} + \xi T_t^{new}, \tag{5.9}$$

where T_t^{orig} is the original cohesive law for the unchanged interface and T_t^{new} is the cohesive law for the changed part of the interface. The time dependent parameter ξ expresses the progress of the change of the interface,

$$\xi = \frac{A_{new}}{A_{orig} + A_{new}}, \tag{5.10}$$

where A_{orig} is the area of the interface that still has the original structure and A_{new} is the area that has the changed structure.

In the present study we analyse the influence of mixed loading conditions on the relation between tractions and separations at the interface, since it is expected that a combination of normal and tangential loading will influence the relations for pure normal and pure tangential loading as given in Equations 5.7 and 5.8. In Section 5.2 the

choice of material, the set-up of the simulation, and the analysis methods are described. The influence of a previously applied normal load on the relation between tangential traction and tangential separation during shear loading, here called 'pre-tension' loading, is described in Section 5.3.1. The influence of a previously applied shear load on the relation between normal traction and normal separation during normal loading, here called 'pre-shear' loading, is described in Section 5.3.2. The response of the interfaces to a simultaneously applied normal and shear load, so called mixed-mode loading, is described in Section 5.3.3. In Section 5.4 the previously derived cohesive laws for pure normal and pure shear loading are adjusted to include the influence of the other loading direction under pre-shear, pre-tension and mixed-mode loading. The results are discussed in Section 5.5. Finally, in Section 5.6 the conclusions are drawn.

5.2. METHOD

5.2.1. MATERIAL DESCRIPTION

In this study the same iron-precipitate interfaces as in [20] and [10] are studied, but here under different loading conditions. Iron is described with the EAM-potential by Ackland *et al.* [21]. In the EAM format the potential energy of atom i is given by

$$U_i = F(\rho_i) + 1/2 \sum_j \phi_{ij}(r), \tag{5.11}$$

where F is the embedding energy of atom Fe or atom X as a function of the local electron density ρ_i, and ϕ_{ij} is the pair interaction between atom i and the surrounding atoms j as a function of their distance r. The local electron density ρ_i is made up from the contributions ψ_j to the electron density by the same atoms j surrounding atom i at distances r,

$$\rho_i = \sum_j \psi_j(r). \tag{5.12}$$

F, ϕ and ψ are relatively simple functions, parametrised for Fe. They can be found in the original paper [21]. The artificial precipitate material X is chosen to be material $X^{(3)}$ from [22]. Material X has a 10 % larger lattice constant than Fe and, as a result of the X – X pair interaction being twice as strong as that of Fe – Fe and the X- and Fe-embedding terms being equal, X has a 49 % larger Young's modulus than Fe. Material X is thus stiffer than Fe and, due to the different lattice constant, forms semi- or non-coherent interfaces with Fe. Dislocation transfer into the precipitate material is therefore hindered, just as it is in real precipitate materials found in steel, such as carbides and nitrides of different alloying elements. Similar to [22], the mixed Fe – X pair interaction is a linear combination of the individual Fe – Fe and X – X pair interactions,

$$\phi_{FeX} = q(\phi_{FeFe} + \phi_{XX}), \tag{5.13}$$

where the factor q in this study equals 1/3. This Fe – X pair interaction in combination with the orientations of the Fe and X grains on either side of the interface determines the interface strength. However, defects at the interface, those initially present but also those developing during loading and grain sliding, may be of significant additional influence.

5.2.2. SETUP

The Fe – X system is schematically shown in Figure 5.1. The system size is dependent on the orientation of the crystals, and on average equals $165 \times 4.4 \times 110$ nm^3, with the number of atoms per system varying between 6 and 9 million. The system is periodic in x and y.

Figure 5.1: Setup of the simulations. The simulation box consists of an Fe – X bicrystal, which is periodic in $x-$ and $y-$direction. The atoms in region F are kept fixed, atoms in region M are mobile atoms, whose positions are updated by time integration, and the atoms in region D are moved with a constant strain rate of $\dot{\varepsilon} = 10^8$ s^{-1}. In the Fe grain one $\{112\}\langle 111\rangle$ edge dislocation is inserted close to the interface, so that upon minimisation it moves towards the interface. The X grain is the precipitate material.
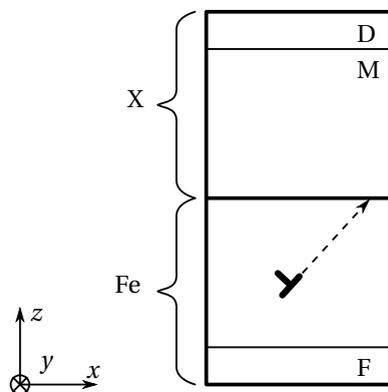
The orientations of the 11 different interfaces, being the same as the ones studied in [20] and [10], are listed in Table 5.1. Since in α-iron the typical cleavage plane is the (100) plane, with the crack front direction in either the [001] or the [011] direction, the most logical starting point for the study of interface decohesion, as is also the focus of [20], is a system with the (100) plane in the interface, which upon decohesion becomes the crack plane. To study the interaction of a dislocation with such an interface, the dislocation line has to be in a periodic direction to avoid edge effects. The choice is therefore made to study dislocations of the $\{112\}\langle 111\rangle$ slip system, so that the dislocation line is in the [011] direction, which, with the (100) plane at the interface, is the crack front direction. With this as starting point, the orientations of the iron and precipitate crystal are varied to obtain the orientations given in Table 5.1. The simulations are performed with one dislocation present in the iron grain at the interface. The dislocation is initially placed in the iron grain at 10 Å underneath the interface by removing a half plane of atoms. Upon energy minimisation the dislocation moves to the interface where it halts. By starting the simulations with the dislocation at the interface, instead of far below the interface, the influence of the different angles between glide plane and loading direction for the different oriented Fe grains is minimised.

In the simulations atoms in the lower 10 Å are kept fixed, region F in Figure 5.1. On atoms in the upper 10 Å, region D, a displacement is imposed so that a constant strain rate $\dot{\varepsilon}$ of 10^8 s^{-1} results. For the mobile atoms, region M, time integration using a time step of 5 fs is performed at 1 K with a Nosé-Hoover thermostat. Prior to loading, the system is equilibrated at 1 K for 100 ps. The stress σ that results from the applied strain is calculated by summing the resulting forces on the atoms in region D and dividing this by the area in the x, y-plane.

The very low temperature of 1 K was chosen to be able to see details of the atomic behaviour driving the interface dynamics. At higher temperatures these details would

Table 5.1: Orientations of the Fe and X grains giving the 11 different interface structures. The angle between the dislocation glide direction and the interface is given as ζ in Fe and η in X. All interfaces have been given a label just to identify them. Interfaces with the same letter(s) have one grain in the same orientation.

		Fe			X			ζ (°)	η (°)
		x	y	z	x	y	z		
(100) Fe	S1	[01$\bar{1}$]	[011]	[100]	[11$\bar{1}$]	[011]	[2$\bar{1}$1]	35.3	0.00
	S2	[01$\bar{1}$]	[011]	[100]	[01$\bar{1}$]	[011]	[100]	35.3	35.3
	S3	[01$\bar{1}$]	[011]	[100]	[$\bar{2}$3$\bar{3}$]	[011]	[31$\bar{1}$]	35.3	60.5
	S4	[01$\bar{1}$]	[011]	[100]	[21$\bar{1}$]	[011]	[1$\bar{1}$1]	35.3	90.0
(100) X	Fe1	[11$\bar{1}$]	[011]	[2$\bar{1}$1]	[01$\bar{1}$]	[011]	[100]	0.00[a]	35.3
	Fe3	[$\bar{2}$33]	[011]	[31$\bar{1}$]	[01$\bar{1}$]	[011]	[100]	60.5	35.3
	Fe4	[21$\bar{1}$]	[011]	[1$\bar{1}$1]	[01$\bar{1}$]	[011]	[100]	90.0[b]	35.3
(110) Fe	X1	[001]	[1$\bar{1}$0]	[110]	[111]	[1$\bar{1}$0]	[11$\bar{2}$]	54.7	0.00
	X2	[001]	[1$\bar{1}$0]	[110]	[113]	[1$\bar{1}$0]	[33$\bar{2}$]	54.7	29.5
	X3	[001]	[1$\bar{1}$0]	[110]	[001]	[1$\bar{1}$0]	[110]	54.7	54.7
	X4	[001]	[1$\bar{1}$0]	[110]	[$\bar{1}\bar{1}$2]	[1$\bar{1}$0]	[111]	54.7	90.0

[a] The dislocation is placed in the [1$\bar{1}$1] direction, giving an angle between slip plane and crack plane of 70.6°.

[b] The dislocation is placed in the [$\bar{1}\bar{1}$1] direction, giving an angle between slip plane and crack plane of 19.4°.

be hidden by thermal vibrations.

The particular interface realisations for each of the 11 crystal orientations are the same as those in [20], where they were created using the method described by Tschopp and McDowell [23]. A systematic collection of interface structures was generated for each crystal orientation by energy minimisation following extremely small initial displacements in the x and y directions. Of all the possible interface structures thus generated, the structure of which the interface energy has the highest number of occurrences in the collection is chosen as the final realisation.

5.2.3. LOCAL BEHAVIOUR

Similar to [20], to calculate the local response to the applied load in the interface region, the region is divided into multiple bins along the $x-$direction. Each bin is then divided in two: one half above the interface, one half underneath, as shown in Figure 5.2. The width of each bin, δx, was chosen to be 8.8 Å, or five atomic [100] planes. The height of the bins, δz, was chosen as 20 Å. This ensures that the total interface region, which is the region in which significant extra strain is seen with respect to the bulk, is taken into account in the calculations made over each bin [20].

For every bin k the stress is calculated as the average of the stresses on the N_k atoms j in the bin, according to

$$\sigma_{\alpha\beta k} = \frac{1}{N_k} \sum_{j=1}^{N_k} \sigma_{\alpha\beta kj}. \tag{5.14}$$
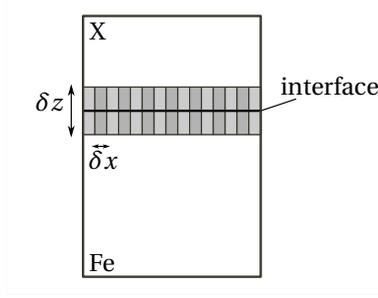
Figure 5.2: Division of interface region into bins with width δx of 8.8 Å and height δz of 20 Å. The bins have a role only in the data analysis, not in the simulation.

The normal traction T_n in a bin is equal to the $\alpha\beta = zz$ component of this average stress in the bin, and the tangential traction T_t is equal to the $\alpha\beta = xz$ component.

The normal and tangential separations u_n and u_t between the bins above and underneath the interface are calculated at the time of interest t as the increase in normal and tangential distance between the centers of mass (c) of these bins

$$
\begin{aligned}
u_n(t) &= z_c^X(t) - z_c^{Fe}(t) - (z_c^X(0) - z_c^{Fe}(0)), \\
u_t(t) &= x_c^X(t) - x_c^{Fe}(t) - (x_c^X(0) - x_c^{Fe}(0)),
\end{aligned}
\tag{5.15}
$$

where z_c^{Fe} is the z-position and x_c^{Fe} the x-position of the center of mass of the Fe-bin, below the interface, and z_c^X is the z-position and x_c^X is the x-position of the X-bin, above the interface. For simplicity of notation, T_n, u_n, T_t and u_t do not carry a subscript designating the bin to which they apply. The values for T_n, T_t, u_n and u_t were calculated every 100 time steps (500 fs) as an average over 10 time steps (50 fs).

To determine T_t and u_t, the division of atoms into bins is made once, at the beginning of the simulation. If, under the influence of a shear load, interface sliding occurs, the upper and lower half of the bin move apart. The increase in tangential distance between the bin halves gives u_t. However unlike the tangential case, T_n and u_n have to be determined between the upper and lower half of a bin for which the bin halves are still at roughly the same x-position. In order to determine T_n and u_n therefore, the division of atoms into bins is made every time step when these values are calculated.

As was shown in [10], in response to a shear load the individual bins do not always show equal $T_t(u_t)$ behaviour at the same moment in time. The average and the standard deviation of the response, however, is equal for all the bins. Therefore T_t can be averaged over all the bins at every desired moment in time. In addition to the $T_t(u_t)$ results for individual bins, the data are therefore also averaged over the entire interface and over time intervals of 10 ps. This averaging is done to smoothen the curves and get a better view on the similarities and differences between the different interfaces and loading directions. These average tangential traction data are indicated as $\overline{T_t}(u_t)$.

The response to a normal load is quite different for different bins at the same moment in time, as was shown in [20]. The relations between T_n and u_n of the bins are comparable, however. Therefore, instead of averaging the data of the individual bins at

a particular moment in time as is done for T_t, the data for T_n of the individual bins are averaged at particular values of u_n. These average normal traction data are indicated as $\overline{T_n}(u_n)$

5.2.4. LOADING

Three different kinds of mixed loading conditions are applied: 1.) pre-shear: a tensile load preceded by a shear load, 2.) pre-tension: a shear load preceded by a tensile load, and 3.) mixed-mode loading: simultaneously applied tensile and shear loads. The strain rate equals $10^8 \, \text{s}^{-1}$. For mixed-mode loading this is the total strain rate, which implies different normal and tangential strain rates under different loading angles. Under mixed-mode loading the mode-mixity angle is defined as the angle between the normal to the interface and the loading direction, so that an angle of $0°$ implies pure normal loading and $90°$ gives pure shear loading. Different mode-mixity angles ranging between $0°$ and $90°$ are studied.

5.2.5. METHODS

The MD-simulations are performed with LAMMPS [24, 25] and the GPU-accelerated version hereof [26–28]. The structures are visualised with OVITO [29]. As a measure for changes in the interface structure the number of non-bcc atoms at the interface is determined with the common neighbour analysis as implemented in LAMMPS [30, 31]. We found this to be a sensitive diagnostic for recording structural changes at an interface.

5.3. RESULTS

A schematic representation of the traction-separation relations for shear, pre-tension, mixed-mode, tension, and pre-shear loading of the different interfaces is given in Table 5.2. This table is intended to be a quick reference to the mechanical responses in the various situations studied. In Sections 5.3.1, 5.3.2, and 5.3.3 these results are discussed in detail.

5.3.1. PRE-TENSION

When the systems are subjected to a tensile load, the normal separation at the interface, u_n, increases. When subsequently a shear load is applied to the same system, it can be expected that the increased normal separation at the interface makes it 'easier' to shear the system, resulting in a lower tangential traction. As illustrated for the Fe4 interface in Figure 5.3, left, this effect is indeed seen. The longer the pre-tension time and therefore, since a constant strain rate is applied, the higher the normal strain, the lower the tangential traction is during shearing. Systems that were already 'easy' to shear without pre-tension, having a low tangential traction, stay 'easy' to shear, as illustrated for the X1 interface in Figure 5.3, right. The S4 interface, however, is an exception to this rule. As shown in Figure 5.3, middle, $\overline{T_t}$ is not influenced by the applied pre-tension. Only after 500 ps of pre-tension, the combination of the pre-tension and the subsequent tangential loading leads to decohesion of the interface, reflected in the decreasing blue curve for 500 ps of pre-tension for $u_t > 10$ Å.

An overview of the influence of pre-tension on the shearing behaviour is given in Fig-

Table 5.2: Schematic representation of the response of interfaces with a dislocation initially at the interface to different loading modes. For the X1 and X2 interface an applied shear load leads to a gradual change of the interface structure from the dislocation position onwards. The response therefore will be different for larger applied shear strains.

Interfaces	Shear	Pre-tension	Mixed-mode	Tension	Pre-shear	Mixed-mode
Fe3, Fe4, S3	T_t, u_t	T_t, u_t	T_t, u_t	T_n, u_n	T_n, u_n	T_n, u_n
Fe1	T_t, u_t	T_t, u_t	T_t, u_t	T_n, u_n	T_n, u_n	T_n, u_n
S1	T_t, u_t	T_t, u_t	T_t, u_t	T_n, u_n	T_n, u_n	T_n, u_n
X4	T_t, u_t	T_t, u_t	T_t, u_t	T_n, u_n	T_n, u_n	T_n, u_n
S4	T_t, u_t	T_t, u_t	T_t, u_t	T_n, u_n	T_n, u_n	T_n, u_n
X1, X2	T_t, u_t	T_t, u_t	T_t, u_t	T_n, u_n	T_n, u_n	T_n, u_n

5
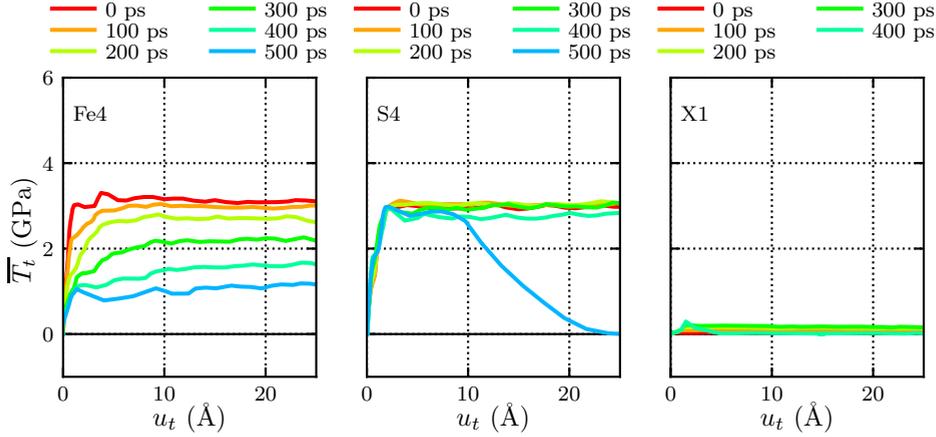
Figure 5.3: Tangential traction as function of tangential separation for three different interfaces after different amounts of pre-tension, indicated by the different pre-tension times, prior to loading the system in shear.

5

ure 5.4, where the sliding traction T_t^s is shown for ten interfaces after different amounts of pre-tension. A schematic representation of the influence of pre-tension on the entire traction-separation relation for shear is given in Table 5.2. Results for the S2 interface are not shown, since for this interface the structure dramatically changes during both pre-tension and shearing, and no steady-state sliding behaviour is reached after pre-tension. T_t^s can therefore not be determined for this interface.

5.3.2. PRE-SHEAR

The response of an interface to a tensile load is proportional to its adhesive energy, as is reflected in the normal cohesive law derived in [20], Equation 5.7. The different interfaces result from different crystal orientations and have, as a result, different interface structures with different adhesive energies. When a shear load is applied to the systems, the structure of the entire interface changes in certain cases [10], depending on the interface and on the loading direction. It could be expected that a change in interface structure also changes the adhesive energy of the interface and with that also changes the response of such an interface to a tensile load with respect to the original interface. For the Fe4 interface it is indeed seen that the pre-shear load leads to a changed normal traction during subsequent tensile loading, Figure 5.5.

The results for all interfaces are given in Figure 5.6, where the average of the maximum normal traction over all bins $\overline{T_n^{max}}$ is shown for nine of the interfaces after different amounts of pre-shear. A schematic representation of the influence of pre-shear on the entire traction-separation relation for tension is given in Table 5.2. Pre-shear can either make the system 'easier' to pull apart (Fe3, Fe4, S3), make it 'harder' (Fe1, S1), or have no significant influence (S4, X1, X2, X4). It turns out that whether or not a change in $\overline{T_n^{max}}$ is seen with increasing pre-shear time depends on whether or not the structure of the interface changes as a result of the applied shear load. So, indeed a changed interface
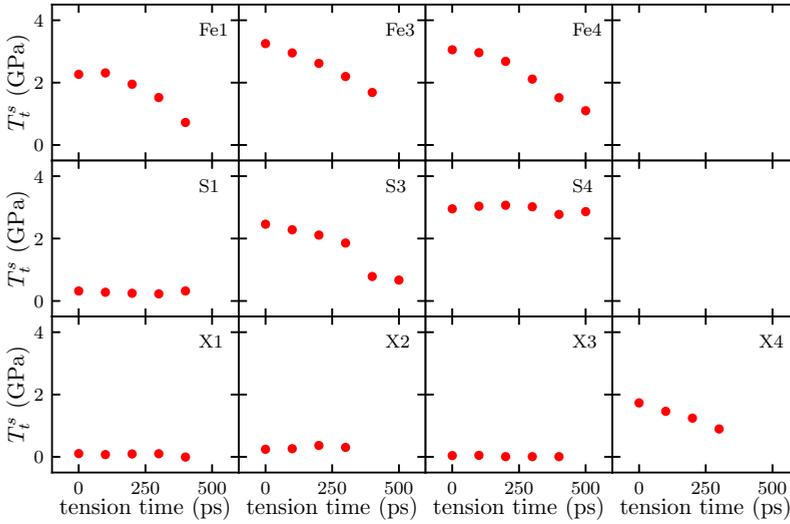
Figure 5.4: Sliding traction, T_t^s, during shearing as function of the pre-tension time, for ten different interfaces.

structure leads to a different $T_n(u_n)$ relation, since the adhesive energy of the interface is also changed. For the S2 and the X3 interface no graphs are shown, because they cannot be compared to the other results: in these cases pre-shear followed by tensile loading leads to the nucleation of a dislocation loop (S2) or to the reflection of the dislocation into iron (X3). This dislocation (loop) then moves towards the lower boundary, where it is stopped by the fixed atomic planes and causes a stress concentration. From this stress concentration multiple dislocations are nucleated, leading to failing of the structure in a different way than for the other interfaces, making it impossible to compare the crack growth between the different simulations and to determine meaningful values for $\overline{T_n^{max}}$ at the interface.
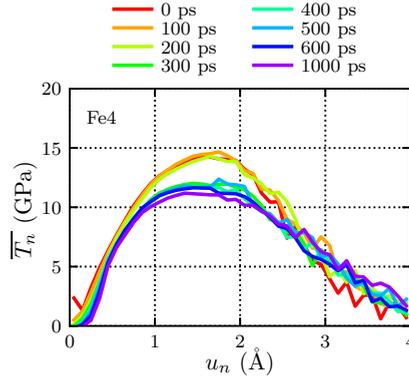
Figure 5.5: Normal traction as function of normal separation for the Fe4 interface under tensile loading after different amounts of pre-shear, indicated by the different pre-shear times.

5.3.3. MIXED MODE

The pre-shear and pre-tension loading conditions described in the previous sections might seem rather artificial. In practice, interfaces will be subjected to simultaneously combined shear and tensile loading, the so called mixed-mode loading. The pre-shear and pre-tension loading conditions, however, do give insight in the mechanisms that take place at the different interfaces under the different loading conditions. Based on this insight one can speculate what would happen during mixed-mode loading, as we will do in the following paragraphs.

Under mixed-mode loading conditions a combined shear and tensile load are applied to the system with a total strain rate of 10^8 s^{-1}. Based on the results for the pre-tension loading condition, Figure 5.4, one would expect that under mixed-mode loading a larger normal component of the load, i.e. a smaller mode-mixity angle, makes it 'easier' to shear the system for the Fe1, Fe3, Fe4, S3, and X4 interface. The normal component of the load causes u_n to increase, resulting in a smaller T_t^s. This behaviour is indeed seen, as illustrated for the Fe4 interface in Figure 5.7a. In contrast to the pre-tension simulations, once the system slides during mixed-mode loading the continued shearing and tensile loading lead to a continuously increasing u_n, which in turn leads to a decreasing T_t^s. This behaviour is indeed seen, as illustrated for the Fe4 interface in Figure 5.7a.

Similarly as under pre-shear loading, the shear component of the mixed-mode load leads to a changing interface structure, although the change can be different because of the simultaneously applied tensile component. The changed structure in turn influences the response to normal loading, as shown in Figure 5.7b. Under pre-shear loading after a certain amount of pre-shear loading a steady-state sliding regime is reached and further shear loading has no additional influence on the normal loading behaviour (Figure 5.5). Under mixed-mode loading however, as shown in Figure 5.7b, increasing the shear component leads to a gradual decrease in the normal traction for the Fe4 interface, since under mixed-mode loading the increasing shear is applied simultaneously with an increasing tensile load and therefore the interface structure gradually continues
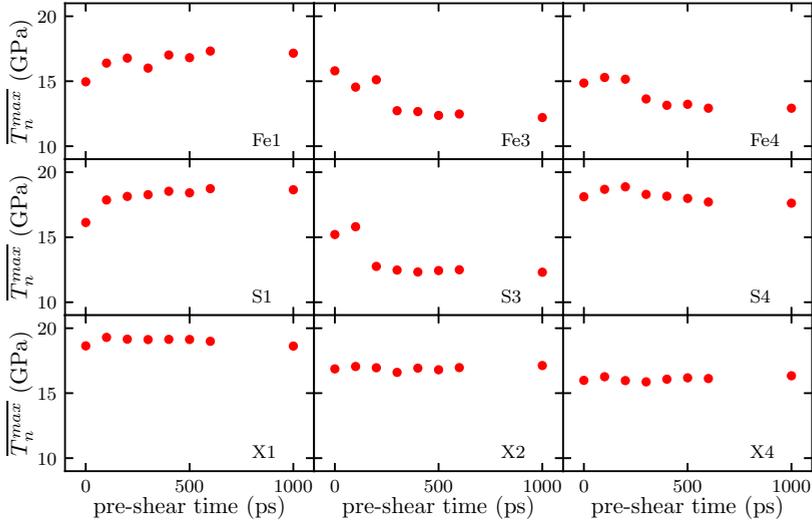
Figure 5.6: Average maximum normal traction during normal loading after different amounts of pre-shear are applied, indicated by the pre-shear time, for nine different interfaces.

(a)

(b)
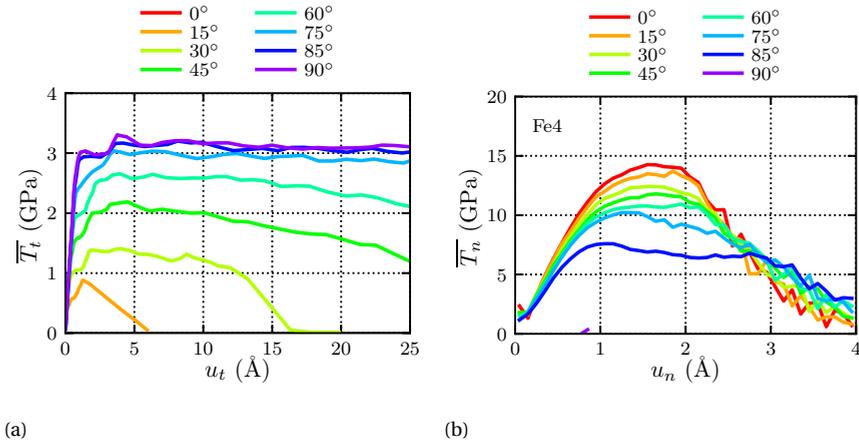
Figure 5.7: Fe4 interface under mixed-mode loading. Figure 5.7a shows that an increased normal loading component, so a smaller mode-mixity angle, leads to a decrease in $T_t(u_t)$ compared to the relation under pure shear (a mode-mixity angle of $90°$). Figure 5.7b shows that an increased shear loading component, so a larger mode-mixity angle, leads to a decrease in $T_n(u_n)$ compared to the relation under pure normal loading (a mode-mixity angle of $0°$).

to change.

An overview of the influence of the shear component of the mixed-mode load on the normal response is given for ten of the interfaces in Figure 5.8. A schematic representation of the influence of mixed-mode loading on the entire traction-separation relations for shear and tension is given in Table 5.2. For the X3 interface no data are shown, for the same reason as given in the case of pre-shear, Section 5.3.2.
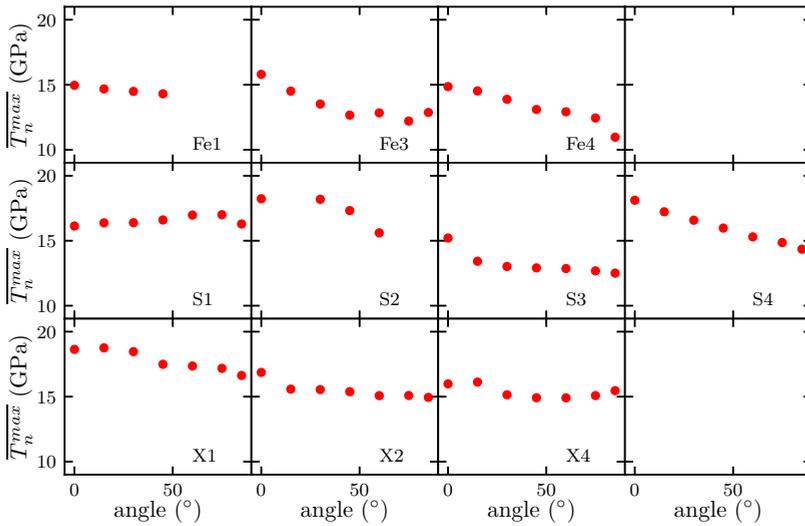
Figure 5.8: Average maximum normal traction during mixed-mode loading for different mode-mixity angles for ten different interfaces.

Comparing Figures 5.6 and 5.8 shows that the influence of the shear load on the normal behaviour is not for all interfaces the same under mixed-mode and pre-shear loading conditions. The third and fourth column in Table 5.2 further illustrate this. To compare the influence of the different loading paths on the response, in Figure 5.9 both $\overline{T_n}$ and $\overline{T_t}$ are shown as function of u_t for different values of u_n. The red dots show the values obtained with mixed-mode loading, while the blue dots result from pre-shear loading. For the Fe4 interface, as shown in Figure 5.9, both loading paths give similar results. In this case, therefore, u_n and u_t have the role of 'state parameters', i.e. representing the traction behaviour irrespective of the history through which the interface has evolved to these particular u_n and u_t values. In Figure 5.10 the influence of the different loading paths on the response are shown for the S4 interface. For this interface the different loading paths clearly give different responses, perhaps not greatly different but certainly different in a significant way.
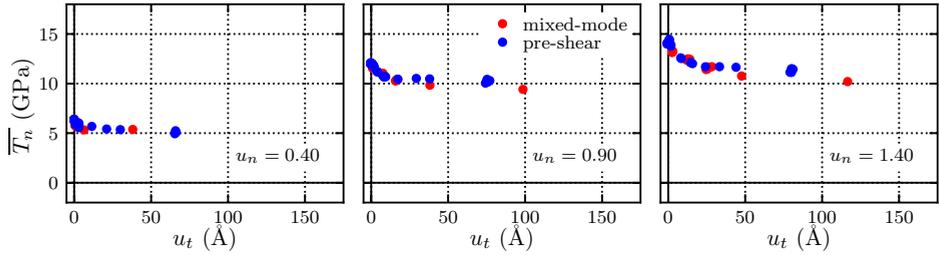
(a)
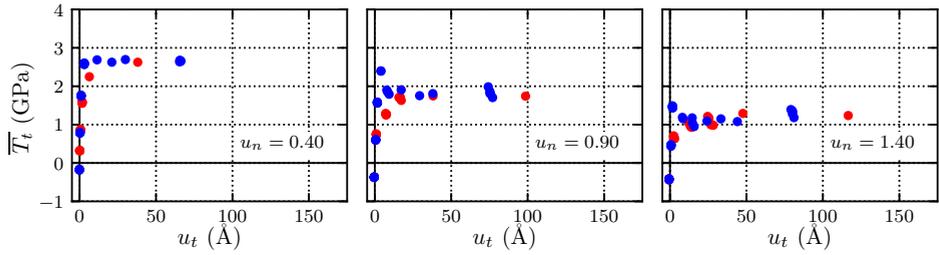
(b)

Figure 5.9: $\overline{T_n}(u_t)$ (a) and $\overline{T_t}(u_t)$ (b) for different values of u_n for the Fe4 interface under mixed-mode and pre-shear loading.
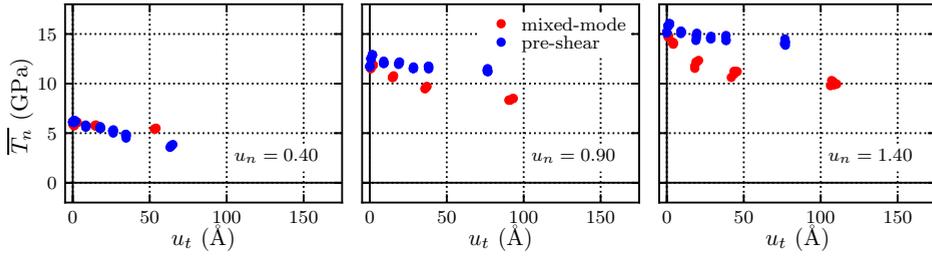
(a)
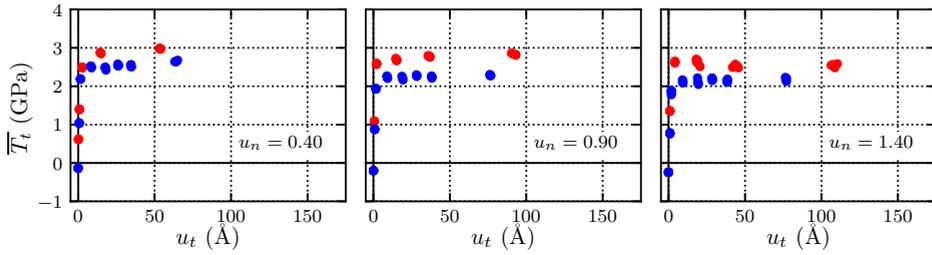
(b)

Figure 5.10: $\overline{T_n}(u_t)$ (a) and $\overline{T_t}(u_t)$ (b) for different values of u_n for the S4 interface under mixed-mode and pre-shear loading.

5.3.4. STRUCTURE CHANGE

The different tractions resulting from subsequently or simultaneously applied tangential and normal loading can be explained by different structure changes at the interfaces under different loading modes. As a measure for the structure change the number of non-bcc atoms per interface area is used. For the S4 interface the results for pre-shear and subsequent normal loading and for mixed-mode loading are compared in Figure 5.11. Note that the time in Figure 5.11a starts at the beginning of the simulation and thus includes both the pre-shear and the subsequent normal loading. Under pure tension, without pre-shear (0 ps) or with a mode-mixity angle of 0°, the number of non-bcc atoms increases with time until decohesion occurs, around 600 ps, upon which n_{int} drops and becomes a constant, reflecting that the two newly formed free surfaces revert to a much more bcc-like structure. In contrast, under a (pre-)shear load n_{int} slightly increases and becomes a constant during steady-state sliding. When the normal loading starts from this new structure, the structure changes are similar for different amounts of pre-shear loading, Figure 5.11a, since the starting structure for normal loading is similar after every amount of pre-shear. During mixed-mode loading the combined effect of normal and tangential loading leads to different structure changes for different mode-mixity angles, as illustrated in Figure 5.11b, and therefore, not surprisingly, to different $\overline{T_n}(u_n)$ behaviour, as was shown in Figure 5.10a. For this S4 interface a larger mode-mixity angle leads to less structure change at the interface and to a lower $\overline{T_n^{max}}$. For the other interfaces a difference in structure change between consecutively and simultaneously applied tangential and normal loading is also found, although sometimes less pronounced than for S4.

(a)

(b)
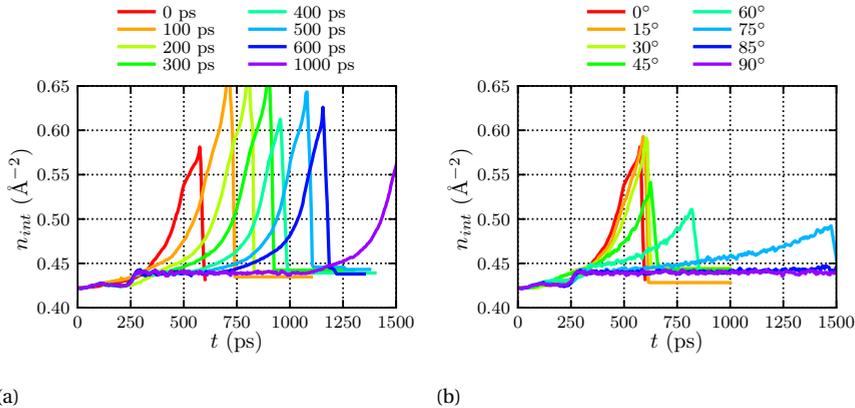
Figure 5.11: Change in interface structure, indicated by the number of non-bcc atoms at the interface per area as function of time, for the S4 interface during pre-shear (a) and mixed-mode (b) loading. Note that the time in (a) starts at the beginning of the simulation and thus includes both the pre-shear and the subsequent normal loading.

5.3.5. OTHER EFFECTS

In Sections 5.3.1 to 5.3.3 results are shown for the 11 studied interfaces. However, in some cases other effects are seen than only interface decohesion or interface sliding. We report this here, just to illustrate the multitude of different effects that occur under conditions that differ only in the interface orientation. For the Fe1 interface, dislocation loops form from the interface into the iron grain under the three different loading modes but not for pure shear or pure tension. These loops coalesce and, due to the periodic boundary conditions, form a downwards moving twin plane. At the S2 interface loops are also seen to nucleate. Furthermore, under certain loading conditions a single dislocation nucleates from the interface. The dislocation initially placed at the X3 interface moves back into the iron grain under all loading conditions except pure shear. This dislocation is then blocked by the fixed atomic bottom planes, which leads to a stress concentration. From this stress concentration multiple dislocations nucleate, which in turn lead to failure of the structure in a different way than by pure interface decohesion.

Since in Sections 5.3.1 to 5.3.3 the influence of pre-shear, pre-tension or the mode-mixity angle on the tensile and shear behaviour is quantified by their effect on $\overline{T_n^{max}}$ and T_t^s, respectively, these parameters are shown only if meaningful values could be determined. However, for some interfaces the nucleated dislocations cause decohesion at multiple positions along the interface or at the boundary between fixed and dynamic atoms, which constitutes a new complication. A detailed investigation of this behaviour, however, is beyond the scope of this work.

In conclusion, the response of the interfaces to mixed-mode loading is different from the response to pre-shear or pre-tension loading. The loading direction and history determine the local stress state at the interface and with that determine the structure change that takes place at the interface. That, ultimately, influences the traction-separation behaviour.

5.4. COHESIVE LAW

In [20] a cohesive law for the relation between normal traction and normal separation during crack growth under pure normal loading was derived. Although it was found that crack nucleation is influenced by impinging dislocations, since they locally modify the structure of the interface, crack growth is independent of the number of dislocations under pure normal loading. In [10] a cohesive law for the relation between tangential traction and tangential separation under pure tangential loading was derived. This cohesive law does depend on dislocations, since dislocations can change the entire interface structure and with that influence the response of the interface. In the current section the two cohesive laws are adjusted to take into account the cross effects: the influence of normal loading on the shear behaviour and that of shear loading on the normal behaviour, based on the results from the pre-shear, pre-tension, and mixed-mode simulations.

5.4.1. PRE-SHEAR

The relation between normal traction and normal separation under pre-shear loading conditions can be derived from the previously derived [20] cohesive law for crack growth under pure normal loading, Equation 5.7, by including the influence of the shear load. If a shear load is applied to the system, the interface structure changes until a steady-state sliding regime is achieved. The largest structure change occurs until the peak of T_t is reached, as given by Equation 5.8. The new interface structure that forms under the applied shear load will have a different interface energy ΔE, and therefore a different relation for $T_n(u_n)$ under a subsequent normal load, than the original structure. The influence of the structure change can be included in the cohesive law by a mixing rule that describes the transition between beginning and end,

$$T_n = (1-\zeta)T_n^{orig} + \zeta T_n^{new}, \tag{5.16}$$

where T_n^{orig} is $T_n(u_n)$ for the original interface structure, T_n^{new} is $T_n(u_n)$ for the changed structure in the steady-state sliding regime, and ζ is a measure for the structure change, which ranges from $\zeta = 0$ for the original interface to $\zeta = 1$ for the sliding regime. Since the largest amount of structure change takes place until the peak in T_t is reached, ζ can be represented as follows:

$$
\begin{aligned}
&\text{if } T_t^s \geq T_t^{crit} : \zeta = \frac{u_t}{u_t^s}, \text{ for } 0 \leq u_t \leq u_t^s,\\
&\qquad\qquad \zeta = 1, \text{ for } u_t > u_t^s,\\
&\text{if } T_t^{crit} \geq T_t^s : \zeta = \frac{u_t}{u_t^{crit}}, \text{ for } 0 \leq u_t \leq u_t^{crit},\\
&\qquad\qquad \zeta = 1, \text{ for } u_t > u_t^{crit}.
\end{aligned}
\tag{5.17}
$$

In Figure 5.12 the results from the pre-shear simulations are shown for the Fe4 interface together with the predictions by the cohesive law given by Equations 5.7, 5.16 and 5.17. In order to determine the parameters for the cohesive law, Equation 5.7 is fitted to the data of the simulations with 0 and 1000 ps pre-shear to determine ΔE for the original and the changed interface, which in turn determines T_n^{orig} and T_n^{new}. The value of ζ is determined for every amount of pre-shear with Equation 5.17, using the average value of u_t along the interface after the indicated pre-shear time before normal loading, and using the values of u_t^{crit}, u_t^s, T_t^{crit} and T_t^s from [10].

For various interfaces the maximum values of T_n after different pre-shear times as calculated with Equation 5.16 are shown in Figure 5.13 as the blue crosses, together with the values determined from the actual pre-shear simulations, which are given by the red dots. Predictions by the cohesive law are only shown for those interfaces for which the presence of an initial dislocation modifies the interface behaviour only very slightly, not for those interfaces where the dislocation triggers a gradual structure change along the interface, leading to significantly different behaviour of the changed part of the interface, as described in [10]. T_n^{orig}, T_n^{new} and ζ are determined as described above for the Fe4 interface. As can be seen in Figure 5.13, Equation 5.16 quite well reproduces $\overline{T_n^{max}}$ from the simulations.
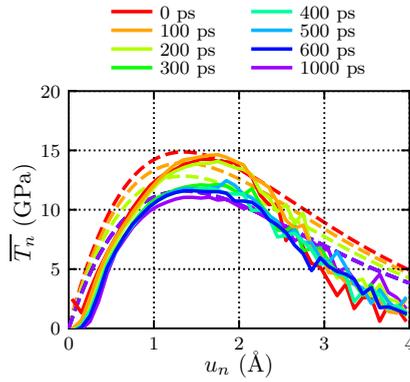
Figure 5.12: Normal traction as function of normal separation for the Fe4 interface under tensile loading after different amounts of applied pre-shear indicated by the different pre-shear times (solid lines), and as predicted by the cohesive law, Equations 5.7, 5.16 and 5.17 (dashed lines).
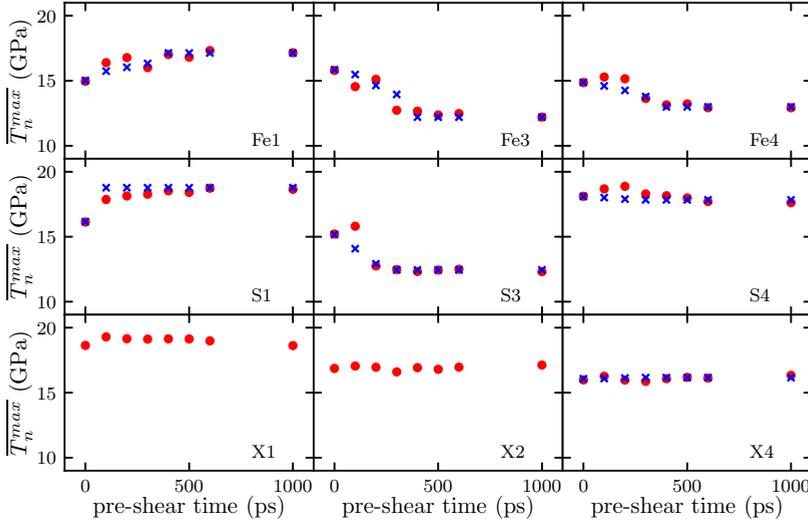
Figure 5.13: Average maximum normal traction during normal loading after different amounts of pre-shear are applied, indicated by the pre-shear time, for nine different interfaces (red dots). The blue crosses indicate T_n^{max} as predicted by Equation 5.16.

For the S2, X1, X2, and X3 interfaces shearing of the interface leads to a gradual structure change along the interface from the dislocation onwards, instead of to a gradual structure change of the entire interface over time as is seen for the other interfaces. In the same way as in the previously derived cohesive law [10], the gradual structure change should be included in the normal cohesive law by the factor

$$\xi = \frac{A_{new}}{A_{orig} + A_{new}}, \tag{5.18}$$

where A_{orig} is the area of the interface with the original structure and A_{new} is the area of the interface with the changed structure. The overal cohesive law for the entire interface is then given by

$$T_n = (1 - \xi) T_n^{orig} + \xi T_n^{new}, \tag{5.19}$$

where again T_n^{orig} is $T_n(u_n)$ for the original interface structure, and T_n^{new} is $T_n(u_n)$ for the part of the interface with the changed structure.

5.4.2. PRE-TENSION
Under pre-tension loading conditions the tensile load leads to an increase in u_n, which in turn may lead to a decrease in $\overline{T_t}$. The influence of u_n on $T_t(u_t)$ can be taken into account in a similar manner as u_t in the relation for $T_n(u_n)$,

$$T_t = (1 - \eta) T_t^{orig} + \eta T_t^{new}, \tag{5.20}$$

where T_t^{orig} is the original relation for $T_t(u_t)$ so without a normal load being applied, and T_t^{new} is the new relation for $T_t(u_t)$ that exists if u_n reaches its critical value u_n^{crit} at which decohesion takes place. However, upon decohesion there is no contact between the surfaces at the interface and therefore $T_t^{new} = 0$. The influence of u_n on the tangential behaviour is reflected in η, which ranges from $\eta = 0$ without normal load to $\eta = 1$ upon decohesion. We define η as the fraction of u_n^{crit} that u_n has reached,

$$\eta = \frac{u_n}{u_n^{crit}}, \text{ for } 0 \le u_n \le u_n^{crit}. \tag{5.21}$$

In Figure 5.14 the results from pre-tension simulations are shown for the Fe4 interface together with the predictions by the cohesive law given by Equations 5.8, 5.20 and 5.21. For every amount of applied pre-tension η is calculated with Equation 5.21 by using the average value of u_n along the interface after the indicated pre-tension time before shear loading. The cohesive law for pure normal loading, Equation 5.7, gives $u_n^{crit} = 1.35$Å.

5.4.3. MIXED-MODE
Under mixed-mode loading the structure change of the interface can be different from that under pre-shear or pre-tension loading conditions, as was illustrated in Figure 5.11. Equation 5.16 for pre-shear loading assumes that once the steady-state sliding regime is reached a new interface structure is formed, which no longer changes. If under mixed-mode loading the structure change is different from that under pre-shear loading for a
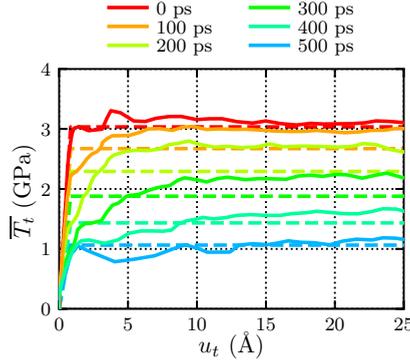
Figure 5.14: Tangential traction as function of tangential separation for the Fe4 interface under tensile loading after different amounts of pre-tension are applied, indicated by the different pre-tension times (solid lines), and as predicted by the cohesive law, Equations 5.8, 5.20 and 5.21 (dashed lines).

particular interface, T_n^{new} in Equation 5.16 is no longer a constant value for this interface, since for every mode-mixity angle a different structure and therefore a different T_n^{new} results. The next paragraphs describe for every interface how T_n^{new} is determined. In Table 5.3 the parameters for the cohesive laws for all the interfaces are given.

For interfaces Fe3, Fe4 and S3 T_n^{new} can be considered to be a constant. The structure changes during pre-shear and mixed-mode loading are quite comparable and, as illustrated in Figure 5.9 for the Fe4 interface, unique relations for $T_n(u_n, u_t)$ and $T_t(u_n, u_t)$ are found.

For interfaces S4 and X4 the structure change is different for pre-shear and mixed-mode loading and, as illustrated in Figure 5.10 for the S4 interface, no unique relations for $T_n(u_n, u_t)$ and $T_t(u_n, u_t)$ can be found. T_n^{new} is not constant for these interfaces, but ranges between T_n^{orig} and T_n^{new} as found with a mode-mixity angle of 85°, which is the largest mode-mixity angle studied at which decohesion occurs.

Also for interface S1 the structure change is different for pre-shear and mixed-mode loading and no unique relation for $T_n(u_n, u_t)$ and $T_t(u_n, u_t)$ can be found. For this interface T_n^{new} ranges between T_n^{new} in the steady-state sliding regime and T_n^{new} as found with a mode-mixity angle of 85°. In the steady-state sliding regime and under pre-shear loading conditions $T_n(u_n)$ increases, while under mixed-mode loading $T_n(u_n)$ decreases.

For interfaces X1 and X2 the dislocation at the interface causes a gradual structure change along the interface under an applied shear load. The rate at which this structure change proceeds is dependent on the sliding velocity of the upper crystal with respect to the lower crystal, as shown in [10], and therefore on the applied shear strain rate, which for mixed-mode loading is dependent on the mode-mixity angle. Furthermore, under mixed-mode loading the 'unchanged' part of the interface shows a different response for larger mode-mixity angles. For these two interfaces, as can be seen in Figure 5.6, an applied pre-shear up to 1000 ps has only a small influence on $\overline{T_n^{max}}$, since it is averaged over the entire interface and only a small part of the interface shows a structure change.

For a large mode-mixity angle, however, the structure change is spread much more along the interface, since in this case the applied shear strain is larger. This leads to a decrease in $\overline{T_n^{max}}$. For these interfaces T_n^{new} as found with a mode-mixity angle of 85° can be used.

The cohesive laws for normal and shear loading, Equations 5.7 and 5.8, and the modifications to include the influence of shear, respectively tension, in pre-shear and pre-tension simulations, Equations 5.16-5.21, with the parameters given in Table 5.3 describe the behaviour of the interfaces studied in this work. To describe the interface behaviour of other interfaces the parameters of the cohesive laws have to be determined. For this only a limited number of MD simulations are needed per interface and per loading direction:

- A static simulation to determine ΔE as described in [20].

- A shear simulation without initial dislocations to determine u_t^{crit}, u_t^s, T_t^{crit}, and T_t^s as described in [10].

- A tensile simulation on the interface structure formed in the steady-state sliding regime to determine T_n^{new}.

- A mixed-mode simulation with a mode-mixity angle of 85° to determine T_n^{new} if the mixed-mode behaviour is different from the pre-shear behaviour and a range has to be found in which T_n^{new} varies.

- A shear simulation with an initial dislocation to verify if this dislocation causes a gradual structure change of the interface from the dislocation position onwards. If so, $\dot{A}_{new}$ can be determined from this simulation, and a normal simulation for this changed interface has to be performed to determine T_n^{new}.

5.5. DISCUSSION

In [20] it was found that the cohesive law for normal loading can be determined based on an adhesive energy relation, Equation 5.7. The only factor differentiating the different interfaces was ΔE, the depth of the energy well, Equation 5.5. The scaling factor c was determined as an average of the scaling factors for the individual interfaces, which in turn were averages of the different simulations with different numbers of dislocations impinging on the interface. For some individual interfaces the simulation results showed small deviations from this universal normal cohesive law.

In our pre-shear simulations the value of ΔE for the changed interface in the steady-state sliding regime is not known beforehand. Instead, this value must be determined by fitting the maximum value of T_n to the normal cohesive law. Similarly, for improved accuracy for a particular interface, the maximum value of T_n from a pure normal simulation can be fitted to the cohesive law to determine ΔE. Of course, in this case not the real ΔE is found but an adjusted ΔE that includes the over- or undershoot of c for this interface.

Figures 5.9 and 5.10 clearly show that there is not a unique relation between the separations at the interface and the tractions for every interface. To properly describe the interface behaviour, no potential-based cohesive zone model can be applied if there is

no unique relation. Previous studies [5, 8] based on analytical derivations have already shown that a potential-based cohesive zone model is not capable to accurately describe interface behaviour. In this study, based on atomic-scale dynamics, we also find this. The interface structure and the change of this structure play key roles in the response to a load. To correctly capture the interface behaviour in a cohesive zone model, the structure change should therefore be included. Since the structure change depends on the order of applying shear and tensile loading, and a steady-state sliding regime can be reached, this structure change cannot be incorporated in a potential-based cohesive law.

The most commonly implemented cohesive zone model [4] has a non-periodic tangential response and therefore allows for shear failure. The cohesive law for pure shear behaviour derived in [10] is also non-periodic. However, with this cohesive law shear failure under pure shear loading will never occur, since a steady-state sliding regime is reached. Since our simulations, in [10, 20] and in the present study, involve the study of a periodic bi-crystal, the simulation set-up makes shear failure impossible.

In this study the focus is only on interface behaviour during loading and not during unloading. Since the relation between tractions and separations at the interfaces is dependent on the structure change, which in turn is determined by the loading path, it is impossible to predict the unloading behaviour of the interfaces with the currently derived cohesive model. Further study is necessary to capture the unloading behaviour.

In this study only a dislocation of the $\{112\}\langle111\rangle$ slip system interacts with the interface. Since the dislocation interacts with the interface under an angle, it can be expected that a different structure change will result for a dislocation of the same slip system but under a different angle, and that therefore the interface behaviour will be different. Similarly, a dislocation of another slip system will very likely cause a different structure change at the interface and therefore have a different influence on the shearing behaviour.

Before a crack grows in our simulations, it first has to nucleate. In [20] it was shown that under normal loading the crack *nucleation* behaviour is influenced by impinging dislocations, while the crack *growth* behaviour is not. In that work the crack nucleation was excluded from the determination of the crack growth behaviour. As explained in Section 5.2.3, to determine T_t and u_t the interface is divided into bins at the beginning of the simulations, while to determine T_n and u_n this division is made every time step when these values are calculated. When, under an applied shear load, the upper crystal starts sliding with respect to the lower crystal, the upper and lower parts of the bins move apart. If then a crack forms, under a subsequently or simultaneously applied tensile load, it is not evident which bins to exclude from the analysis of the growth behaviour in order to separate the nucleation behaviour. We therefore chose in this work not to exclude the nucleation behaviour in the determination of the crack growth behaviour. Since there are at least 175 bins along every interface, the error made by not excluding the nucleation behaviour in the crack growth behaviour is quite small. The crack nucleation behaviour itself will be discussed in a separate work [32].

In [20] and [10] the interface behaviour was studied with and without dislocations under tensile and shear loading. It was found that under tensile loading dislocations only influence the nucleation behaviour, while under shear loading, for some interfaces,

dislocations in combination with the shear load cause a gradual change of the interface structure from the dislocation position onwards. In the current work all simulations are performed with an initial dislocation present at the interface, in order to trigger crack nucleation at a specific point instead of at a number of random positions. In those cases where the dislocation causes a gradual structure change of the interface, this is taken into account in the cohesive law by Equations 5.18 and 5.19.

5.6. CONCLUSIONS

In this work we studied the behaviour of 11 different interfaces under a shear load followed by tensile loading ('pre-shear'), a tensile load followed by shear loading ('pre-tension'), and under simultaneously applied shear and tensile loading, ('mixed-mode loading'). We find that the interface structure and the change in this structure during loading play key roles in the response to the loading. This structure change is influenced by the loading history and by the loading direction. This leads to the overall conclusion that the details of the responses of various interfaces to various loading sequences are too complex to be captured in a relatively simple scheme, see also Table 5.2.

Only a few general conclusions emerge:

- if a shear load changes the structure of an interface, the response to a subsequent tensile load will be different from that of the original unchanged interface,

- if under an applied shear load a barrier has to be overcome to commence sliding, first applying a tensile load will make it easier to shear the system,

- if a previously applied shear load makes it harder to obtain decohesion in the system during tensile loading, applying a shear and tensile load simultaneously will reduce this effect, since the tensile load makes shearing easier.

We have adjusted our previously derived cohesive laws for pure normal and pure shear loading [10, 20] to take into account the influence of an earlier or simultaneously applied different loading direction. For some of the interfaces a unique relation between traction and separation exists. For other interfaces, however, no unique relation exists and our cohesive law gives no exact prediction but rather a range of possible values. This in itself is not without merit for modelling, since random values within this range can be assigned to different interfaces of the same type in a polycrystalline model. For computational practice we find that for every iron-precipitate interface a maximum of five MD simulations are needed to obtain the parameters of the cohesive zone model and to be able to fully predict the traction-separation behaviour in larger-scale models than MD.

APPENDIX
5.A. PARAMETERS

Table 5.3: Parameters for the cohesive laws given in Equations 5.7, 5.8, 5.16, 5.19, and 5.20. Values for ΔE are in eV/Å², values for u_t^{crit} and u_t^s are in Å, values for T_t^{crit}, T_t^s, T_n^{orig}, and T_n^{new} are in GPa. If only T_n^{new} for steady-state sliding is given, this is the actual value for T_n^{new}. If only T_n^{new} for a mode-mixity angle of 85° is given, this indicates a range, the actual value varying between this value and T_n^{orig}, depending on the loading mode, as described in Section 5.4.3. Where two values for T_n^{new} are given, the actual value varies between the two. For the Fe1, S2, and X3 interface no values are given for various reasons as explained in the main text.

Interface	ΔE	u_t^{crit}	u_t^s	T_t^{crit}	T_t^s	T_n^{orig}	T_n^{new} steady-state sliding	T_n^{new} mode-mixity angle 85°
Fe1	0.0519	8.08	143.35	2.92	1.95	14.96	-	-
Fe3	0.0574	2.36	132.67	3.56	2.99	15.80	12.21	-
Fe4	0.0570	0.83	0.83	3.03	3.03	14.86	12.92	-
S1	0.0519	0.69	82.26	0.86	0.34	16.13	18.65	16.29
S2	0.0686	0.15	2.72	1.24	0.92	18.23	-	-
S3	0.0530	3.72	5.16	2.71	2.47	15.21	12.31	-
S4	0.0606	1.92	6.64	3.08	2.96	18.11	-	14.35
X1	0.0601	0.14	0.14	0.02	0.02	18.11	-	16.63
X2	0.0559	0.38	0.38	0.19	0.19	18.64	-	14.95
X3	0.0755	0.00	0.00	0.01	0.01	16.87	-	-
X4	0.0555	2.19	8.17	0.96	1.67	23.73	-	15.46

5

REFERENCES

[1] A. Elzas and B. J. Thijsse, *Crack growth at iron / precipitate interfaces under mixed loading conditions,* accepted by Mechanics of Materials (2018).

[2] G. I. Barenblatt, *The Mathematical Theory of Equilibrium Cracks in Brittle Fracture,* Advances in Applied Mechanics **7**, 55 (1962).

[3] D. Dugdale, *Yielding of steel sheets containing slits,* Journal of the Mechanics and Physics of Solids **8**, 100 (1960), arXiv:0021-8928(59)90157-1 [10.1016] .

[4] X. P. Xu and A. Needleman, *Void nucleation by inclusion debonding in a crystal matrix,* Modelling and Simulation in Materials Science and Engineering **1**, 111 (1993).

[5] M. J. van den Bosch, P. J. G. Schreurs, and M. G. D. Geers, *An improved description of the exponential Xu and Needleman cohesive zone law for mixed-mode decohesion,* Engineering Fracture Mechanics **73**, 1220 (2006).

[6] J. Dollhofer, W. Beckert, B. Lauke, and K. Schneider, *Fracture mechanical characterisation of mixed-mode toughness of thermoplast/glass interfaces,* Computational Materials Science **19**, 223 (2000).

[7] K. Park, G. H. Paulino, and J. R. Roesler, *A unified potential-based cohesive model of mixed-mode fracture,* Journal of the Mechanics and Physics of Solids **57**, 891 (2009).

[8] J. P. McGarry, É. Ó. Máirtín, G. Parry, and G. E. Beltz, *Potential-based and non-potential-based cohesive zone formulations under mixed-mode separation and over-closure. Part I: Theoretical analysis,* Journal of the Mechanics and Physics of Solids **63**, 336 (2014).

[9] R. Dimitri, M. Trullo, L. De Lorenzis, and G. Zavarise, *Coupled cohesive zone models for mixed-mode fracture: A comparative study,* Engineering Fracture Mechanics **148**, 145 (2015).

[10] A. Elzas, T. P. C. Klaver, and B. J. Thijsse, *Cohesive laws for shearing of iron / precipitate interfaces,* Computational Materials Science **152**, 417 (2018).

[11] X. W. Zhou, J. A. Zimmerman, E. D. Reedy Jr., and N. R. Moody, *Molecular dynamics simulation based cohesive surface representation of mixed mode fracture,* Mechanics of Materials **40**, 832 (2008).

[12] X. W. Zhou, N. R. Moody, R. E. Jones, J. A. Zimmerman, and E. D. Reedy Jr., *Molecular-dynamics-based cohesive zone law for brittle interfacial fracture under mixed loading conditions: Effects of elastic constant mismatch,* Acta Materialia (2009), 10.1016/j.actamat.2009.06.023.

[13] D. E. Spearot, K. I. Jacob, and D. L. McDowell, *Non-local separation constitutive laws for interfaces and their relation to nanoscale simulations,* Mechanics of Materials **36**, 825 (2004).

5

[14] D. E. Spearot, K. I. Jacob, D. L. McDowell, and S. J. Plimpton, *Effect of deformation path sequence on the behavior of nanoscale copper bicrystal interfaces,* Journal of Engineering Materials and Technology **127**, 374 (2004).

[15] C. R. Dandekar and Y. C. Shin, *Molecular dynamics based cohesive zone law for describing Al-SiC interface mechanics,* Composites Part A: Applied Science and Manufacturing **42,** 355 (2011).

[16] V. Yamakov, E. Saether, D. R. Phillips, and E. H. Glaessgen, *Molecular-dynamics simulation-based cohesive zone representation of intergranular fracture processes in aluminum,* Journal of the Mechanics and Physics of Solids **54,** 1899 (2006).

[17] V. Yamakov, E. Saether, and E. H. Glaessgen, *Multiscale modeling of intergranular fracture in aluminum: Constitutive relation for interface debonding,* Journal of Materials Science **43,** 7488 (2008).

[18] P. Gupta, S. Pal, and N. Yedla, *Molecular dynamics based cohesive zone modeling of Al (metal)-Cu50Zr50 (metallic glass) interfacial mechanical behavior and investigation of dissipative mechanisms,* Materials and Design **105,** 41 (2016).

[19] B. Paliwal and M. Cherkaoui, *An improved atomistic simulation based mixed-mode cohesive zone law considering non-planar crack growth,* International Journal of Solids and Structures **50,** 3346 (2013).

[20] A. Elzas and B. J. Thijsse, *Cohesive law describing crack growth at iron/precipitate interfaces,* Computational Materials Science **134,** 214 (2017).

[21] G. J. Ackland, M. I. Mendelev, D. J. Srolovitz, S. Han, and A. V. Barashev, *Development of an interatomic potential for phosphorus impurities in α-iron,* Journal of Physics: Condensed Matter **16,** S2629 (2004).

[22] A. Elzas and B. J. Thijsse, *Dislocation impacts on iron/precipitate interfaces under shear loading,* Modelling and Simulation in Materials Science and Engineering **24,** 85006 (2016).

[23] M. A. Tschopp and D. L. McDowell, *Structures and energies of $\Sigma 3$ asymmetric tilt grain boundaries in copper and aluminium,* Philosophical Magazine **87,** 3147 (2007).

[24] *LAMMPS Molecular Dynamics Simulator,* http://lammps.sandia.gov.

[25] S. J. Plimpton, *Fast Parallel Algorithms for Short-Range Molecular Dynamics,* Journal of Computational Physics **117,** 1 (1995).

[26] W. M. Brown, P. Wang, S. J. Plimpton, and A. N. Tharrington, *Implementing Molecular Dynamics on Hybrid High Performance Computers - Short Range Forces,* Computer Physics Communications **182,** 898 (2011).

[27] W. M. Brown, A. Kohlmeyer, S. J. Plimpton, and A. N. Tharrington, *Implementing Molecular Dynamics on Hybrid High Performance Computers - Particle-Particle Particle-Mesh,* Computer Physics Communications **183,** 449 (2012).

5

[28] W. M. Brown and Y. Masako, *Implementing molecular dynamics on hybrid high per-
      formance computers – Three-body potentials,* Computer Physics Communications
      184, 2785 (2013).

[29] A. Stukowski, *Visualization and analysis of atomistic simulation data with
      OVITO–the Open Visualization Tool,* Modelling Simul. Mater. Sci. Eng. **18**, 015012
      (2009).

[30] D. Faken and H. Jónsson, *Systematic analysis of local atomic structure combined
      with 3D computer graphics,* Computational Materials Science **2**, 279 (1994).

[31] H. Tsuzuki, P. S. Branicio, and J. P. Rino, *Structural characterization of deformed
      crystals by analysis of common atomic neighborhood,* Computer Physics Communi-
      cations **177**, 518 (2007).

[32] A. Elzas and B. J. Thijsse, *Crack nucleation at iron/precipitate interfaces in the pres-
      ence of dislocations under different loading conditions,* submitted to Engineering
      Fracture Mechanics (2018).

5

6

CRACK NUCLEATION AT IRON/PRECIPITATE INTERFACES IN THE PRESENCE OF DISLOCATIONS UNDER DIFFERENT LOADING CONDITIONS

Dislocations piling up at interfaces in metallic microstructures cause stress concentrations. These stress concentrations can lead to interface decohesion. This in turn can lead to the formation of voids, which, when they coalesce, can form a macroscopic crack. Interface decohesion can be described by cohesive zone models which relate the tractions to the separations at the interface. In these cohesive zone models typically no distinction is made between crack nucleation and crack growth. In this work we study the crack nucleation behaviour for 11 different iron/precipitate interfaces and we investigate how this is influenced by the number of dislocations and the loading mode. We find that under pure normal loading crack nucleation occurs according to the same traction-separation relation as crack growth only in the absence of dislocations. Dislocations at the interface as well as different loading modes change the traction-separation relation during crack nucleation, and, depending on the interface, also during crack growth. We explain how the influence of dislocations and loading modes should be included in a cohesive zone model to properly describe both the nucleation and the growth of a crack at an interface.

115

6.1. INTRODUCTION

Interfaces in metallic microstructures act as a barrier for dislocation motion. When dislocations pile-up at an interface, they cause a stress concentration, which in turn might trigger interface decohesion. This can result in the formation of voids and eventually in the formation of a macroscopic crack. Multiphase alloys such as advanced high strength steels show limited ductility due to such decohesion at internal boundaries.

The mechanical failure of materials with pre-existing cracks can be captured by classical fracture mechanics. To avoid the unrealistic stress singularity at the crack tip in classical fracture mechanics, Barenblatt [2] and Dugdale [3] introduced cohesive zone models. In these models, fracture was addressed as a gradual process, where it was assumed that no stress was transmitted between the fully separated crack surfaces. A cohesive zone ahead of the crack continues to transmit forces between a pair of virtual surfaces. This behaviour is governed by a traction-crack opening displacement constitutive law.

The parameters for a traction-separation law can either be obtained empirically from polycrystalline samples, or, to describe interfacial debonding at the nano-scale, from atomistic simulations. When cohesive zone models are employed to describe interface decohesion, typically no distinction is made between crack nucleation and crack growth. However, in the determination of the parameters for cohesive zone models from molecular dynamics simulations (MD) they are often determined from simulations with pre-existing cracks [4]. Two questions now arise: (1) are these cohesive zone models also valid to describe crack nucleation or does nucleation occurs according to a different traction-separation relation, and (2) have dislocations an influence on the crack nucleation behaviour in the sense that dislocations make nucleation obey a different traction-separation relation.

Although quite some research is done on the understanding and modelling of fatigue crack initiation (see [5] for an overview), little is known on crack nucleation at the atomic scale. Pan and Rupert [6] used MD simulations to investigate crack nucleation at an fcc Cu grain boundary, triggered by dislocation absorption. From their simulations they found that the capability of a grain boundary to absorb free volume determines the crack nucleation resistance. The exact traction-separation relations at crack nucleation, however, are not quantified in their work.

In this work we study the crack nucleation at iron-precipitate interfaces under different loading conditions. The traction-separation relations during crack nucleation are determined. The influence of dislocations, either already present at the interface or impinging on the interface, on the crack nucleation behaviour is determined. How the crack nucleation behaviour, and the influence of dislocations on this, should be included in a cohesive zone model is also discussed. The main conclusions are that only in the absence of dislocations, under pure tensile loading, crack *nucleation* obeys the same traction-separation relation as crack *growth*. In the presence of dislocations and/or under different loading modes, crack *nucleation* occurs according to different traction-separation relations than crack *growth*, while the number of dislocations and the loading mode both can influence the crack nucleation and crack growth relations.

Elaborating on our previous work on the derivation of a cohesive zone model for crack *growth* at bcc iron-precipitate interfaces [7–10], we now study the crack *nucleation*

at these interfaces. In Section 6.2 the choice of material, the set-up of the simulations and the analysis methods are described. The crack nucleation behaviour under tensile loading in the absence of dislocations is described in Section 6.3.1, the influence of an initial dislocation at the interface is described in Section 6.3.2 and the effect of impinging dislocations is described in Section 6.3.3. The nucleation behaviour under mixed loading conditions with and without dislocations is described in Section 6.3.4. How the nucleation behaviour should be included in a cohesive zone model is discussed in Section 6.4. Finally, in Section 6.5 some conclusions are drawn.

6.2. METHOD

6.2.1. MATERIAL DESCRIPTION

In this study the same iron-precipitate interfaces as in [8], [9] and [10] are studied, but in this work the focus is on the crack nucleation behaviour. To describe iron in our simulations a potential had to be chosen that accurately describes both edge dislocations in iron and the structures far from equilibrium resulting from dislocation pile-up/interface interactions. To describe a single edge dislocation in iron, the potential developed by Malerba *et al.* [11], optimised to describe interstitials and vacancy defects, is a reliable choice. However, since in the present study not just single edge dislocations but also pile-ups of dislocations interacting with interfaces are studied, structures far from equilibrium are expected for which this potential is less appropriate [4]. Studies of crack tips [4, 12] have shown that both 'potential 2' developed by Mendelev *et al.* [13] and the potential developed by Ackland *et al.* [14] are reliable potentials for this type of study. Although they are both derived from nearly the same input data and predict nearly the same material properties, this does not result in a qualitatively same description of material behaviour at a crack tip [12]. In this study iron is described with the EAM-potential by Ackland *et al.* [14]. In the EAM format the potential energy of atom i is given by

$$U_i = F(\rho_i) + 1/2 \sum_j \phi_{ij}(r), \tag{6.1}$$

where F is the embedding energy of atom Fe or atom X as a function of the local electron density ρ_i, and ϕ_{ij} is the pair interaction between atom i and the surrounding atoms j as a function of their distance r. The local electron density ρ_i is made up from the contributions ψ_j to the electron density by the atoms j surrounding atom i at distances r,

$$\rho_i = \sum_j \psi_j(r). \tag{6.2}$$

F, ϕ and ψ are relatively simple functions, parametrised for Fe. They can be found in the original paper [14]. The artificial precipitate material X is chosen to be material $X^{(3)}$ from [7]. In this work we choose $\phi_{XX} = 2\phi_{FeFe}$, $a_X = 1.1a_{Fe}$, and the embedding term $F(\rho_i)$ is equal for Fe and X atoms. To create material X with lattice constant $a_X = 1.1a_{Fe}$, we use

$$\begin{aligned} \phi_{XX}(r) &= 2\phi_{FeFe}(r/1.1), \\ \psi_X(r) &= \psi_{Fe}(r/1.1). \end{aligned} \tag{6.3}$$

X has thus a 10 % larger lattice constant than Fe and, as a result of the X – X pair interaction being twice as strong as that of Fe – Fe and the X– and Fe–embedding terms being equal, X has a 49 % larger Young's modulus than Fe. Material X is thus stiffer than Fe and, due to the different lattice constant, forms semi- or non-coherent interfaces with Fe. Dislocation transfer into the precipitate material is therefore hindered, just as it is in real precipitate materials found in steel, such as carbides and nitrides of different alloying elements. Similar to [7] the mixed Fe – X pair interaction is a linear combination of the individual Fe – Fe and X – X pair interactions,

$$\phi_{FeX} = q(\phi_{FeFe} + \phi_{XX}),\qquad(6.4)$$

where the factor q in this study equals 1/3. This Fe – X pair interaction in combination with the orientations of the Fe and X grains on either side of the interface determines the interface strength. However, defects at the interface, initially present but also those developing during loading and grain sliding, may be of significant additional influence.

6.2.2. SETUP

The Fe – X system is schematically shown in Figure 6.1. The system size is dependent on the orientation of the crystals, and on average equals $165 \times 4.4 \times 110$ nm^3, with the number of atoms per system varying between 6 to 9 million. The system is periodic in x and y.

Figure 6.1: Setup of the simulations. The simulation box consists of an Fe – X bicrystal, which is periodic in $x-$ and $y-$direction. The atoms in region F are kept fixed, atoms in region M are mobile atoms, whose positions are updated by time integration, and the atoms in region D are moved with a constant strain rate of $\dot{\varepsilon} = 10^8$ s^{-1}. In the Fe grain one or more $\{112\}\langle111\rangle$ edge dislocations can be inserted. The X grain is the precipitate material.
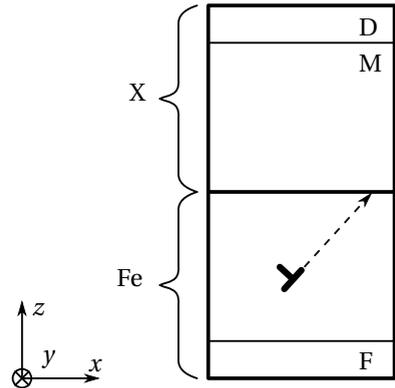
The orientations of the 11 different interfaces, being the same as the ones studied in [8], [9] and [10], are listed in Table 6.1. Since in α-iron the typical cleavage plane is the (100) plane, with the crack front direction in either the [001] or the [011] direction, the most logical starting point for the study of interface decohesion is a system with the (100) plane at the interface, which upon decohesion becomes the crack plane. To study the interaction of a dislocation with such an interface, the dislocation line has to be in a periodic direction to avoid edge effects. The choice is therefore made to study dislocations of the $\{112\}\langle111\rangle$ slip system, so that the dislocation line is in the [011] direction, which, with the (100) plane at the interface, is the crack front direction. With this as starting point, the orientations of the iron and precipitate crystal are varied to obtain the

Table 6.1: Orientations of the Fe and X grains giving the 11 different interface structures. The angle between the dislocation glide direction and the interface is given as ζ in Fe and η in X. All interfaces have been given a label just to identify them. Interfaces with the same letter(s) have one grain in the same orientation.

		Fe			X			ζ (°)	η (°)
		x	y	z	x	y	z		
(100) Fe	S1	$[01\bar{1}]$	$[011]$	$[100]$	$[11\bar{1}]$	$[011]$	$[2\bar{1}1]$	35.3	0.00
	S2	$[01\bar{1}]$	$[011]$	$[100]$	$[01\bar{1}]$	$[011]$	$[100]$	35.3	35.3
	S3	$[01\bar{1}]$	$[011]$	$[100]$	$[\bar{2}3\bar{3}]$	$[011]$	$[31\bar{1}]$	35.3	60.5
	S4	$[01\bar{1}]$	$[011]$	$[100]$	$[21\bar{1}]$	$[011]$	$[1\bar{1}1]$	35.3	90.0
(100) X	Fe1	$[11\bar{1}]$	$[011]$	$[2\bar{1}1]$	$[01\bar{1}]$	$[011]$	$[100]$	0.00[a]	35.3
	Fe3	$[\bar{2}3\bar{3}]$	$[011]$	$[31\bar{1}]$	$[01\bar{1}]$	$[011]$	$[100]$	60.5	35.3
	Fe4	$[21\bar{1}]$	$[011]$	$[1\bar{1}1]$	$[01\bar{1}]$	$[011]$	$[100]$	90.0[b]	35.3
(110) Fe	X1	$[001]$	$[1\bar{1}0]$	$[110]$	$[111]$	$[1\bar{1}0]$	$[11\bar{2}]$	54.7	0.00
	X2	$[001]$	$[1\bar{1}0]$	$[110]$	$[113]$	$[1\bar{1}0]$	$[33\bar{2}]$	54.7	29.5
	X3	$[001]$	$[1\bar{1}0]$	$[110]$	$[001]$	$[1\bar{1}0]$	$[110]$	54.7	54.7
	X4	$[001]$	$[1\bar{1}0]$	$[110]$	$[\bar{1}\bar{1}2]$	$[1\bar{1}0]$	$[111]$	54.7	90.0

[a] The dislocation is placed in the $[1\bar{1}1]$ direction, giving an angle between slip plane and crack plane of 70.6°.

[b] The dislocation is placed in the $[\bar{1}\bar{1}1]$ direction, giving an angle between slip plane and crack plane of 19.4°.

orientations given in Table 6.1. The simulations are performed with and without dislocations present in the iron grain. Dislocation are placed in the iron grain by removing a half plane of atoms. Upon energy minimisation a dislocation forms. There are simulations performed with one dislocation initially present at the interface. In this case the dislocation is placed 10 Å underneath the interface so that upon minimisation the dislocation moves to the interface where it halts. There are also simulations performed with one, two or three dislocations initially present in the iron grain, far below the interface. In these cases the first dislocation is placed 100 Å underneath the interface, the second dislocation is placed 300 Å underneath the interface and the third dislocation is placed 500 Å underneath the interface.

In the simulations, atoms in the lower 10 Å are kept fixed, region F in Figure 6.1. On atoms in the upper 10 Å, region D, a displacement is imposed with a constant strain rate $\dot{\varepsilon}$ of 10^8 s^{-1}. For the mobile atoms, region M, time integration using a time step of 5 fs is performed at 1 K with a Nosé-Hoover thermostat. Prior to loading, the system is equilibrated at 1 K for 100 ps. The stress σ that results from the applied strain is calculated by summing the resulting forces on the atoms in region D and dividing this by the area in the x, y-plane.

The very low temperature of 1 K was chosen to be able to see details of the atomic behaviour driving the interface dynamics. At higher temperatures these details would be hidden by thermal vibrations.

The particular interface realisations for each of the 11 crystal orientations are taken

from [8], where they were created using the method described by Tschopp and McDowell [15]. A systematic collection of interface structures was generated by energy minimisation following extremely small initial displacements in the x and y directions. Of all the possible interface structures thus generated, the structure of which the interface energy has the highest number of occurrences in the collection is chosen as the final realisation.

6.2.3. LOCAL BEHAVIOUR

Similar to [8], [9] and [10], to calculate the local response to the applied load in the interface region, the region is divided into multiple bins along the x-direction. Each bin is then divided in two: one half above the interface, one half underneath, as shown in Figure 6.2. The width of each bin, δx, was chosen to be 8.8 Å, or five atomic [100] planes. The height of the bins, δz, was chosen as 20 Å. This ensures that the total interface region, which is the region in which significant extra strain is seen with respect to the bulk, is taken into account in the calculations made over each bin [8].
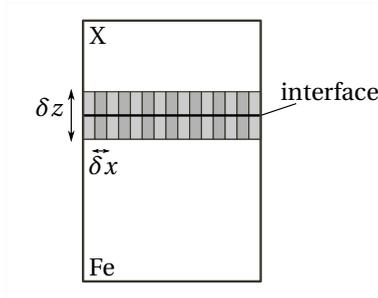
Figure 6.2: Division of interface region into bins with width δx of 8.8 Å and height δz of 20 Å. The bins have a role only in the data analysis, not in the simulation.

For every bin k the stress is calculated as the average of the stresses on the N_k atoms j in the bin, according to

$$\sigma_{\alpha\beta k} = \frac{1}{N_k} \sum_{j=1}^{N_k} \sigma_{\alpha\beta kj}. \tag{6.5}$$

The normal traction T_n in a bin is equal to the $\alpha\beta = zz$ component of this average stress in the bin, and the tangential traction T_t is equal to the $\alpha\beta = xz$ component.

The normal and tangential separations u_n and u_t between the bins above and underneath the interface are calculated at the time of interest as the increase in normal and tangential distance between the centers of mass (c) of these bins

$$
\begin{aligned}
u_n(t) &= z_c^X(t) - z_c^{Fe}(t) - \left(z_c^X(0) - z_c^{Fe}(0)\right), \\
u_t(t) &= x_c^X(t) - x_c^{Fe}(t) - \left(x_c^X(0) - x_c^{Fe}(0)\right),
\end{aligned}
\tag{6.6}
$$

where z_c^{Fe} is the z-position and x_c^{Fe} the x-position of the center of mass of the Fe-bin, below the interface, and z_c^X is the z-position and x_c^X is the x-position of the X-bin, above the interface. The time of interest is denoted as t. For simplicity of notation, T_n, u_n, T_t and u_t do not carry a subscript designating the bin to which they apply. The values for

T_n, T_t, u_n and u_t were calculated every 100 time steps (500 fs) as an average over 10 time steps (50 fs).

To determine T_t and u_t, the division of atoms into bins is made once, at the beginning of the simulation. If, under the influence of a shear load, interface sliding occurs, the upper and lower half of the bin move apart. The increase in tangential distance between the bin halves gives u_t. However, T_n and u_n have to be determined between the upper and lower half of a bin for which the bin halves are still at roughly the same x-position. Therefore, to determine T_n and u_n the division of atoms into bins is made every time step when these values are calculated.

For every bin the normal traction-separation curve is determined. It is assumed that interface decohesion occurs for a bin right after the maximum of the traction-separation curve is reached. Therefore, for every bin the maximum normal traction T_n^{max} and the time at which this traction is reached, $t_{decohesion}$, is determined. If for a particular bin $t_{decohesion}$ is lower than for the neighbouring bins, a crack nucleates at this bin. Otherwise, a crack grows at this bin. To compare T_n^{max} at crack growth and at crack nucleation, T_n^{max} at crack growth is determined by taking the average value of T_n^{max} for all bins along the interface, except those in a region of 15 bins around the crack nucleation position, to ensure that possibly different behaviour at crack nucleation is not included in the determination of the crack growth behaviour.

6.2.4. SYSTEMS

Three different kinds of systems are studied and under different loading conditions: 1. Interface systems without a dislocation present loaded in tension and loaded in tension after a previously applied shear load. 2. Interface systems with an initial dislocation present at the interface loaded in tension, loaded in tension after a previously applied shear load, and loaded in mixed-mode (combined tensile and shear loading). 3. Interface systems with dislocations impinging from the iron grain on the interface, loaded in tension.

6.2.5. METHODS

The MD-simulations are performed with LAMMPS [16, 17] and the GPU-accelerated version hereof [18–20]. The structures are visualised with OVITO [21]. As a measure for changes in the interface structure the number of non-bcc atoms at the interface is determined with the common neighbour analysis as implemented in LAMMPS [22, 23]. We found this to be a sensitive diagnostic for recording structural changes at an interface.

6.3. RESULTS

The crack nucleation behaviour is studied for the different interfaces under different conditions. In earlier work the relation between normal traction and normal separation during *crack growth* was determined for these interfaces under these conditions. To quantify the *crack nucleation* behaviour, the maximum of the normal traction at nucleation is determined, for easy comparison with this value during crack growth. Since the tangential traction and separation are determined for bins where the two bin halves can move apart if the precipitate grain slides with respect to the iron grain, it is impossi-

ble to extract the nucleation behaviour from the T_t versus u_t data. By looking at the T_t profile along the interface, however, which can be determined for instantaneously determined bins, the difference between T_t during crack growth and at nucleation can be identified. In Section 6.3.1 the crack nucleation behaviour of interfaces loaded in tension without a dislocation present is discussed. The influence of an initial dislocation is discussed in Section 6.3.2. In Section 6.3.3 we discuss the change in crack nucleation behaviour when dislocations impinge on the interfaces under tensile loading rather than being already present at the start. The effect of mixed loading conditions on the crack nucleation behaviour is discussed in Section 6.3.4, first under pre-shear loading (tensile loading preceded by shear loading), Section 6.3.4, then under mixed-mode loading, Section 6.3.4.

6.3.1. SYSTEMS WITHOUT DISLOCATION

Without a dislocation there is no obvious trigger for crack nucleation at flat interfaces. In the absence of a defect or impurity at the interface there is no significant stress concentration which triggers interface decohesion when a tensile load is applied. Crack nucleation will therefore occur at random positions along the interface, depending on where the critical stress for nucleation happens to be reached first. This is determined by the local interface structure, the thermal vibrations of the atoms, and the applied load. We find that for all the 11 studied interfaces cracks nucleate at multiple positions along the interface in the absence of dislocations. These cracks grow and merge until total decohesion along the interface is reached. In Figure 6.3 the maximum normal traction T_n^{max} upon crack nucleation (blue) is compared with the maximum normal traction during crack growth (red) for the 11 studied interfaces. For all the interfaces, except S1 and S4, T_n^{max} at crack nucleation is equal to, or only slightly lower than, T_n^{max} at crack growth.

In Figure 6.4 T_n^{max} and $t_{decohesion}$ are shown for every bin along the X4 and S4 interfaces, where $t_{decohesion}$ is defined as the time at which T_n^{max} is reached. For the S1 interface a similar behaviour as for the S4 interface is found, while all other interfaces behave similar to X4. A (local) minimum in $t_{decohesion}$ indicates crack nucleation at that bin position. We see that cracks nucleate at random positions along the X4 interface, Figure 6.4a, and that T_n^{max} at crack nucleation is equal to T_n^{max} during crack growth. Along the S4 interface, however, we find a regular pattern in the crack nucleation positions. Cracks nucleate at three distinct positions, Figure 6.4b, and T_n^{max} at crack nucleation is considerably lower than during crack growth, indicating that at these positions the cohesion at the interface is less than at the other positions.

Along the S4 interface cracks nucleate at three distinct positions. Along the S1 interface this number is four (not shown). Upon creation of these interfaces, the system sizes were chosen in such a way that, given the differences in lattice constant and orientation of the Fe and X grains, unit cells of both crystals would fit in the system volume an integer number of times with minimal strain. After creation of the interface structure the S1 interface was replicated four times along the x-direction and the S4 interface three times, to obtain the desired system size for this work and previous studies [8–10]. Although all interfaces were created in a similar manner, and for all interfaces the systems were replicated a certain number of times along the x-direction, only for the S1 and S4 interfaces cracks nucleate at a number of distinct positions corresponding with the number
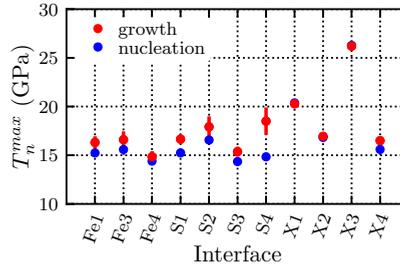
Figure 6.3: Maximum normal traction T_n^{max} at nucleation, blue, and during crack growth, red, for the 11 studied interfaces under tensile loading without a dislocation in the system. T_n^{max} at nucleation is T_n^{max} in the bin which reaches its maximum first. T_n^{max} at growth is the average maximum normal traction of all bins along the interface, except the bins in a region of 15 bins on both sides of the crack nucleation point. The error bars indicates the standard deviation of T_n^{max} over the interface. All red dots have an error bar, although for some it is not visible since the standard deviation of the interface is very small. The figure shows that T_n^{max} at crack nucleation is similar to T_n^{max} for crack growth for all interfaces except S1 and S4, which is explained in the main text.

(a) X4

(b) S4
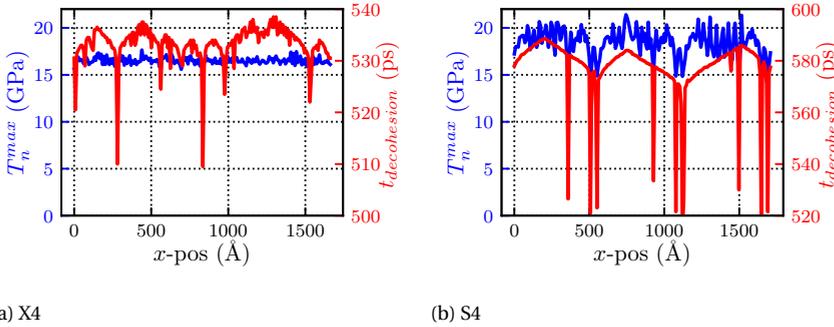
Figure 6.4: Maximum normal traction per bin, T_n^{max}, along the interface and the time, $t_{decohesion}$, at which T_n^{max} is reached, for the (a) X4 and (b) S4 interfaces under tensile loading without a dislocation in the system. The local minima in $t_{decohesion}$ indicate local crack nucleation. The figures show that for the X4 interface T_n^{max} at crack nucleation is equal to that during crack growth, while for the S4 interface it is considerably lower.

of replications, with a lower T_n^{max} at crack nucleation than during crack growth. This is therefore an artefact of the simulation. We can therefore conclude that, in the absence of dislocations, the relation between T_n and u_n for crack nucleation is equal to that for crack growth. This is a major result of this work and is further illustrated for the S1 interface in Figure 6.6, where in the top-left figure the relation between T_n and u_n for bin 42, where the crack nucleates, is indistinguishable from that for the neighbouring bins, where the crack grows.

6.3.2. Systems with an initial dislocation at the interface under tensile loading

With an initial dislocation present at the interface, there is also a stress concentration present at the interface, which is a clear candidate to trigger crack nucleation under an applied tensile load. This is also what we find, but there are exceptions. For all interfaces, except Fe4 and S4, a crack indeed nucleates at or right next to the dislocation position and grows in both directions along the interface under the tensile load. This is illustrated in Figure 6.5a for the X4 interface. Here it can be clearly seen that T_n^{max} is lower at the point where the crack nucleates (which is where the minimum in $t_{decohesion}$ is found) than at the remaining part of the interface. The crack nucleation behaviour in this case is not equal to the crack growth behaviour.

Although we find in general that the stress concentration from a dislocation triggers crack nucleation and that this nucleation behaviour is different from the growth behaviour, there are two exceptions. The initial dislocation at the Fe4 interface spreads in the interface upon energy minimisation of the structure, so that, in contrast to the other interfaces, there is no clear dislocation position but an entire region where the interface structure is changed by the spread of the dislocation. For the Fe4 interface the crack nucleates at the outer boundaries of this region depending on the initial velocity distribution, as is shown in Figures 6.5c and 6.5d. For all the other interfaces the dislocation only spreads in the interface under an applied shear load, as was explained in [9]. For the Fe4 interface the angle between the dislocation slip plane and the interface plane is only 19.4°, which is much smaller than for the other interfaces (see Table 6.1). Clearly this shallow angle allows for the dislocation to spread in the interface, resulting in a nucleation region rather than a nucleation point.

For the S4 interface a crack nucleates not only next to the dislocation position but also at one or more other positions along the interface, as illustrated in Figure 6.5b. Comparing Figures 6.5b and 6.4b shows that nucleation occurs at the same positions with and without a dislocation, which, as explained in Section 6.3.1, is triggered by an artefact of the simulation.

In Figure 6.8 the influence of the dislocation on the crack nucleation and growth behaviour under tensile loading for all interfaces can be seen by comparing ■ with ●. The initial dislocation at the X3 interface does not stay at the interface, but moves away from the interface into the Fe grain. Impinging dislocations at this X3 interface, as discussed in Section 6.3.3, are also reflected at the interface. This leads to a complication in the simulation. The reflected dislocations are blocked by the fixed atomic planes at the lower boundary of the simulation box, where they cause a stress concentration. This stress concentration triggers either crack nucleation at the lower boundary or disloca-

(a) X4

(b) S4

(c) Fe4

(d) Fe4
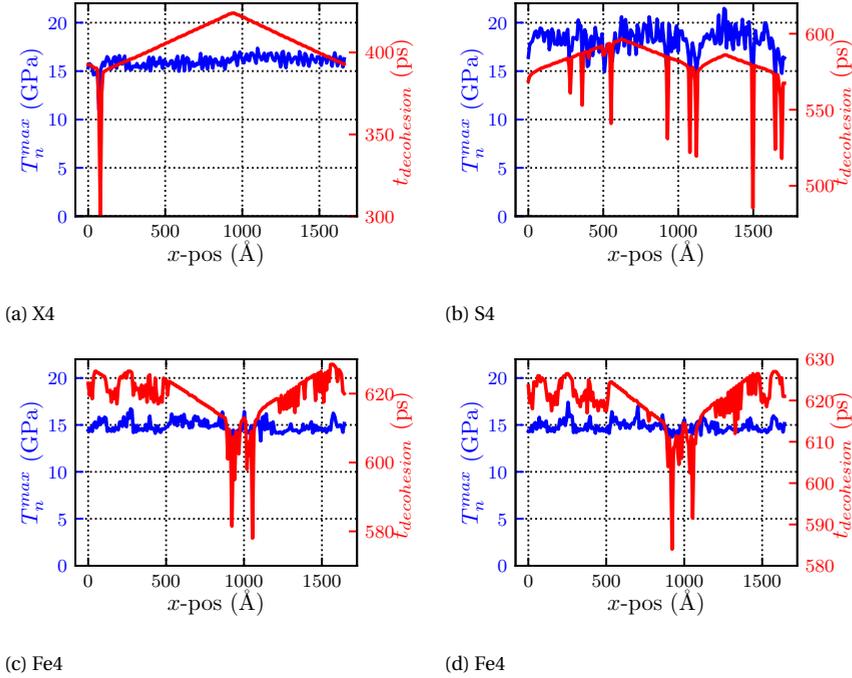
Figure 6.5: Maximum normal traction per bin, T_n^{max}, along the interface and the time, $t_{decohesion}$, at which T_n^{max} is reached, for the (a) X4, (b) S4, and (c and d) two realisations with different initial velocity distributions of the Fe4 interfaces under tensile loading with an initial dislocation present at the interface. The local minima in $t_{decohesion}$ indicate local crack nucleation. The figure shows that for the X4 interface a crack nucleates at one distinct position, for the Fe4 interface a crack nucleates in a region, while for the S4 interface cracks nucleate at multiple positions.

tion nucleation. Even when eventually a crack nucleates at the interface, it is therefore not triggered by the initial dislocation at the interface or the one, two, or three impinging dislocations as it is for the other interfaces. Therefore, no results for the X3 interface with dislocations are shown in the remainder of this work.

6.3.3. SYSTEMS WITH DISLOCATIONS IMPINGING ON THE INTERFACE UNDER TENSILE LOADING

Without a dislocation in the system, Figure 6.6 top left, the traction-separation relation for nucleation (bin 42) can not be distinguished from the traction-separation relation for growth (neighbouring bins) for the S1 interface under tensile loading. However, when dislocations impinge on the interface they cause a stress concentration, which in turn triggers crack nucleation. But the stress concentration is not the only issue. At the same time, impinging dislocations locally modify the structure of the interface. When this happens, u_n increases and T_n decreases at the dislocation impingement position (bin 129), resulting in a saw-tooth shape of the traction-separation relation at that position, Figure 6.6, where every drop in the traction indicates an impinging dislocation. In this work the nucleation position is defined as the position where the maximum in the traction-separation relation is reached first, as explained in Section 6.2.3. As can be seen from Figure 6.6 the nucleation position is not always precisely the dislocation impingement position, but it can also be a bin close to this position. The traction-separation relations for the bins in between the dislocation impingement position and the nucleation position are, just as for the dislocation impingement position and the nucleation position, different than for crack growth. The stress field of the dislocation(s) even leads to negative tractions close to the dislocation impingement position. The dislocation thus influences the traction-separation behaviour over a certain length along the interface.

We have just seen that the presence of a dislocation, both by its influence on the structure as by its stress field, changes the traction-separation relation. As was shown in [8], this change is only found in a small region surrounding the dislocation impingement position. Outside a region of 10 Burgers vectors to both sides of this position the traction-separation relations are not influenced by the dislocation(s). Therefore, the crack growth behaviour is independent of the number of impinging dislocations. The crack *nucleation* behaviour, however, as becomes clear from Figure 6.6, is influenced by the number of impinging dislocations as well as by the behaviour at the dislocation impingement position.

In Figure 6.7 the maximum normal tractions at crack growth, at crack nucleation and at the dislocation impingement position are compared for different numbers of impinging dislocations for all interfaces. As can be seen in this figure, dislocations can significantly reduce T_n^{max} at the dislocation impingement position and at the nucleation point. To ensure that the different behaviour caused by the dislocation is not included in T_n^{max} during crack growth, this quantity has been determined as an average over the interface away from the nucleation point, i.e. excluding a region of 15 bins at both sides of the nucleation point.
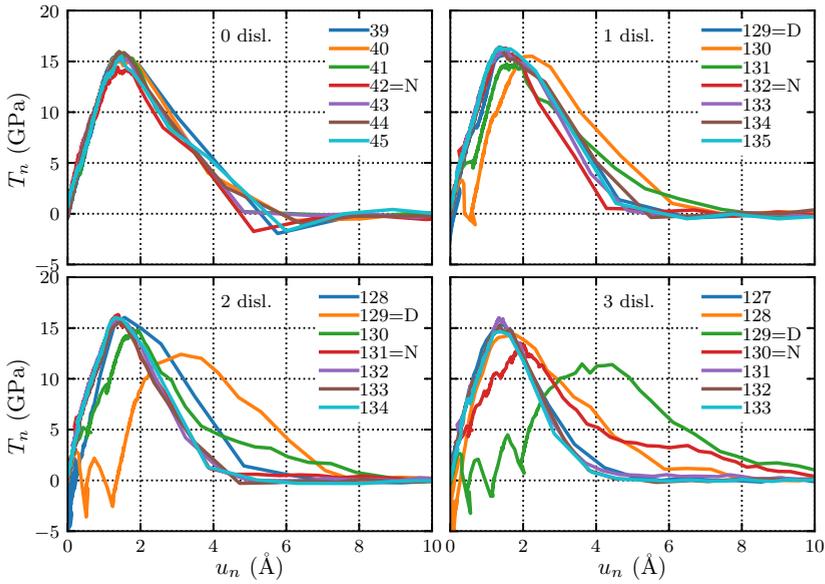
Figure 6.6: Normal traction T_n versus normal separation u_n for seven bins surrounding the crack nucleation point for simulations with different numbers of dislocations impinging on the S1 interface. The different coloured lines indicate the different bins along the interface. N is the bin where the crack nucleates, D is the bin where the dislocations impinge. One notices the initial saw-tooth patterns in the bins D caused by the impinging dislocations. The figure shows that without impinging dislocations and for bins further away from the dislocation impingement or nucleation bin, the traction-separation relations are equal and not influenced by the dislocations.
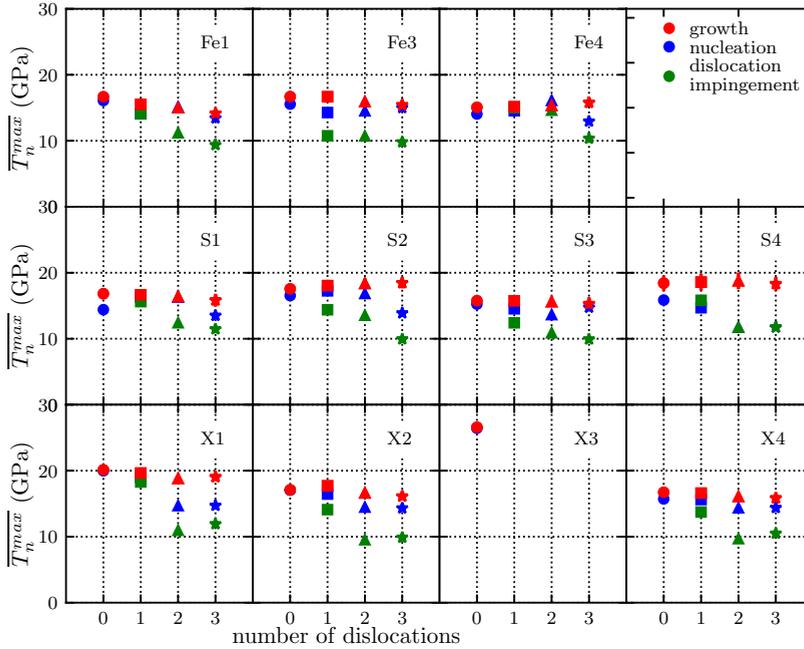
Figure 6.7: Maximum normal traction T_n^{max} at nucleation, blue, at dislocation impingement position, green, and during crack growth, red, for the 11 studied interfaces under tensile loading. Results are shown for different numbers of dislocations impinging on the interface. T_n^{max} at nucleation is T_n^{max} in the bin which reaches its maximum first. T_n^{max} at growth is the average maximum normal traction of all bins along the interface, except the bins in a region of 15 bins on both sides of the crack nucleation point. T_n^{max} at dislocation impingement is T_n^{max} in the bin where the dislocations impinge. The error bars indicate the standard deviation of T_n^{max} over the interface. All red points have an error bar, although for some it is not visible since the standard deviation of the interface is very small. The figure shows that impinging dislocations can significantly reduce T_n^{max} at the crack nucleation position and at the dislocation impingement position.

6.3.4. SYSTEMS WITH AN INITIAL DISLOCATION AT THE INTERFACE UNDER MIXED LOAD

Under mixed-mode or shear loading the dislocation can spread in the interface, depending on the interface, the loading direction, and the dislocation, as was shown for shear loads in [9]. When the dislocation spreads across the interface, the structure of the interface changes over a larger region than under pure tensile loading, and the local structure change at the dislocation impingement position will be different from that under pure tensile loading. Therefore the nucleation behaviour will be different than when the dislocation is intact. At the same time, due to the applied shear load, the structure of the entire interface might change, not only resulting in a different crack growth behaviour but also in a different crack nucleation behaviour. We will next discuss several cases of mixed mechanical loading.

CRACK NUCLEATION UNDER PRE-SHEAR LOADING

The influence of a previously applied shear load on the crack nucleation and crack growth behaviour under tensile loading for the interfaces with and without an initial dislocation is shown in Figure 6.8. In this figure the crack nucleation and crack growth behaviour are compared for the 11 interfaces in four different cases: 1. under tensile loading without a dislocation present, 2. under tensile loading with a dislocation present, 3. under tensile loading after a previously applied shear load without a dislocation present, and 4. under tensile loading after a previously applied shear load with a dislocation present. In the cases where a pre-shear load is applied, the shear load is applied for a sufficiently long time for the system to show steady-state sliding, i.e. to let one grain slide with respect to the other grain at constant tangential traction without any further changes in the interface structure. For the systems without a dislocation the system was sheared for 2500 ps, resulting in a strain of 0.25, and the systems with a dislocation were sheared for 1000 ps, resulting in a strain of 0.1. For most of the interfaces the presence of a dislocation influences the nucleation behaviour, both with (compare ▲ with ★ in Figure 6.8) and without (compare ● with ■) a previously applied shear load. In most cases the presence of a dislocation reduces T_n^{max} at crack nucleation. When a previously applied shear load changes the interface behaviour, the influence of the dislocation on the crack nucleation becomes, for most interfaces, larger than without the shear load being applied (compare difference between ★ and ★ with difference between ■ and ■). This difference is caused by the local change in interface structure when the dislocation has spread in the interface due to the applied shear load. This is illustrated for the X4 interface in Figure 6.9.

When a shear load is applied to the X4 interface without a dislocation present both the crack nucleation and crack growth behaviour under tensile loading are only slightly different than without a previously applied shear load, as can be seen by comparing Figure 6.9a with Figure 6.4a. When a dislocation is present at the interface, however, the shear load leads to a spread of the dislocation in the interface. This can be clearly seen by comparing the distribution of the tangential traction along the interface after a shear load is applied prior to normal loading, with and without an initial dislocation present at the interface, as shown in Figure 6.10. Without a dislocation T_t is uniform along the interface, while with a dislocation T_t is higher at the lowest and highest x-positions (due to the periodic boundary conditions) where the dislocation is spread in the interface. As
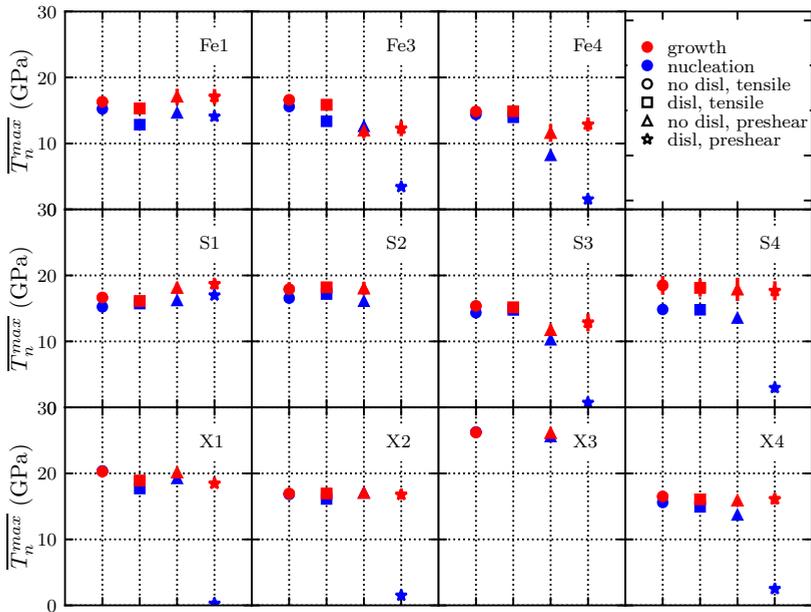
Figure 6.8: Maximum normal traction T_n^{max} at crack nucleation, blue, and during crack growth, red, for the 11 studied interfaces, under tensile loading without a dislocation present (•) and with a dislocation present (■). Results are also shown under tensile loading after a previously applied shear load without a dislocation present (▲, sheared for 2500 ps with $\dot{\varepsilon} = 10^8$ s^{-1}) and with a dislocation present (★, sheared for 1000 ps with $\dot{\varepsilon} = 10^8$ s^{-1}). T_n^{max} at nucleation is T_n^{max} in the bin which reaches its maximum first. T_n^{max} at growth is the average maximum normal traction of all bins along the interface, except the bins in a region of 15 bins at both sides of the crack nucleation point. T_n^{max} at dislocation impingement is T_n^{max} in the bin where the dislocations impinge. The error bars indicate the standard deviation of T_n^{max} over the interface. All red points have an error bar, although for some it is not visible since the standard deviation of the interface is very small. The figure shows that a previously applied shear load can change both the crack nucleation and crack growth behaviour, and that a dislocation increases this influence.

a result of this spread, a different crack nucleation and crack growth behaviour occurs in the affected part of the interface, Figure 6.9b, which is now less concentrated than without a pre-shear load, as can be seen by comparing Figure 6.9b with Figure 6.5a (where the influence of the dislocation on the crack nucleation and growth behaviour is shown without a shear load being applied). Without the shear load a dislocation gives a local reduction in T_n^{max} at crack nucleation. When a shear load is applied, however, T_n^{max} is increased not only at the crack nucleation point, but also in a region surrounding the dislocation position, similar to the region where T_t is increased.

(a) No dislocation
(b) Initial dislocation present at interface
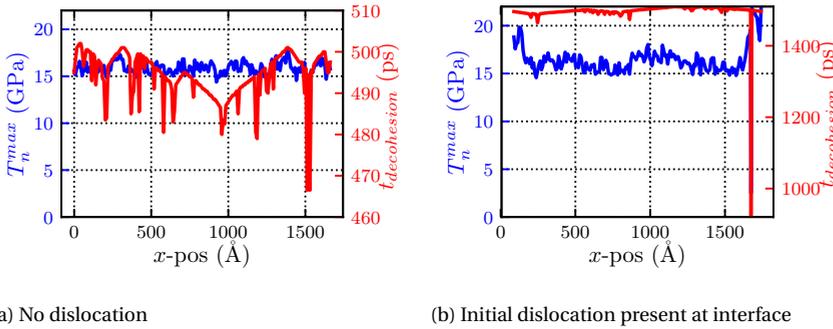
Figure 6.9: Maximum normal traction per bin, T_n^{max}, along the interface and the time, $t_{decohesion}$, at which T_n^{max} is reached, for pre-sheared X4 interface under tensile loading (a) without and (b) with an initial dislocation present at the interface. The local minima in $t_{decohesion}$ indicate local crack nucleation. The figure shows that without a dislocation the influence of the pre-shear load on crack nucleation and growth is only small (compare Figures 6.4a and 6.9a), while with an initial dislocation present the pre-shear load leads to a local change of interface structure around the dislocation position and therefore to a locally changed interface behaviour.

(a) No dislocation
(b) Initial dislocation present at interface
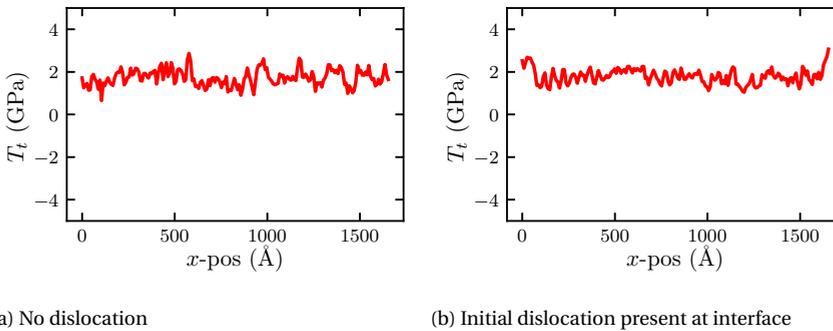
Figure 6.10: Tangential traction per bin, T_t, along the interface for pre-sheared X4 interface before tensile loading (a) without and (b) with an initial dislocation present at the interface. The figure shows that with an initial dislocation present the pre-shear load leads to a local change of interface structure around the dislocation position and therefore to a locally changed interface behaviour.

Applying a mixed-mode load to the system with a dislocation influences the interface behaviour in multiple ways compared to pure tensile loading or to pure shear loading. The shear component of the load can change the structure of the entire interface, leading to a different $T_n(u_n)$ relation for both crack growth and crack nucleation. Due to the shear component of the load the dislocation can spread in the interface, leading to a different $T_n(u_n)$ relation for crack nucleation. Analogously, since simultaneously with the shear load component a tensile load component is applied, the effect of the shear load component is also constantly influenced by the tensile load component. The structure change of the interface is different for shear in combination with a tensile load than for pure shear, leading in turn to a different $T_n(u_n)$ relation. In Figure 6.11 T_n^{max} during both crack growth and crack nucleation is shown for the studied interfaces for mixed-mode loads with different mode-mixity angles. As can be seen, the influence of the dislocation in combination with the mixed-mode load is different for the different interfaces. For the S4 interface for example T_n^{max} for crack growth decreases with increasing mode-mixity angle due to the interface structure change, as was explained in [10]. T_n^{max} during crack nucleation also decreases with increasing mode-mixity angle. For the X4 interface however the change in T_n^{max} during both crack growth and crack nucleation for different mode-mixity angles is quite small. Only for a mode-mixity angle of 30° or 85° the crack nucleation behaviour is significantly influenced. The reasons for this have not been studied in detail.

6.4. COHESIVE LAW

Figures 6.3, 6.7, 6.8, and 6.11 together summarise the influence of dislocations and different loading modes on the normal crack nucleation and crack growth behaviour of the different interfaces. Although not explicitly described in Section **??**, the tangential behaviour is similarly influenced regarding the (non-)locality of crack nucleation, as is illustrated in Figure 6.10. We will now describe the implications of these results for the cohesive laws for the $T_n(u_n, u_t)$ and $T_t(u_n, u_t)$ relations. In [8], [9] and [10] these were derived only for crack growth behaviour. Crack nucleation behaviour was not taken into account. From the present study three different cases of crack nucleation behaviour can be distinguished. In the following we describe these three cases and how this behaviour should be included in the cohesive zone model.

In the first case, as is shown in Section 6.3.1, without a dislocation the crack nucleation behaviour is equal to the crack growth behaviour. The cohesive laws derived for crack growth can therefore also be used to describe crack nucleation in this case.

In the second case, the presence of a dislocation can influence the crack nucleation behaviour as is illustrated in Figure 6.6. In this case the cohesive laws derived for crack growth *are not suitable* to describe crack nucleation. This is because the dislocation causes a structure change at the interface which can either be very local or more spread along the interface. Especially when the structure change is very local, the crack nucleation can be very different from the crack growth behaviour. Larger-scale material modelling methods, such as Discrete Dislocation Plasticity, that use the cohesive laws to describe the interface behaviour typically have a resolution which is coarser than the length scale at which crack nucleation plays a role. Therefore, in these kinds of simula-
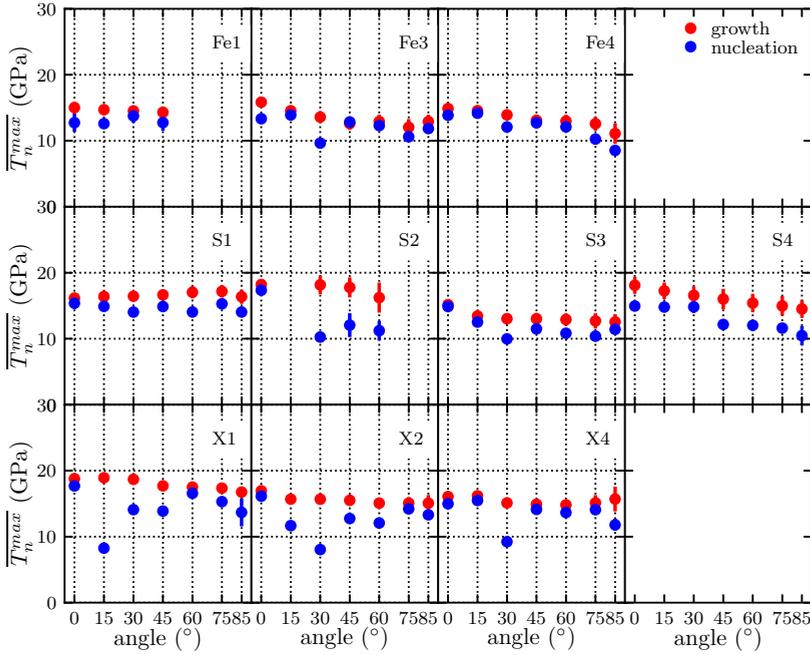
Figure 6.11: Maximum normal traction T_n^{max} at crack nucleation, blue, and during crack growth, red, for the studied interface with an initial dislocation present at the interface under mixed-mode loading with different mode-mixity angles. The error bars indicate the standard deviation of T_n^{max} over the interface for crack growth and over multiple simulations (both for crack growth and crack nucleation). The figure shows that a combination of a shear and a tensile load has a different effect on T_n^{max} at both crack nucleation and crack growth for the different interfaces.

tions, the difference between crack nucleation and crack growth will be neglected. The stress field of a dislocation will then trigger crack nucleation according to the cohesive laws for crack growth and no different cohesive relation for crack nucleation is needed.

In the third case, the structure change at the interface caused by the dislocation is not only local but spreads along the interface. The influence of this structure change on the traction-separation relations has already been taken into account in the cohesive laws derived in [10] for crack growth under mixed-mode or pre-shear conditions. Therefore, in simulations at larger length scale, the difference between crack nucleation and crack growth can again be neglected, since nucleation plays a role only at a length scale smaller than the resolution of the simulation, while the influence of dislocations is already taken into account in the cohesive laws for crack growth.

This work shows that crack nucleation takes place on a length scale smaller than the resolution of larger scale material models such as discrete dislocation plasticity. In these material models crack nucleation will therefore typically be described according to the cohesive laws for crack growth, which are not modified by crack nucleation. The dislocations that trigger crack nucleation however, can also change the interface structure and with that modify the cohesive laws for crack growth, depending on the interface, the mechanical loading mode, and the number of dislocations. The influence of dislocations on crack growth behaviour should therefore be included in the larger scale material models, as it is in our cohesive laws for crack growth [8–10].

6.5. CONCLUSIONS

In this work we find that in the absence of defects or impurities at an interface, crack nucleation occurs according to the same traction-separation relation as crack growth at the interface. To start a crack is not harder or easier than to let it grow. The presence of dislocations at the interface, however, changes the traction-separation relations at the dislocation position, and, since the stress fields of the dislocations trigger crack nucleation, also the traction-separation relations for nucleation. Depending on the interface and the loading direction, the influence of the dislocations can be either very local, or felt in a larger part of the interface, when the dislocations are spread in the interface.

Earlier derived cohesive zone models do not take into account the difference between crack nucleation and crack growth. These cohesive zone models are typically incorporated in material models at larger length scale than MD. The typical resolution of these models is larger than the region where the influence of the dislocations on the traction-separation relations is felt. This does therefore not lead to erroneous results. When the dislocations are spread in the interface, however, the influence of the dislocations on the traction-separation relations should be taken into account. In our earlier derived cohesive zone model [10] this is already taken into account and therefore no separate relations for crack nucleation are needed when this cohesive zone model is incorporated in a larger-scale material model.

REFERENCES

[1] A. Elzas and B. J. Thijsse, *Crack nucleation at iron/precipitate interfaces in the presence of dislocations under different loading conditions,* submitted to Engineering Fracture Mechanics (2018).

[2] G. I. Barenblatt, *The Mathematical Theory of Equilibrium Cracks in Brittle Fracture,* Advances in Applied Mechanics **7**, 55 (1962).

[3] D. Dugdale, *Yielding of steel sheets containing slits,* Journal of the Mechanics and Physics of Solids **8**, 100 (1960), arXiv:0021-8928(59)90157-1 [10.1016] .

[4] J. J. Möller and E. Bitzek, *Comparative study of embedded atom potentials for atomistic simulations of fracture in α-iron,* Modelling and Simulation in Materials Science and Engineering **22**, 045002 (2014).

[5] F. P. E. Dunne, *Fatigue crack nucleation: Mechanistic modelling across the length scales,* Current Opinion in Solid State and Materials Science **18**, 170 (2014).

[6] Z. Pan and T. J. Rupert, *Damage nucleation from repeated dislocation absorption at a grain boundary,* Computational Materials Science **93**, 206 (2014).

[7] A. Elzas and B. J. Thijsse, *Dislocation impacts on iron/precipitate interfaces under shear loading,* Modelling and Simulation in Materials Science and Engineering **24**, 85006 (2016).

[8] A. Elzas and B. J. Thijsse, *Cohesive law describing crack growth at iron/precipitate interfaces,* Computational Materials Science **134**, 214 (2017).

[9] A. Elzas, T. P. C. Klaver, and B. J. Thijsse, *Cohesive laws for shearing of iron / precipitate interfaces,* Computational Materials Science **152**, 417 (2018).

[10] A. Elzas and B. J. Thijsse, *Crack growth at iron / precipitate interfaces under mixed loading conditions,* accepted by Mechanics of Materials (2018).

[11] L. Malerba, M. C. Marinica, N. Anento, C. Björkas, H. Nguyen, C. Domain, F. Djurabekova, P. Olsson, K. Nordlund, A. Serra, D. A. Terentyev, F. Willaime, and C. S. Becquart, *Comparison of empirical interatomic potentials for iron applied to radiation damage studies,* Journal of Nuclear Materials **406**, 19 (2010).

[12] P. A. Gordon, T. Neeraj, M. J. Luton, and D. Farkas, *Crack-tip deformation mechanisms in α-Fe and binary Fe alloys: An atomistic study on single crystals,* Metallurgical and Materials Transactions A: Physical Metallurgy and Materials Science **38 A**, 2191 (2007).

[13] M. I. Mendelev, S. Han, D. J. Srolovitz, G. J. Ackland, D. Y. Sun, and M. Asta, *Development of new interatomic potentials appropriate for crystalline and liquid iron,* Philosophical Magazine **83**, 3977 (2003).

6

[14] G. J. Ackland, M. I. Mendelev, D. J. Srolovitz, S. Han, and A. V. Barashev, *Development of an interatomic potential for phosphorus impurities in α-iron,* Journal of Physics: Condensed Matter **16**, S2629 (2004).

[15] M. A. Tschopp and D. L. McDowell, *Structures and energies of $\Sigma3$ asymmetric tilt grain boundaries in copper and aluminium,* Philosophical Magazine **87**, 3147 (2007).

[16] *LAMMPS Molecular Dynamics Simulator,* http://lammps.sandia.gov.

[17] S. J. Plimpton, *Fast Parallel Algorithms for Short-Range Molecular Dynamics,* Journal of Computational Physics **117**, 1 (1995).

[18] W. M. Brown, P. Wang, S. J. Plimpton, and A. N. Tharrington, *Implementing Molecular Dynamics on Hybrid High Performance Computers - Short Range Forces,* Computer Physics Communications **182**, 898 (2011).

[19] W. M. Brown, A. Kohlmeyer, S. J. Plimpton, and A. N. Tharrington, *Implementing Molecular Dynamics on Hybrid High Performance Computers - Particle-Particle Particle-Mesh,* Computer Physics Communications **183**, 449 (2012).

[20] W. M. Brown and Y. Masako, *Implementing molecular dynamics on hybrid high performance computers – Three-body potentials,* Computer Physics Communications **184**, 2785 (2013).

[21] A. Stukowski, *Visualization and analysis of atomistic simulation data with OVITO–the Open Visualization Tool,* Modelling Simul. Mater. Sci. Eng. **18**, 015012 (2009).

[22] D. Faken and H. Jónsson, *Systematic analysis of local atomic structure combined with 3D computer graphics,* Computational Materials Science **2**, 279 (1994).

[23] H. Tsuzuki, P. S. Branicio, and J. P. Rino, *Structural characterization of deformed crystals by analysis of common atomic neighborhood,* Computer Physics Communications **177**, 518 (2007).

7

CONCLUSIONS

7.1. CRACKS IN METALS

Multiphase alloys such as advanced high strength steels have a heterogeneous structure, where different domains in the material have a different strength, giving these materials a high strength and a high ductility at the same time. However, these materials can show unexpected failure. When they are deformed, dislocations that move in the softer domains may pile-up at the interfaces between the soft and the hard domains causing stress concentrations, which in turn can trigger interface decohesion. This may lead to the formation of voids, which, when they coalesce, can form a macroscopic crack. To prevent such material failure in operating conditions, material models are needed that accurately predict the material behaviour. In this thesis the process of interface decohesion at interfaces between the soft iron matrix and a hard precipitate material is studied on the nano-scale with molecular dynamics simulations, to understand which conditions lead to interface decohesion and in order to improve existing material models at larger scale.

7.2. INTERFACE STRUCTURE

From the results in this thesis it is concluded that the interface structure is the key factor determining the interface behaviour. The orientation of the grains at both sides of the interface, as well as the interaction strength between the grains, determine the interface structure. The adhesive energy of the interface, the dislocation accommodation capability, and the relation between normal and tangential tractions and separations at the interface are all determined by this interface structure. However, the interface structure is not static, because it can change due to an applied load or due to dislocations interacting with the interface. Depending on the interface, the loading, and the presence of dislocations, a change in interface structure may occur very locally or affect a large part or even the entire interface. It is found that an interface for which the structure has changed, partly or entirely, shows a different behaviour than the original interface structure. For some interfaces this means that interface decohesion occurs at much lower

applied loads than for the original interface.

7.3. MULTISCALE MODELLING

To accurately predict the macro-scale material behaviour in a computational framework, a bottom-up approach should be used. With such an approach the material behaviour is modelled at different length scales, where crucial information from one length scale is carried on to the next larger length scale. From this thesis it is clear that the differences in behaviour between the different interfaces and the change in behaviour when the structure of an interface changes are crucial ingredients to carry on from the nano-scale to the micro-scale. In this thesis, therefore, cohesive laws are developed based on the nano-scale information, to describe the interface behaviour, in terms of traction-separation relations, in micro-scale material models. Not only are the different necessary input parameters determined for the cohesive laws for the different interfaces, also the change in behaviour due to a change in structure is taken into account.

7.4. CRACK NUCLEATION AND CRACK GROWTH

In this thesis a distinction is made between crack *nucleation* and crack *growth*. Crack *nucleation* is defined as the first occurrence of interface decohesion, whereas the progression of this decohesion along the interface is considered as crack *growth*. It is found that only under pure normal loading in the absence of dislocations crack nucleation and crack growth occur according to the same traction-separation relation. Both the presence of dislocations and the presence of a shear component in the load influence the interface structure and with that change the nucleation behaviour. This change can be very local, affecting only the nucleation behaviour, or more spread out, affecting both nucleation and growth behaviour but not necessarily in the same manner. The nucleation itself is a very local effect taking place on a length scale smaller than the resolution of the micro-scale material models. In these models the start of interface decohesion will therefore not be separately described. If the interface structure is affected in a larger region however, this should be included in the cohesive laws used in larger-scale material models, to correctly capture the interface behaviour. In the cohesive laws derived in this thesis the change in interface behaviour due to interface structure change upon nucleation is included.

ACKNOWLEDGEMENTS

The road towards a PhD degree can be sometimes lonely. But luckily, throughout the years, there have been many people who supported me, were open for critical discussions, or just made me laugh. First of all, I would like to thank my promotor, Barend Thijsse, for giving me the opportunity to work on this project for almost five years. Without you, I never would have even started on this road. In the past years for both of us many things have changed in our personal situation, but you always made time to discuss or read my work. Thank you for your continuous support, your critical thinking, and the many pleasant conversations.

Studying the atomic scale for so many years, a larger scale perspective was very much needed. Thank you, Erik van der Giessen and Tarun Katiyar, for many pleasant and helpful discussions. I would also like to thank the other participants in the Physics of Failure program and the members of M2i cluster 2 for helpful discussions.

All my past and present colleagues from the MSE department and in particular from the fourth floor I would like to thank for helpful discussions, practical assistance and completely meaningless, but very much appreciated, conversations near the coffee machine. Special thanks to the '5me-people' for many helpful discussions and the weekly opportunity to tear my mind off my own work and focus on something else. Thank you, Peter, for practical assistance with all the computer stuff you know so much more about than I ever will. Thanks for not giving up during the gpu-struggle. It incredibly increased the amount of work I was able to do these past years, which certainly is reflected in this thesis. Thank you, Syam, for sharing not only an office with me all these years, but also many pleasant conversations.

All my family and friends I would like to thank for their support during the past years. In particular I would like to thank Guido for supporting me when starting this project. We did not make it to the end together, but you never stopped believing in me. Papa and mama, you have supported me in starting this project and never stopped showing interest in my work, even though you had so many other things on your mind. Thank you for everything.

Thank you, Walter, for being there for me, listening to my stories and my complaints, helping me to free my mind from work and other struggles, and motivating me in your own famous words. It is so good to know that you would have done it yourself if it would have been easy.

Although this project has been a big part of my life the past five years, it certainly has not been the most important part. Lieke, Thomas and Martin, thank you for always making me remember that there are far more important things in life than working towards a PhD degree. I know it has not always been easy for you these past years and you certainly did not always got the attention you deserved. Thank you for bearing with me. The three of you might look like regular children, but you are the most special ones I know.

CURRICULUM VITÆ

Astrid ELZAS

29-09-1978	Born in The Hague, The Netherlands
1990–1996	Pre-university education Gymnasium Haganum, The Hague
1996–2003	BSc in Mechanical Engineering Eindhoven University of Technology
2/2012–7/2013	MSc in Mechanical Engineering Delft University of Technology *Thesis:* Anodization of aluminium, atomic simulations of the initial process steps
9/2013–3/2014	Researcher Delft University of Technology, Chemical Engineering, Product and Process Engineering
4/2014–1/2019	PhD. Materials Science Delft University of Technology *Thesis:* Nano-scale failure in steel *Promotor:* Prof. dr. B.J. Thijsse

LIST OF PUBLICATIONS

9. A. Elzas, B. J. Thijsse, *Shear dislocation loops in iron*, in preparation.

8. S. Karewar, A. Elzas, J. Sietsma, M. J. Santofimia, *An atomistic perspective of the nucleation and the origin of twin morphology of martensite in Fe*, in preparation.

7. R. J. Dikken, A. Elzas, B. J. Thijsse, *The effect of temperature and locality on sensitivities in molecular dynamics simulations*, in preparation.

6. A. Elzas, B. J. Thijsse, *Crack nucleation at iron/precipitate interfaces in the presence of dislocations under different loading conditions*, submitted.

5. A. Elzas, B. J. Thijsse, *Cohesive law describing the interface behaviour of iron/precipitate interfaces under mixed loading conditions*, accepted by Mechanics of Materials, in press.

4. A. Elzas, T. P. C. Klaver, B. J. Thijsse, *Cohesive laws for shearing of iron/precipitate interfaces*, Computational Materials Science **152**, 417 (2018).

3. A. Elzas, B. J. Thijsse, *Cohesive law describing crack growth at iron/precipitate interfaces*, Computational Materials Science **134**, 214 (2017).

2. A. Elzas, B. J. Thijsse, *Dislocation impacts on iron/precipitate interfaces under shear loading*, Modelling and Simulation in Materials Science and Engineering **24**, 085006 (2016).

1. A. Elzas, B. J. Thijsse, *Ionic motion during field-assisted oxidation of aluminium studied by molecular dynamics simulations*, Computational Materials Science **90**, 196 (2014).